Planar Heterojunction Perovskite Solar Cells via Vapour Deposition and Solution Processing



Mingzhen Liu

Wolfson College

University of Oxford

A thesis submitted for the degree of
Doctor of Philosophy

October, 2014

Planar Heterojunction Perovskite Solar Cells via Vapour Deposition and Solution Processing

Mingzhen Liu, Wolfson College, Oxford

Thesis submitted for the degree of Doctor of Philosophy at the University of Oxford, October, 2014

Abstract

Hybrid organic-inorganic solar photovoltaic (PV) cells capable of directly converting sunlight to electricity have attracted much attention in recent years. Despite evident technological advancements in the PV industry, the widespread commercialisation of solar cells is still being mired by their low conversion efficiencies and high cost per Watt. Perovskites are an emerging class of semiconductors providing a low-cost alternative to silicon-based photovoltaic cells, which currently dominate the market. This thesis develops a series of studies on "all-solid state perovskite solar cells" fabricated via vapour deposition which is an industrially-accessible technique, to achieve planar heterojunction architectures and efficient PV devices.

Chapter 2 presents a general outlook on the operating principles of solar cells, delving deeper into the specific operational mechanism of perovskite solar cells. It also explores the usual methods employed in the fabrication of perovskite thin films. Chapter 3 describes the experimental procedures followed during the fabrication of the individual components constituting the device from the synthesis of the precursors to the construction of the functioning perovskite PV devices. Chapter 4 demonstrates pioneering work involving the dual-source vapour deposition (DSVD) of planar heterojunction perovskite solar cells which generated remarkable power conversion efficiency values surpassing 15%. These significant results pave the way for the mass-production of perovskite PVs. To further expand the range of feasible vapour deposition techniques, a two-layer sequential vapour deposition (SVD) technique is explored in Chapter 5. This chapter focusses on identifying the factors affecting the fundamental properties of the vapour-deposited films. Findings provide an improved understanding of the effects of precursor compositions and annealing conditions on the films. Chapter 5 concludes with a comparison between SVD and DSVD fabricated films, highlighting the benefits of each vapour deposition technique.

Furthermore, hysteretic effects are analysed in Chapter 6 for the perovskite PV devices fabricated based on different structural configurations. An interesting discovery involving the temporary functioning of compact layer-free perovskite PV devices suggests the presence of a built-in-field responsible for the hysteresis of the cells. The observations made in this chapter yield a new understanding of the functionality of individual cell layers. Combining the advantages of the optimum vapour deposition technique established in Chapter 4 and Chapter 5, with the enhanced understanding of perovskite PV cell operational mechanism acquired from Chapter 6, an ongoing study on an "all-perovskite" tandem solar cell is introduced in Chapter 7. This demonstration of the "all-perovskite" tandem devices confirms the versatility of perovskites for a broader range of PV applications.

Publications

Published Work

(1) Liu, M., Johnston, M. B. & Snaith, H. J. Efficient planar heterojunction perovskite solar cells by vapour deposition. *Nature* **501,** 395–8 (2013)

(2) Zhang, Y.,* Liu, M.,* Eperon, G., Leijtens, T., McMeekin, D., Saliba, M., Zhang, W., Herz, L. M., Johnston, M. B., Lin, H., & Snaith, H. J. Charge selective contacts, mobile ions and anomalous hysteresis in organic-inorganic perovskite solar cells, *Mater. Horiz.*, DOI: 10.1039/C4MH00238E (2015).(just accepcted)

(3) Wehrenfennig, C., Liu, M., Snaith, H. J., Johnston, M. B. & Herz, L. M. Homogeneous Emission Line Broadening in the Organo Lead Halide Perovskite $CH_3NH_3PbI_{3-x}Cl_x$. *J. Phys. Chem. Lett.* **5,** 1300–1306 (2014).

(4) Wehrenfennig, C., Liu, M., Snaith, H. J., Johnston, M. B. & Herz, L. M. Charge-carrier dynamics in vapour-deposited films of the organolead halide perovskite $CH_3NH_3PbI_{3-x}Cl_x$. *Energy Environ. Sci.* **7,** 2269 (2014).

(5) Wehrenfennig, C., Liu, M., Snaith, H. J., Johnston, M. B. & Herz, L. M. Charge carrier recombination channels in the low-temperature phase of organic-inorganic lead halide perovskite thin films. *APL Mater.* **2,** 081513 (2014)

Manuscript in Preparation

(6) Liu, M., Menelaou, C., Pathak, S., Parkinson, P., Huang, J., Herz, L. M., Snaith, H. J. & Johnston, M. B. A Comparison between Two-Layer Sequential Vapour Deposition and Dual-Source Vapour Deposition Fabrication Methods.

** Denotes equal contribution authorships*

Acknowledgements

First and foremost, I am greatly indebted to my supervisors Professor Henry Snaith and Prof. Michael Johnston, for their guidance and constant support throughout my PhD study. I should thank Henry for many things, most of all for sharing his foresight and enthusiasm in science with me. His spirit inspired me to discover much excitement in research. I also owe a great deal to Michael who always supported me and helped me whenever I needed it most. His solid understanding of science sets an example of a great scientist for me.

I also would like to thank all my learned colleagues in Snaith's and Johnston's groups. It has been great to work with all of you. I would especially like to express my deepest gratitude to Dr. Sandeep Pathak, for being such a supportive and helpful lab buddy, always encouraging me to strive, to seek, to find and not to yield.

Furthermore, I highly appreciate the opportunity to collaborate with Professor Laura Herz and I am grateful to several members in her research group, in particular, Christian Wehrenfennig and Chris Menelaou for helping me with spectroscopy measurement.

I am much obliged to my dearest friend, Chindu Nwankwo. If there is anything I should appreciate of my life in Cambridge, it must be the friendship with you. Thanks for your time and efforts for proofreading my thesis even though you are extremely busy with your work. I also would like to thank all of my friends in Wolfson College, thanks for those who keep encouraging me when I was spending all days and nights in the college's library.

My boyfriend, Yunfeng Harry Rong, you are the best gift I have received. Thanks for accompanying me and helping me get through this most difficult challenge. I have almost forgotten how stressful the writing-up of this thesis was, thinking of the worthwhile times we spent and will be spending together.

Last but not the least, I would like to express my very deepest appreciation to my parents. I appreciate your unwavering support and unconditional love. Papa, your attitude towards life always motivates me and supports me to overcome every obstacle I come across. Mama, you are such an amazing woman, regardless of your career or our family. Going back home is always the one thing I have been looking forward to for the last 7 years. Thanks you both for always being such strong back-up for me all the way throughout my life.

Contents

Abstract i

Publications ii

Acknowledgements iii

Contents iv

List of Figures and Tables ix

Nomenclature xi

Chapter 1 Introduction 1

1.1 Background Motivation 1

1.2 Goals of the Thesis 4

References 8

Chapter 2 Background 10

2.1 Operating Principles of Photovoltaic Devices 10

2.2 Solar cell Characterisation 13

2.3 Perovskite and Perovskite Solar Cells 20

2.3.1 Perovskite Properties 20

2.3.2 Perovskite-Sensitized Solar Cells 27

2.3.3 Meso-Superstructured Solar Cells 29

2.3.4 Planar Heterojunction Perovskite Solar Cells 29

2.3.5 Tandem Solar Cells 30

2.4 Operation Mechanisms of Perovskite Solar Cells 32

2.5 Fabrication Techniques for Perovskite Films 35

2.5.1 Spin-Coating 35

2.5.2 Sequential Two-Step Deposition 36

2.5.3 Vapour Deposition 37
2.5.4 Other Deposition Methods 38
References 39
Chapter 3 Methodology 45
3.1 Synthesis of Precursors 45
3.1.1 Synthesis of Methylammonium Iodide 46
3.1.2 Synthesis of Methylammonium Bromide 46
3.1.3 Purchase of Metal Halide 46
3.1.4 Synthesis of Hybrid Halide Perovskite 46
3.2 Device Assembly 47
3.2.1 FTO Glass Preparation 47
3.2.2 Fabrication of Meso-superstructured Perovskite Device 48
3.2.3 Fabrication of Planar Heterojunction Perovskite Device 49
3.2.4 Hole-Transporter Deposition and Electrode Deposition 53
3.3 Characterisation Techniques 53
3.3.1 Crystallographic Analysis 54
3.3.2 Microstructural Analysis 54
3.3.3 Photo-physical Analysis 55
3.3.4 Solar Cell Performance Characterisation 58
References 59
Chapter 4 Efficient Planar Heterojunction Perovskite Solar Cells by Dual-Source Vapour Deposition 60
4.1 Introduction 62
4.2 Methods 64
4.2.1 Method Summary 64
4.2.2 Perovskite Films Fabricated by Dual-Source Vapour Deposition 64
4.2.3 Perovskite Film Fabricated by Solution Processing 67

4.2.4 Hole-Transporter Deposition and Electrode Deposition.....67
4.3 Results and Discussion..... 67
4.3.1 Dual-Source Vapour Deposition and Crystallographic Analysis 67
4.3.2 Microstructural Analysis.....69
4.3.3 Photo-physical Analysis.....72
4.3.4 Solar Cell Characterisation 75
4.4 Summary 77
References..... 78
Chapter 5 A Comparison between Two-Layer Sequential Vapour Deposition and Dual-Source Vapour Deposition Fabrication Methods**...81**
5.1 Introduction..... 83
5.2 Methods..... 85
5.2.1 Method Summary.....85
5.2.2 Perovskite Films Fabricated by Vapour Deposition 86
5.2.3 Hole-Transporter Deposition and Electrode Deposition.....88
5.3 Results and Discussion..... 89
5.3.1 Optimisation of Perovskite Films Fabricated by the Two-Layer Sequential Vapour Deposition.....89
5.3.2 Comparison of Two-Layer Sequential Vapour Deposition and Dual-Source Vapour Deposition 95
5.4 Summary 106
References..... 107
Chapter 6 Understanding on Hysteresis in Perovskite Solar Cells through Titania Compact-Free System **.....110**
6.1 Introduction..... 112
6.2 Methods..... 114
6.2.1 Substrate Preparation and Synthesis of Precursors.....114

6.2.2 Fabrication of Standard Meso-Superstructured and Planar Heterojunction Perovskite Devices 114
6.2.3 Compact-Free Device Fabrication 114
6.2.4 Hole-Transporter and Electrode Deposition 115
6.2.5 Fourier Transform Photocurrent Spectroscopy (FTPS) 115
6.3 Results and Discussion 116
6.3.1 Device Configuration 116
6.3.2 Device Performance and Hysteretic Behaviour 118
6.3.3 Discussion on the Origins of Hysteresis from a Stabilisation Power Perspective 122
6.3.4 Perovskite-only System 128
6.3.5 Hysteresis Loop from FTPS Measurement 130
6.4 Summary 132
References 133
Chapter 7 Ongoing Work: Room-Temperature Fabrication of Tandem Perovskite Solar Cells 137
Content and Summary 137
7.1 Introduction 139
7.2 Methods 141
7.2.1 Synthesis of Perovskite Precursors for Bottom Sub-Cell 141
7.2.2 Fabrication of Perovskite Films for Top Sub-Cell 142
7.2.3 Fabrication of Inverted Single-Junction Device 142
7.2.4 Fabrication of the Tandem Device 143
7.3 Results and Discussion 143
7.3.1 Fabrication of Bottom Cells through Solution Processing 145
7.3.2 Fabrication of Top Cells through Vapour Deposition 149
7.3.3 Model of an All-Perovskite Tandem Device 150

7.4 Summary 151

References 152

Chapter 8 Conclusion and Outlook 155

8.1 Overview of the Research 155

8.2 Work Done and Contribution 156

References 161

List of Figures and Tables

Figure 2.1: Energy band diagram of a *p-n* junction 12
Figure 2.2: Illustration of JV curve 16
Figure 2.3: Limiting efficiency curve for single-junction solar cells 18
Figure 2.4: Basic perovskite crystal structure 21
Figure 2.5: Tolerance factors for halide perovskites 25
Figure 2.6: Schematic of dye-sensitized solar cell 27
Figure 2.7: Tandem device 31
Figure 2.8: Charge transport of perovskite solar cells 33
Figure 2.9: Vapour deposition system for perovskite film 37

Figure 3.1: Kurt J. Lesker Mini Spectros system 51

Figure 4.1: Statistics of solar cells optimisation 67
Figure 4.2: DSVD system and characterisation of the DSVD's films 68
Figure 4.3: Thin-film topology of the DSVD's films 71
Figure 4.4: Comparison of the annealed and unannealed DSVD's films. 72
Figure 4.5: Optical properties of the DSVD's films 74
Figure 4.6: DSVD's solar cell performance 75

Figure 5.1: Fabrication procedures of the SVD 90
Figure 5.2: XRD of the SVD's films 92
Figure 5.3: XRD of the DSVD's films 96
Figure 5.4: PL of the SVD's and DSVD's films 97
Figure 5.5: Absorption spectra of the SVD's and DSVD's films 100
Figure 5.6: Thin-film topology of the SVD's and DSVD's films. 102
Figure 5.7: SVD's and DSVD's solar cell performance 104
Figure 5.8: Thermal stability of the SVD's and DSVD's films. 105

Figure 6.1: FTPS experiment design 116
Figure 6.2: Illustrations of perovskite solar cells with various configurations. . 117
Figure 6.3: Forwards and backwards J-V curves of perovskite solar cells 119
Figure 6.4: Stabilised maximum power output. 123
Figure 6.5: Schematic representation of the intrinsic doping 125
Figure 6.6: Stabilided power at various titania precursor concentrations. 126
Figure 6.7: Illustration of the proposed charging effect under forward bias. 128
Figure 6.8: J-V curves of cells without Ti-CL or spiro-OMeTAD layers 129
Figure 6.9: FTPS measurement 131

Figure 7.1: Schematic of an inverted single-junction device 144
Figure 7.2: Schematic of a tandem cell 145

Figure 7.3: Characterisation of the wide bandgap bottom sub-cell 147
Figure 7.4: J-V curves of the wide bandgap bottom cell 148
Figure 7.5: J-V curves and SEMs of the top cell 150
Figure 7.6: SEMs images of the tandem cell 151

Figure 8.1: Summary of research steps.....156

Table 2.1: Structural data for $CH_3NH_3PbX_3$ (X=Cl, Br, I) 24

Table 4.1: Tooling factor measurement for the DSVD processing 65
Table 4.2: Optimised deposition conditions of the DSVD processing.....66
Table 4.3: Solar cell performance from the DSVD and spin-coating.....76

Table 5.1: Tooling factor measurement for the SVD processing 86
Table 5.2: Compositions of precusors for the SVD processing.....87
Table 5.3: Optimised deposition conditions of the DSVD processing 88
Table 5.4: Solar cell performance from the SVD and DSVD fabrications.....104

Table 6.1: Device performance of perovskite cells at various configurations...121

Nomenclature

Fundamental Constants

h	Planck's constant
c	speed of light in vacuum
k_B	Boltzmann constant
q	charge on the electron

Symbols Used in the Thesis

η	power conversion efficiency (PCE)
λ	wavelength of light
v	frequency of light
τ	lifetime
t	tolerance factor
μ	octahedral factor
b_s	incident spectral photon flux density
E	energy
E_g	bandgap energy
FF	fill factor
I	current
J	current density
J_0	reverse saturation current density
J_{sc}	short circuit current density
J_{dark}	dark current density

P_s	power density
P_m	maximum power density
QE	quantum efficiency
T	device operating temperature
V	voltage or bias
V_{oc}	open circuit voltage

Acronyms

a-Si	amorphous silicon
AFM	Atomic Force Microscopy
AM1.5	air mass 1.5 spectrums – standard for solar cell calibration
AMR	approximate molar ratio
c-Si	crystalline silicon
CB	conduction band
CdTe	cadmium telluride
CIGS	copper indium gallium selenide
DMF	dimethylformamide
DSSC	dye-sensitized solar cell
DSVD	dual-source vapour deposition
EQE	external quantum efficiency
FB-SC	forward bias to short circuit
FTIR	Fourier Transform Infrared Spectrophotometer
FTO	fluorine-doped tin oxide
FTPS	Fourier Transform Photocurrent Spectroscopy
GaAs	gallium arsenide

GBL	γ-butyrolactone
HTM	hole transport material
InP	indium phosphide
IPCE	incident photon-to-current efficiency
JV	current density-voltage
MA	methylammonium (CH_3NH_3)
MAX	methylammonium halide (CH_3NH_3X)
MAI	methylammonium iodide (CH_3NH_3I)
MABr	methylammonium bromide (CH_3NH_3Br)
MACl	methylammonium chloride (CH_3NH_3Cl)
MSSC	meso-superstructured perovskite solar cell
p-i-n	positive-intrinsic-negative
PbX_2	lead halide
OLED	organic light emitting diode
PCBM	[6,6]-Phenyl-C61-butyric acid methyl ester
PCE	power conversion efficiency
PEDOT:PSS	poly(3,4-ethylenedioxythiophene):poly(4-styrenesulfonate)
PL	photoluminance
PMMA	polymethyl methacrylate
PV	photovoltaic
QE	quantum efficiency
ssDSSC	solid-state dye-sensitized solar cell
spiro-OMeTAD	2,2',7,7'-Tetrakis(N,N-p-dimethoxyphenylamino)-9,9'-spirobifluorene

SC-FB	short circuit to forward bias
SEM	Scanning Electron Microscopy
STC	Standard Test Conditions
SVD	sequential vapour deposition
TCSPC	time-correlated single photon counting
Ti-CL	tatinia (TiO_2) compact layer
VB	valence band

Chapter 1

Introduction

1.1 Background Motivation

Global energy consumption continues to rise at an alarming rate, primarily due to the increasing global population and a rapidly evolving industrial economy. The estimated consumption stood at 524 quadrillion British thermal units (Btu) in 2010, and has been projected to reach 824 quadrillion Btu in 2040 based on an average annual growth of 1.5 percent.[1] Traditional forms of energy such as fossil fuels (i.e. liquid fuels, natural gas, and coal), continue for the majority of the world's energy demands, and are still expected to supply more than three-quarters of the total required amount by the year 2040.[1] On the subject of environmental sustainability, carbon dioxide which is an unavoidable by-product of fossil fuel combustion, is a major contributor to anthropogenic greenhouse gas emissions worldwide, and the subsequent rising of global temperatures.[2] The persistence of current trends is likely to result in catastrophic consequences on weather patterns, frequency of coastal flooding, natural

ecosystems, and the future of the human society in general.[2] Carbon dioxide emissions must therefore be reduced significantly within the next 20-30 years to avoid the unwanted stimulation of these adverse effects.[3]

To meet the aforementioned energy challenges, intensive research has been conducted on potential alternative renewable, affordable, and clean energy sources as well as their specific applications. Solar power, despite being the most abundant of all natural energy resources, generated only 34 billion kilowatt hours (kWh) of electricity in 2010.[4] With progressive innovation, research, and development in the renewable energy sector, this number is expected to rise to 452 billion kWh by 2040.[4]

Amongst the various categories of solar technological devices, photovoltaic (PV) cells have shown the most promise owing to their ability to directly generate electrical power through the absorption of sunlight. PV technology therefore has been the focus of much institutional and industrial research in recent decades. Gallium arsenide (GaAs)-based solar cells yield power conversion efficiencies reaching 28.8%. However, the production cost involved is too high for widespread commercialisation.[5,6] On the other hand, silicon based thin film solar cells have been widely commercialised and utilised for residential and industrial applications as they currently dominate the PV market and they possess power conversion efficiencies (PCEs) approaching 25% (crystalline Si).[7] Nonetheless, due to the indirect bandgap, characteristic of silicon, the thickness of the semiconducting layer required to form an efficient solar cell needs to be in the order of hundreds of micrometres to gain enough light absorption. This results in highly complicated and expensive fabrication processes, further limiting the material's usage in the energy supply industry. Thus, much focus has been placed on the alternatives of thin film solar cells, especially,

those based on amorphous and nanocrystalline silicon, or direct band-gap semiconductor materials. The following instances illustrate the nature of issues currently being encountered in the thin film PV research field: 1) Cadmium telluride solar cells has reached 19.6% in laboratory and 17.5% for its module efficiency; however, the toxicity of cadmium possibly causes environmental hazards;[5,8,9] 2) Copper indium gallium selenide (CIGS), another direct band gap material, has been reported to exhibit a power conversion efficiency of 20.5%; in this case, wide scale production is limited by the complexity of fabrication as well as the unavailability of indium which is a rare element.[5,10] It is thus, evident that lengthy financial and energy payback times are currently hindering the widespread adoption of such photovoltaic devices.

The discovery of sustainable photovoltaic materials capable of delivering high efficiency is the key. Liquid-electrolyte dye-sensitized solar cells (DSSCs), originally developed in 1991 by Brian O'Regan and Michael Gratzel, emerged as a low cost alternative to conventional solar PV cells.[11] Recently, the record PCE of liquid-electrolyte DSSCs reached 12.3%.[12] Nevertheless, one of the major concerns associated with designing a DSSC, involves the utilisation of a highly-corrosive and thermally-unstable liquid electrolyte which severely degrades the long-term device stability. Another factor deterring the commercial success of DSSCs is the scaling up of current devices to large-area arrays on conducting glass, in order to facilitate reel-to-reel fabrication.[13]

Hybrid organic-inorganic halide perovskite absorbers have drawn a great deal of attention recently.[14,15,16,17] Inspired by the concept of DSSCs, perovskite-sensitized solar cells were initially proposed to operate in a manner analogous to DSSCs,

substituting the dye with a perovskite layer as the light absorber.[15,16] In 2012, a meso-superstructured perovskite solar cell (MSSC) incorporating an insulating alumina (Al_2O_3) layer boosted the power conversion efficiency (PCE) over 12%.[18] Within a few months, perovskite-based solar cells rapidly achieved PCE values capable of competing with the DSSC record PCE of 12.3%, demonstrating great potential to perform better in the near future.[19] Research into hybrid perovskites as PV materials was however, still in its infancy, and numerous challenges emerged simultaneously. Driving power conversion efficiency upwards while developing feasible large-volume fabrication techniques is crucial to realising high-volume commercial applications for perovskite based photovoltaic devices.

1.2 Goals of the Thesis

This thesis reports on a series of experimental studies involving the development of efficient perovskite solar cells, fabricated specifically by vapour deposition techniques. Vapour deposition is a mature technique employed in large-scale manufacturing, ideally for the fabrication of extremely uniform thin-films with fine tuning control.[6,20] It has been widely used for the mass production of high efficiency inorganic multi-junction solar cells.[20,21,22,23,24] Originally, hybrid organic-inorganic perovskite films were produced through the spin-coating of a single precursor solution, such as dimethylformamide (DMF), [18,19] or γ-butyrolactone (GBL),[17] generally resulting in non-uniform films which possibly induce inhomogeneous charge generation and shunting paths within the perovskite layer. Furthermore, the determination of appropriate solvents capable of dissolving the source components presented additional difficulties, limiting the broadening of perovskites into varieties.[25]

This thesis commences in Chapter 2, with an introduction of the structure and

operating principles of perovskite solar cells fabricated based on different configurations. The necessary fabrication techniques relevant to the perovskites are also explained in detail in Chapter 2. The experimental methods including the synthesis of precursors, device assembly, and characterisation techniques are presented in Chapter 3. Chapter 4 delves into the pioneering work entailing a dual-source vapour deposition (DSVD) technique for fabricating efficient planar heterojunction mixed-halide perovskite ($CH_3NH_3PbI_{3-x}Cl_x$) solar cells. This chapter confirms that mixed-halide perovskite materials can be formed entirely from solid-state materials under vacuum with outstanding film quality. More importantly, it illustrates the capability of mixed-halide perovskite materials to produce efficient solar cells in thin-film architecture. Lastly, a comparison between perovskite films fabricated by the DSVD technique and the conventional spin-coating technique clearly highlights the superiorities of the vapour-deposited films in Chapter 4.

To further expand the vapour deposition techniques and to gain an insight into the properties of the vapour-deposited perovskite films, a follow-up study in Chapter 5 introduces a two-layer sequential vapour deposition (SVD) technique for the fabrication of planar heterojunction single halide perovskite ($CH_3NH_3PbI_3$) devices. An investigation into the crystallographic and photo-physical properties of the resultant films clarifies that an appropriate composition of the precursors reacting in the fabrication process determines material properties, and an optimal annealing condition improves the crystallinity of the perovskite films. A parallel comparison in Chapter 5 between the perovskite films fabricated by the SVD and DSVD techniques leads to the identification of the merits and drawbacks associated with each technique from various perspectives such as their crystal formation, carrier lifetime, film quality and corresponding device performance. Integrating the optimised perovskite films

derived from both (SVD and DSVD) fabrication techniques, results in remarkable PCEs. The study in Chapter 5 delivers a better understanding of the fundamental properties of the vapour-deposited perovskite films, further promoting the advantages of this fabrication method.

Despite the ability of both mixed-halide and single halide perovskite solar PV cells to exhibit high PCEs, hysteresis is observed during the photocurrent density-voltage (J-V) characterisation of both planar heterojunction and meso-superstructured solar cells. This is a common phenomenon in perovskite-based solar cells.[26,27] In Chapter 6, an investigative study on the hysteretic behaviour in solution-processed perovskite devices with various configurations is conducted in order to facilitate a systematic comparison and understanding, especially, since the MSSCs could not be optimised via vapour deposition methods. The comparison between devices in different configurations shows that the perovskite devices without compact layers exhibit unusual high PCEs under fast J-V scans. These high PCEs however, are not maintained at stabilised maximum power points. This behaviour is suggestive of a short-lived effect existing within the perovskite-based devices, enabling them to function temporarily. This short-lived effect is caused by a temporary built-in-field that is also responsible for the hysteresis in these perovskite devices. Chapter 6 therefore extensively analyses the possible contributing factors to the short-lived effect as well as the built-in-field. Additionally, to further evaluate the extent of hysteresis in the different devices, a Fourier Transform Photocurrent Spectroscopy (FTPS) method is developed to measure the hysteretic loops of the devices. This technique allows for the consistent evaluation of the hysteresis level of each device regardless of the scan conditions (i.e., scan rate). The understanding gained in Chapter 6 provides a new perspective on the functionality of each layer, giving an insight on

supplementary ways to boost efficiency.

Combining the advantages of the vapour deposition technique identified in Chapter 4 and Chapter 5, with the understanding gained on the operating mechanisms of perovskite devices in Chapter 6, Chapter 7 introduces an ongoing exploratory study on an “all-perovskite” tandem PV device. This tandem device consists of a vapour-deposited perovskite sub-cell on top and a solution-processed perovskite sub-cell at the bottom. Although the performance of both sub-cells is still undergoing optimisation, the demonstration of an “all-perovskite” tandem photovoltaic device shows the versatility of perovskite films, and their potential for wider commercialisation.

To summarise, the primary objective of this thesis involved the exploration of new vapour deposition techniques to fabricate efficient hybrid organic-inorganic perovskite solar cells based on planar heterojunction architecture. The vapour deposition techniques successfully boost the power conversion efficiency, and clearly demonstrate the feasibility of fabricating high efficiency perovskite thin film devices, thus, paving the road to commercialisation. Additionally, the thesis studies the relevance of acquiring further understanding of the fundamental properties and operation principles of perovskite films, as they are key factors to further developing perovskite PV technology. Enhanced performance, improved understanding of the associated fundamental mechanisms and a broader range of research activities, are clearly highlighted in the conclusion of the thesis as vital factors to focus on, in order to realise maximum potential pertaining to perovskite solar PV cell technology.

References

1. Annual Energy Outlook 2014 - Energy Information Administration. at <http://www.eia.gov/forecasts/aeo/>

2. Intergovernmental Panel on Climate Change. *Fifth Assessment Report - Climate Change 2014: Impacts, Adaptation and Vulnerability*. (2014). at <http://www.ipcc.ch/report/ar5/wg2/>

3. Anderson, K. & Bows, A. Beyond "dangerous" climate change: emission scenarios for a new world. *Philos. Trans. A. Math. Phys. Eng. Sci.* **369,** 20–44 (2011).

4. Leahy, M. *et al.* International Energy Outlook 2013.

5. Green, M. A., Emery, K., Hishikawa, Y., Warta, W. & Dunlop, E. D. Solar cell efficiency tables (version 44). *Prog. Photovoltaics Res. Appl.* **22,** 701–710 (2014).

6. Chopra, K. L., Paulson, P. D. & Dutta, V. Thin-Film Solar Cells: An Overview. *Prog. Photovoltaics Res. Appl.* **12,** 69–92 (2004).

7. Green, M. A., Emery, K., Hishikawa, Y., Warta, W. & Dunlop, E. D. Solar cell efficiency tables (version 42). *Prog. Photovoltaics Res. Appl.* **21,** 827–837 (2013).

8. Shah, A., Torres, P., Tscharner, R., Wyrsch, N. & Keppner, H. Photovoltaic Technology: The Case for Thin-Film Solar Cells. *Science.* **285,** 692–698 (1999).

9. Fthenakis, V. M. & Moskowitz, P. D. Thin-film Photovoltaic Cells: Health and Environmental Issues in their Manufacture Use and Disposal. *Prog. Photovoltaics Res. Appl.* **3,** 295–306 (1995).

10. Green, M. A. Thin-film solar cells: review of materials, technologies and commercial status. *J. Mater. Sci. Mater. Electron.* **18,** 15–19 (2007).

11. O'Regan, B. & Grätzel, M. A low-cost, high-efficiency solar cell based on dye-sensitized colloidal TiO_2 films. *Nature* **353,** 737 (1991).

12. Yella, A. *et al.* Porphyrin-sensitized solar cells with cobalt (II/III)-based redox electrolyte exceed 12 percent efficiency. *Science* **334,** 629–34 (2011).

13. Snaith, H. J. & Schmidt-Mende, L. Advances in Liquid-Electrolyte and Solid-State Dye-Sensitized Solar Cells. *Adv. Mater.* **19,** 3187–3200 (2007).

14. Kojima, A., Teshima, K., Shirai, Y. & Miyasaka, T. Novel Photoelectrochemical Cell with Mesoscopic Electrodes Sensitized by Lead-halide Compounds (11). *Meet. Abstr.* **MA2008-02,** 27 (2008).

15. Kojima, A., Teshima, K., Shirai, Y. & Miyasaka, T. Organometal halide perovskites as visible-light sensitizers for photovoltaic cells. *J. Am. Chem. Soc.* **131,** 6050–6051 (2009).

16. Im, J.-H., Lee, C.-R., Lee, J.-W., Park, S.-W. & Park, N.-G. 6.5% efficient perovskite quantum-dot-sensitized solar cell. *Nanoscale* **3,** 4088–93 (2011).

17. Kim, H.-S. *et al.* Lead iodide perovskite sensitized all-solid-state submicron thin film mesoscopic solar cell with efficiency exceeding 9%. *Sci. Rep.* **2,** 591 (2012).

18. Lee, M. M., Teuscher, J., Miyasaka, T., Murakami, T. N. & Snaith, H. J. Efficient Hybrid Solar Cells Based on Meso-Superstructured Organometal Halide Perovskites. *Science* **338,** 643–647 (2012).

19. Ball, J. M., Lee, M. M., Hey, A. & Snaith, H. J. Low-temperature processed meso-superstructured to thin-film perovskite solar cells. *Energy Environ. Sci.* **6,** 1739–1743 (2013).

20. Yang, F., Shtein, M. & Forrest, S. R. Morphology control and material mixing by high-temperature organic vapor-phase deposition and its application to thin-film solar cells. *J. Appl. Phys.* **98,** 014906 (2005).

21. Chopra, K. L., Paulson, P. D. & Dutta, V. Thin-film solar cells: an overview. *Prog. Photovoltaics Res. Appl.* **12,** 69–92 (2004).

22. Sugo, M., Takanashi, Y., Al-jassim, M. M. & Yamaguchi, M. Heteroepitaxial growth and characterization of InP on Si substrates. *J. Appl. Phys.* **68,** 540 (1990).

23. Dupuis, R. D. III-V semiconductor heterojunction devices grown by metalorganic chemical vapor deposition. *IEEE J. Sel. Top. Quantum Electron.* **6,** 1040–1050 (2000).

24. King, R. R. *et al.* 40% efficient metamorphic GaInP⁄GaInAs⁄Ge multijunction solar cells. *Appl. Phys. Lett.* **90,** 183516 (2007).

25. Günes, S., Neugebauer, H. & Sariciftci, N. S. Conjugated Polymer-Based Organic Solar Cells. *Chem. Rev.* **107,** 1324–1338 (2007).

26. Snaith, H. J. *et al.* Anomalous Hysteresis in Perovskite Solar Cells. *J. Phys. Chem. Lett.* **5,** 1511–1515 (2014).

27. Sanchez, R. S. *et al.* Slow Dynamic Processes in Lead Halide Perovskite Solar Cells. Characteristic Times and Hysteresis. *J. Phys. Chem. Lett.* **5,** 2357–2363 (2014).

Chapter 2

Background

This section presents an introduction to the fundamental operating principles of photovoltaic devices, and subsequently a special focus on perovskite solar cells. For more detailed information on operating principles of photovoltaic devices and molecular perovskite structure, the reader is referred to the standard texts by Nelson *et al*[1] and Mitzi *et al*[2] respectively.

2.1 Operating Principles of Photovoltaic Devices

The direct conversion of light to electrical energy in photovoltaic (PV) devices is governed by the physical phenomenon known as the photovoltaic effect that was discovered in 1839 by Edmund Becquerel.[3] Light consists of quantum packets of energy called photons, which are capable of transferring their energy to valence electrons in semiconducting materials.[4] Semiconductors provide a medium for the absorption of light photons, and the subsequent generation of electric charge carriers

in conventional PV devices.

A semiconductor can be characterised by the available energy states it possesses which form two crucial bands –valence band (VB) (i.e., the highest occupied band) and conduction band (CB) (i.e., the lowest unoccupied band). Both bands are separated by an energy gap of forbidden states assigned to E_g. Electrons in the VB can either be thermally excited or photo-excited into the CB, thus creating vacancies in the VB previously occupied by electrons. These vacancies are known as "holes" in the VB. Similarly to the negatively charged electrons in the CB, holes in the VB are considered mobile particles in their own respect, capable of movement, depending on the displacement of electrons in the lattice but with a positive charge. When sunlight is incident a solar cell, the photons within the ultraviolet, visible, and infrared regions of the solar spectrum can be reflected, transmitted, or absorbed by the cell depending on the bandgap energy (E_g) of the semiconductor constituting the cell. If absorption occurs, the mobile electrons and holes generated in the CB and VB respectively permit the semiconductor to be conductive.

Collecting the resulting electrons and holes at opposite electrodes generates a photocurrent. It is worth noting that, a photon is only capable of exciting electrons in a semiconductor if its energy E, is equal to or greater than the bandgap energy E_g of the semiconducting material. The energy of a photon is given by the Planck-Einstein equation as

$$E = h\nu = \frac{hc}{\lambda}$$

where h is Planck's constant, ν is the frequency of the light wave, λ is the wavelength of the light incident on the PV cell, and c is the speed of light in vacuum.

Since the generation of electric charge carriers in the CB and the VB can only occur if E matches or exceeds E_g, it is evident that the bandgap energy of the semiconducting material determines the section of the solar spectrum relevant for absorption by a given solar cell, as well as the maximum current that can be generated.

A built-in asymmetry is required to prevent the recombination of electrons and holes in a semiconductor and to facilitate the flow of current in one direction rather than other. A *p*-*n* junction architecture as depicted in Figure 2.1, is generally employed to establish this built-in electric field, providing the force required to propel the electrons and holes in opposite directions, thus, maintaining the separation of opposite charge carriers. Consequently, the photocurrent flows in the same direction as the built-in electric field.

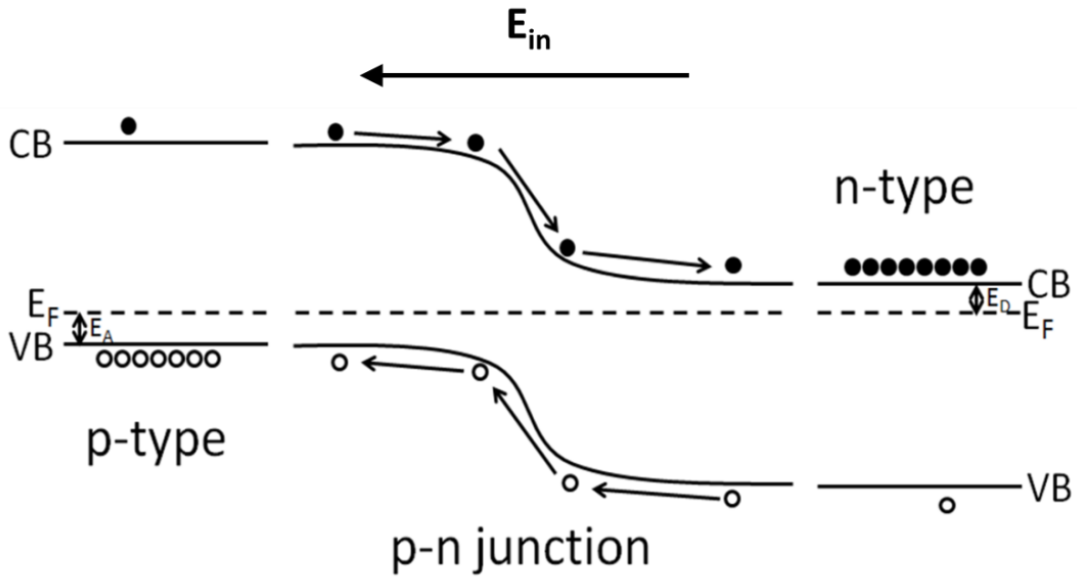


Figure 2.1: Energy band diagram of a *p*-*n* junction. CB is the conduction band, VB is the valence band, E_D is the donor binding energy, E_A is the acceptor binding energy, E_F is the Fermi level and E_{in} is the built-in electric field having the same flow direction as the generated photocurrent.

A *p*-*n* junction is a bi-layer structure comprising of a *p*-type semiconductor and an *n*–type semiconductor with excess holes and electrons respectively. Owing to the

difference in electron and hole concentrations on both sides, there is a tendency for holes to diffuse from the *p*-side to the *n*-side and for electrons to diffuse from the *n*-side to the *p*-side in the opposite direction. As a result, a depletion region where no mobile charges are present is formed. The net charge of the immobile dopant ions at close proximity to the junction on the *p*-side and *n*-side, therefore respectively become negative and positive.

The resulting double layer of charges forms the electric field, which in turn creates an internal potential drop at the junction. Hence, when photons are incident on the *p*-*n* junction, it is this built-in electric field that separates the additional holes and electrons generated. The free carriers produced successively travel through the crystal lattice until they are collected at the opposite electrodes. Photocurrent is thus generated and transferred to the external circuit.

To summarise, the operation mechanism of solar cells in power generation mode can be condensed into three fundamental processes:

1. Absorption of light and generation of the electric charge carriers;

2. Separation of the charge carriers at the *p*-*n* junction;

3. Collection of the charge carriers at opposite electrodes of the junction.

2.2 Solar cell Characterisation

As described above, the absorption of light photons in the semiconductor generates charge carriers which are subsequently driven towards opposite contacts by the built-in electric filed asymmetry. This charge separation induces photovoltage and

photocurrent in open circuit and short circuit conditions respectively.

The incident light intensity and its wavelength determine the photocurrent generated by a cell in short circuit mode. To relate the photocurrent density to the incident light spectrum, quantum efficiency (*QE*) of a cell is defined as the probability that a photon of energy *E* generates one electron to the external circuit,

$$J_{SC} = q \int b_s(E) QE(E) dE$$

where q is the electronic charge, $b_s(E)$ is the incident spectral photon flux density.

A potential difference is built up across a load's terminals when powered by a solar cell. This potential difference generates a dark current, which flows in the opposite direction to the photocurrent. This in turn reduces the value of the net current from its initial short circuit value. Moreover, the presence of a *p-n* junction in the solar cell causes the cell to exhibit basic diode-like qualities in the dark. Considering this case of an ideal diode, it allows the flow of a much larger current under forward bias ($V>0$) than reverse bias ($V<0$) in the dark. The dark current density $J_{dark}(V)$ is given by:

$$J_{dark}(V) = J_0 \left(e^{\frac{qV}{k_B T}} - 1 \right),$$

where the reverse saturation current density J_0 is constant, k_B is the Boltzmann constant, q is the electronic charge and T is the device operating temperature in Kelvin. The corresponding photocurrent density-voltage (*J-V*) response of the solar cell can be approximated as superposition of the short circuit current density and the dark current density resulting in the Shockley solar cell equation which gives the net current density in the cell:

$$J(V) = J_{SC} - J_{dark}(V)$$

The open circuit voltage, V_{oc}, is the maximum potential difference when the load is isolated. This is equivalent to the condition when the dark current and short circuit current exactly neutralise each other. Thus,

$$V_{oc} = \frac{kT}{q} ln(\frac{J_{sc}}{J_0} + 1)$$

Usually, the power delivered from an electric power source is defined as the product of voltage and current, i.e., $P = IV$. If the current is replaced by the current density, the cell power density is expressed as

$$P = JV$$

Figure 2.2 shows that the product of the photocurrent density and voltage is positive while the solar cell is under illumination. The cell generates power when the bias voltage is in a range within 0 and $V_{oc.}$ The maximum power density P_m occurs somewhere between 0 and V_{oc}, at a voltage V_m with a corresponding current density J_m.

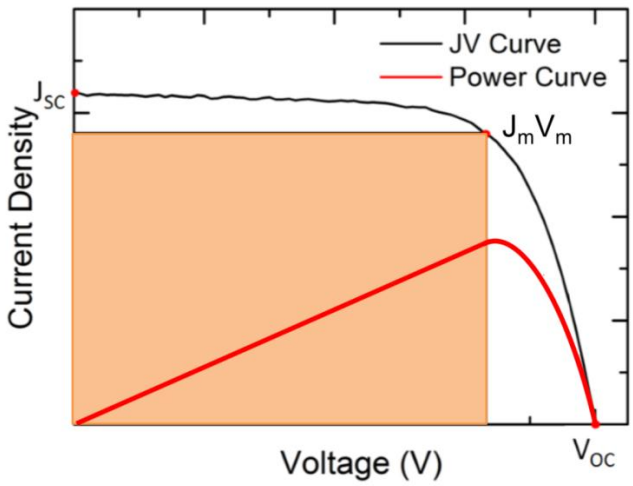


Figure 2.2: Illustration of a photocurrent density-voltage (JV) curve for a solar cell under illumination. The shaded area corresponds to the maximum attainable power output at $J_m V_m$.

The power conversion efficiency η of the cell is a measure of its overall performance, and it can be expressed as the ratio of the maximum power density at $J_m V_m$ to the overall incident light power density, P_s.

$$\eta = \frac{J_m V_m}{P_s}$$

Another parameter essential to the electrical characterisation of solar cells is the fill factor *FF*. It is obtained from the ratio,

$$FF = \frac{J_m V_m}{J_{sc} V_{oc}}$$

and is generally known as the 'squareness' of the *J-V* curve. It gives a measure of the amount of the open circuit voltage and short circuit current "utilised" at maximum power. The conversion efficiency equation can therefore be rewritten to incorporate the relationship between $J_{sc,}$ V_{oc} and *FF* as follows:

$$\eta = \frac{J_{sc} V_{oc} FF}{P_s}$$

J_{sc}, V_{oc}, FF and η are the key performance parameters required for the electrical characterisation of a solar cell. All four parameters should be obtained under specific illumination conditions. The Standard Test Conditions (STC) for solar cells specifies an Air Mass (AM) 1.5 spectrum[5], an incident power density of 1000 Wm^{-2} at temperature of 25^{o}C. [1]

Amongst the factors which adversely affect the performance of a photovoltaic cell, the following three are considered to dominate:

1. Incomplete absorption of incident light;
2. Non-radiative recombination of photo-generated carriers;
3. Voltage drop due to the series resistance attributed from the cell material. This limits the available power.

Moreover, it is important to understand how material-associated factors correlate to photovoltaic performance parameters. For instance, consider two hypothetical solar cells that have no other differences besides the bandgap energy level of the light absorbing materials in each device. This difference in bandgap energy results in changes in the absorption onset that will be reflected in the *JV* characteristics. The cell with the narrower band gap will absorb more photons and therefore generate a higher J_{sc}, but will also have a lower V_{oc} because the difference in Fermi level for holes and electrons is smaller, vice versa for the other cell with a larger band gap. Due to this inherent trade-off between current and voltage, it is necessary to discover an optimum semiconductor for achieving the maximum power conversion efficiency (PCE). As shown in Figure 2.3, the ideal bandgap energy for a solar cell with a single absorbing

transition layer is around 1.4 eV according to the Shockley-Queisser-Limit. This yields a theoretical maximum PCE of 33.7% when illuminated under an AM 1.5 spectrum.

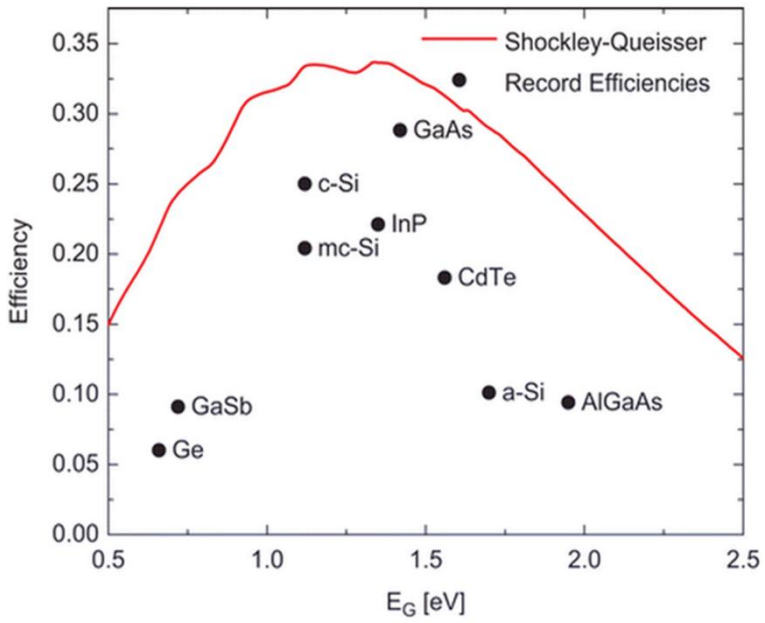


Figure 2.3: Limiting efficiency for single-junction solar cells under AM1.5 illumination from calculation (red curve). The points represent the best experimental single bandgap cells fabricated to date. This figure is reprinted from ref.6 updated on 10 July 2014

Gallium arsenide (GaAs) and indium phosphide (InP), have bandgaps of 1.42 eV and 1.35 eV at 300 K respectively which are very close to the optimum value. As a result, they are both highly favoured for use in high efficiency solar cells. Nonetheless, the high cost of materials and fabrication restricts their applications from expanding into the commercial mass production of terrestrial PV modules.[6]

Regarding silicon-based solar cells, amorphous silicon solar cells which are the dominant Si-based thin-film solar cells have quite a low stabilised module efficiency, generally in the range of 8~10%.[7] Moreover, monocrystalline silicon (c-Si) solar cells exhibit the highest power conversion efficiency (PCE) - as high as 25%.[8] However,

the complexity of their fabrication process leads to high capital costs per unit power output.

Cadmium telluride (CdTe) and copper indium gallium diselenide (CIGS) based cells have also been developed for thin film photovoltaics in manufacturing industries, and their module outputs have been stabilised at 17.5% and 15.7%, respectively.[8] On the other hand, cadmium Cd is highly toxic and its use is limited by environmental restrictions. Another long-term issue with these thin film technologies is the availability of resources such as indium.[9] This emphasises the need for more environmental-friendly materials for PV applications.

Apart from the PV technologies based on inorganic cells, organic and hybrid inorganic-organic solar cells have raised much attention. Organic solar cells, such as polymer based solar cells, have advantages such as: inexpensive fabrication, flexibility, and customisability on the molecular level. Nonetheless, they are relatively unstable in air, suffer photochemical degradation, and have only been able to approach 10% efficiency in laboratory experiments.[10] Hybrid inorganic-organic solar cells such as dye-sensitized solar cells (DSSCs) combine useful properties of each organic and inorganic component within a single device, but their long-term stability and low efficiency slow down their application in a commercial environment.[11,12]

In a nutshell, any materials which are easy to process, inexpensive and abundant, can be incorporated with the aim of delivering high efficiency solar cells. On this note, hybrid inorganic-organic perovskite solar cells are currently of great interest to PV researchers.

2.3 Perovskite and Perovskite Solar Cells

2.3.1 Perovskite Properties

"Perovskite" is the nomenclature for any material that adopts the same crystal structure as calcium titanate $CaTiO_3$, or more generally employs a compound material of stoichiometry in AMX_3 as shown in Figure 2.4. This simple structure consists of a three-dimensional (3-D) network of corner-sharing MX_6^{4-} octahedra, where the A cation is located at interstices in 12-fold cuboctahedral coordination and the M atom is typically a metal cation locating in the centre of an octahedron.[2] X is an anion (usually O^{2-}, Cl^-, Br^-,I^- or S^{2-}) sitting in the corners with the appropriate charge to balance the A and M cations. There are many different materials that adopt this AMX_3 perovskite structure, but differ in properties associated with insulation, ferromagnetism, antiferromagnetism and most importantly, superconductivity[13]. The structure of inorganic perovskite system is usually distorted by cation displacement (e.g. $BaTiO_3$) or octahedral tilting (e.g. $CaTiO_3$). The exhibited ferroelectrical and antiferroelectrical properties in perovskite materials are often enhanced by these cation displacements.[2]

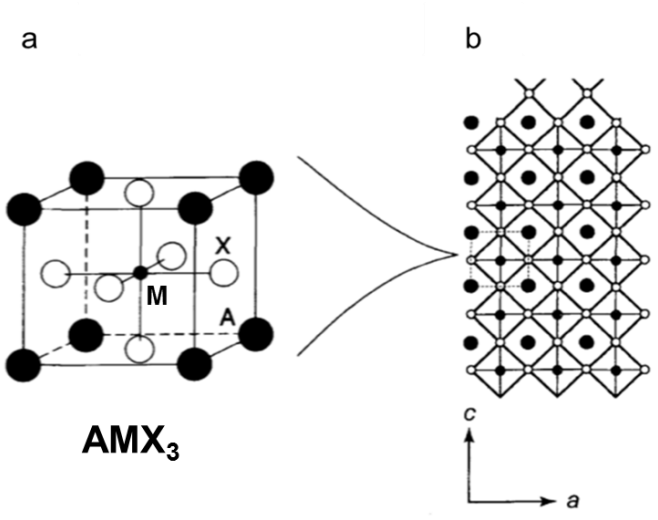


Figure 2.4: Basic perovskite crystal structure in AMX_3 form. (a) a 3-D structure (b) an extension of the structure from three dimensions. The dashed square on the right schematic corresponds to the unit cell shown on the left. This schematic is reprinted from ref.2.

More complex perovskite structures that integrate inorganic and organic components offer a substantial opportunity for tailoring new and functional materials. Many inorganic materials exhibit high electrical mobility, a variety of bandgaps, long thermally stability etc.[2] One the other hand, organic molecules usually have weaker interactions (e.g., hydrogen bonding and van der Waals) allowing for difference in topology, enhancement in luminescence, a large degree of polarisability etc. Hybrid organic-inorganic compositions generally deliver properties that are normally not achievable with either organic or inorganic materials alone. Their useful properties are integrated within a single material and also the molecular parameters (e.g., molecular length and width, polarisability, luminescent character etc.) can be more easily tuned. The categories of hybrid inorganic-organic perovskite have been comprehensively described by Mitzi *et al.*[2,14]

In this work, halide perovskite AMX_3 (X=halogen, Cl, Br or I) will be discussed in detail.

2.3.1.1 Influence of A Cation

The first-principles study has demonstrated that the electronic structure of halide perovskite AMX_3 is dominated by the characteristics of the M–X bond chains: on the one hand, the valence-band maximum is characterised as an antibonding-like hybridised state of the M-*m*s (Pb: *m* = 6) and the X-*n*p (*n*= 3, 4 or 5 for X=Cl, Br or I respectively) orbitals in the M–X chains. On the other hand, the conduction-band minimum is characterised as a non-bonding state of the M-*m*p and the X-*n*p orbitals.[15,16,17]

Although the A cation does not play a major role in determining the band structure of the AMX_3 perovskite, it neutralises the total charge within the lattice.[18] Nevertheless, since the size of various A cations deforms the MX_6^{4-} octahedron network, expansion or contraction of the lattice leads to change in the M-X bond length and consequently affects the bandgap of the perovskite.[19,20] As mentioned before, A cation must fit into a relatively small cuboctahedral hole shared by the 12 nearest X atoms and therefore it limits the choice of molecules for the A site. To describe the probable structure and stable crystallinity, a tolerance factor (*t)* and an octahedral factor *(μ)* are defined where *t* is defined as the ratio of the distance A-X to the distance M-X in an idealised solid-sphere model and μ is defined as the ratio of the ionic radius of M ion to the radius of X ion as below,[18,21,22]

$$t = \frac{R_A + R_X}{\sqrt{2}(R_M + R_X)};\ \ u = \frac{R_M}{R_X}$$

where R_A, R_M and R_X are the ionic radii of the corresponding ions. The tolerance factor *t* is restricted around the unity (*t*=1 corresponds to a perfect perovskite structure in cubic space group $pm\bar{3}m$) to have a stable, even distorted, 3-D perovskite structure.[23]

For all the known perovskite structures, the crystal structure always gives $0.81 < t < 1.11$ and $0.44 < \mu < 0.90$.[22]

Taking $APbI_3$ as an example, to maintain its cubic symmetry ($t \leq 1$), the value of the A ionic radius (R_A^+) may not be larger than 2.6 Å.[21,22] It has been proved that small monovalent cations, such as Rb^+, Cs^+, methylammonium (MA^+), or formanidinium (FA^+) can fit in the 3-D framework with the PbI_6^{4-} network.[24,25,26,27,28] Within the scope of this comparison, the ionic radius follows a trend of $R_{Cs}^+ < R_{MA}^+ < R_{FA}^+$.[18] On the other hand, it has been observed that $CsPbI_3$ absorbs up to a shorter wavelength than $MAPbI_3$, whereas $FAPbI_3$ absorbs to a longer wavelength than $MAPbI_3$.[28] Therefore, it can be concluded that the lattice is expanded with increasing the ionic radius of the A cation and consequently it leads to a decrease in bandgap of the perovskite and therefore causes a red-shift in the absorption onset. However, it is important to note that when the metal or the halide varies, the trend in the bandgap is totally changed.

In addition, despite these constraints in $APbX_3$, transitions between such structures on heating are common for any given perovskite. Taking $MAPbX_3$ as an example, its high-temperature phase is generally cubic. Since the symmetry of the free MA^+ ion exhibit C_{3v} symmetry that does not fit the theoretical O_h site symmetry for the A cation, the organic cation MA^+ has to be orientated to satisfy the O_h symmetry at the high-temperature phase to maintain the cubic perovskite structure.[29] Upon cooling, the structures of the perovskite distort to a lower symmetry as the motion of the MA^+ cation becomes more restricted.[2,30] Table 2.1 summarises the structural data for the trihalide perovskite $MAPbX_3$ (X=Cl, Br, I) and includes the transition temperature where the crystal orientates to another phase.

X	Temperature (K)	Crystal System	Space Group	*a* (Å)	*b* (Å)	*c* (Å)
Cl	>178.8	Cubic	$Pm\bar{3}m$	5.675		
	172.9-178.8	Tetragonal	*P*4/*mmm*	5.656		5.630
	<172.9	Orthorhombic	$P222_1$	5.673	5.628	11.182
Br	>236.9	Cubic	$Pm\bar{3}m$	5.901 (1)		
	155.1-236.9	Tetragonal	*I*4/*mcm*	8.322 (2)		11.832 (7)
	149.5-155.1	Tetragonal	*P*4/*mmm*	5.894 (2)		5.861 (2)
	<144.5	Orthorhombic	$Pna2_1$	7.979 (1)	8.580 (2)	11.849 (2)
I	>327.4	Cubic	$Pm\bar{3}m$	6.3285 (4)		
	162.2-327.4	Tetragonal	*I*4/*mcm*	8.855 (6)		12.659 (8)
	<162.2	Orthorhomic	$Pna2_1$	8.861 (2)	8.581 (2)	12.620 (3)

Table 2.1: Structural data for $CH_3NH_3PbX_3$ (X=Cl, Br, I). This table is modified from ref.2 and ref.31.

2.3.1.2 Influence of Metal Cation

Pb(II) and Sn(II) have been widely recognised for building 3-D halide perovskites, while only a limited study has been reported on the $AGeX_3$ 3-D perovskite (A = Rb, Cs; X = Cl, Br, I).[32,33,34] This is possibly due to the decrease in stability of the 2^+ oxidation state when moving up the group 14 elements on the periodic table (i.e., stability of Ge(II)< Sn(II)< Pb(II)).[32] As mentioned above, the bandgap of the halide perovskites is greatly affected by the X–M bond. For example, in AMI_3 system, the M–I–M bridging angles between the MI_6 octahedra (M = Ge, Sn, Pb) are 166.27(8)° for Ge, 159.61(5)° for Sn and 155.19(6)° for Pb which results in differences in the band structure.[16] Moreover, moving down the group 14 for the selection of the metal cation leads to an increase in the difference between the electronegativities of the M and I atoms. Consequently, it decreases the covalent character of the M–I bond and the band gap of this group of perovskites follows the trend of E_g ($AGeI_3$) < E_g ($ASnI_3$) < E_g ($APbI_3$).[35]

2.3.1.3 Influence of Halide Anion

Another major determining factor for the structural difference of the halide perovskites originates from the differences in the ionic radius of various X anions. Taking $MAPbX_3$ perovskites (where X = Cl, Br, and I) as an example, MA^+ in cation A has a radius of R_A=0.18 nm and Pb in cation M has a radius of R_M=0.119 nm. The X halogen anions, generally have radii of R_X=0.220 nm for iodine, R_X=0.196 nm for Br and R_X=0.181 nm for Cl respectively. Calculated and estimated *t* and μ factors for these lead halide perovskites are shown in Figure 2.5. It suggests that a smaller X ion radius is relatively beneficial for the formation or stability of the cubic structure (i.e., t→1).

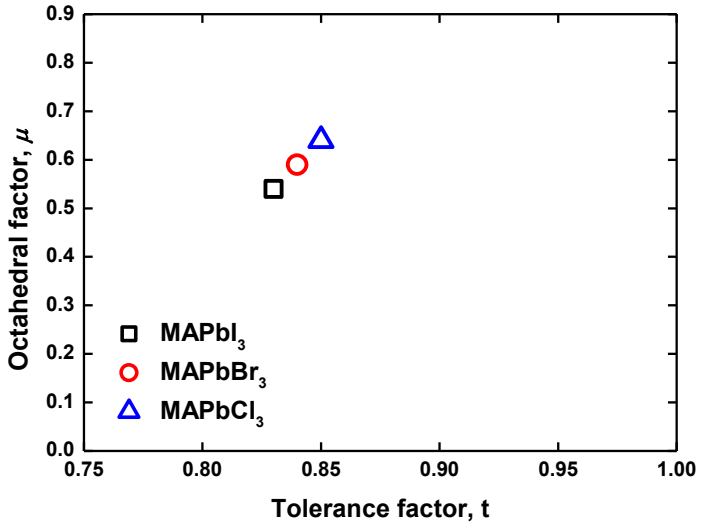


Figure 2.5: Calculated t and μ factors for $MAPbX_3$ halide perovskites. X=Cl, Br or I. The figure is modified from the ref.21.

Furthermore, with moving down the halogen group (Cl→Br→I), the electronegativity of the halogen atoms decreases and therefore the covalent character of the halogen bonding with Pb is enhanced, leading to a red shift of the bandgap from Cl to I in the

$MAPbX_3$ system.[15,36] It agrees with the trend from experimental data that $MAPbX_3$ employs a bandgap of 3.3 eV for Cl, 2.3 eV for Br and 1.5 eV for I respectively.[37,38]

Beyond the single halide perovskites, a perovskite structure which incorporates two halides (*e.g.* iodide with bromide $MAPbI_{3-x}Br_x$ or bromide with chloride $MAPbBr_{3-x}Cl_x$) allows for continuous tuning of the bandgap, since the difference in radii between the two halogens shifts the VB thus resulting in a change in the bandgap.[15] The bandgaps of $MAPbI_{3-x}Br_x$/$MAPbBr_{3-x}Cl_x$ can be tuned between 1.5eV/2.3 eV(x=0) to 2.3 eV/3.3 eV(x=3) respectively.[37,38,39] On the other hand, however, no obvious change on the absorption onset is observed in the case of iodide-chloride mixed perovskite $MAPbI_{3-x}Cl_x$, indicating that the incorporation of Cl^- into the PbI_6^{4-} octahedron is very difficult.[40] The reason could be possibly because the energy required for inserting a chlorine atom into the lead-iodine lattice is much larger than inserting a bromide atom.[41]

The above discussion suggests that the structure of halide perovskite (AMX_3) can be easily tuned by varying the combination of all the three cationic and anionic components. The semiconducting properties and optoelectronic properties of hybrid organic-inorganic perovskites have been extensively investigated since the early 1990's. Characteristics such as excitonic features have been capitalised on for devices such as transistors and light-emitting diodes.[2,42,43] However, research on the applications of perovskites in photovoltaic devices has until recently been inadequate. Perhaps, the conventional focus on layered "excitonic" materials was responsible for the lack of interest in the use of these materials for solar cell development. Meanwhile, whether these perovskite materials could effectively contribute to PV applications, still remained unknown until the last decade.

2.3.2 Perovskite-Sensitized Solar Cells

The employment of perovskite absorbers in solar cells initially evolved from DSSCs. DSSCs are a form of hybrid solar cells with an inorganic *n*-type mesoporous oxide (e.g., TiO_2) that is sensitized either with an organic or metal complex light-absorbing dye, and infiltrated with an organic *p*-type hole-conductor in the form of a liquid redox electrolyte.[11] In order to absorb the incident sun light efficiently, sufficient dyes are sensitized on the porous TiO_2 where should have adequate internal surface area. A schematic diagram depicting a typical dye-sensitized solar cell is shown in Figure 2.6.

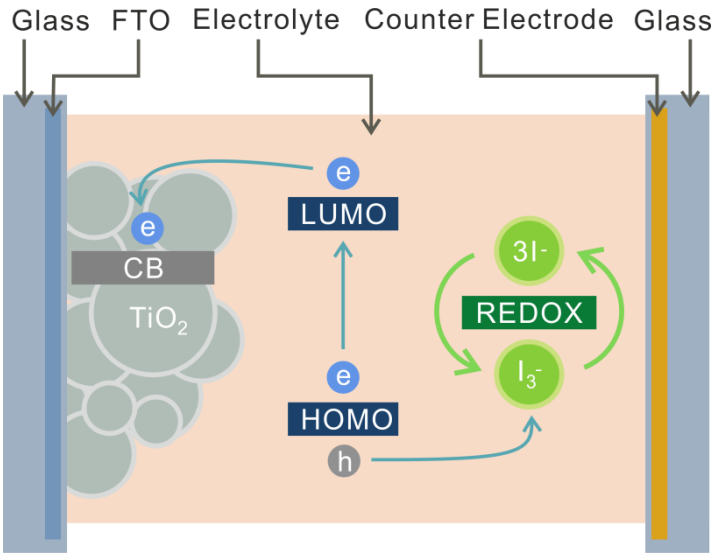


Figure 2.6: Schematic of dye-sensitized solar cell

The electrons are excited by absorbing photons from the highest occupied molecular orbital (HOMO) to the lowest unoccupied molecular orbital (LUMO) of the dye, and are subsequently collected at the fluorine-doped tin oxide (FTO) electrode via the TiO_2 mesoporous layer. Meanwhile, the other side of the dye is contacted by a redox active electrolyte - usually iodide/triiodide-based - which regenerates the oxidized dye molecules and transports the holes to the counter electrode, usually a platinum coated FTO. However, the use of a liquid electrolyte such as the archetypal redox couple

iodide/triiodide demands a rigorous sealing procedure to prevent leakages. This typical redox couple iodide/triiodide significantly degrades the stability of the cells due to its high corrosiveness. To overcome these challenges, a solid-state *p*-type hole transporter, 2,2',7,7'-Tetrakis(N,N-*p*-dimethoxyphenylamino)-9,9'-spirobifluorene (Spiro-OMeTAD), has been proposed to replace the liquid electrolyte, in order to create fully solid-state DSSCs (ssDSSCs).[44]

The replacement of the dye with perovskite as a light absorber does not affect the working principle of DSSCs. The first perovskite-sensitized solar cells employed hybrid inorganic-organic perovskite absorbers ($CH_3NH_3PbI_3$ or $CH_3NH_3PbBr_3$) with liquid iodide/triiodide redox couple electrolyte and exhibited a PCE of 2.2%.[45] Further optimisation on this type of perovskite-sensitized solar cells has since been developed to produce PCEs of 3.5%[46] and 6.5%[47] successively. However, these perovskite-sensitized solar cells based on the liquid electrolyte did not eliminate the problems of instability, and the perovskite absorber was rapidly decomposed in the electrolyte, inducing continual degradation in the cells within a few minutes.

To address these issues, $CH_3NH_3PbI_3$ and $CH_3NH_3PbI_{3-x}Cl_x$ perovskite-sensitized solar cells incorporating spiro-OMeTAD as the hole-transporters were achieved PCEs of over 9%[48] and 7%[49] respectively in 2012. Compared to most efficient ssDSSCs at the time, which achieved just over 7% efficiency[50], this breakthrough was a huge step forward in the development of solid-state sensitized solar cells.

One of the primary superiorities of the perovskite absorbers over the use of dyes is their strong absorbance over a broader spectrum of light, providing broader light absorption with films that are as thin as 500 nm. Therefore, perovskite absorbers

overcome the threshold thickness of solid-state solar cells around 2 microns beyond which has historically limited performance in terms of photocurrent generation.[51]

2.3.3 Meso-Superstructured Solar Cells

To further understand the charge transport mechanism in the halide perovskite solar cells, (i.e. whether the charge transport takes place within the perovskite phase or through the mesoporous TiO_2) the mesoporous TiO_2 was replaced with an insulating layer of Al_2O_3. Surprisingly, this not only resulted in a faster charge transport and a comparable photocurrent, but the open-circuit voltage had also increased by 200 mV to 300 mV, leading to a perovskite solar cell with 10.9% efficiency.[52] Since none of the original components of the DSSCs was incorporated into the hybrid halide perovskite device that was based on a mesoporous alumina (Al_2O_3) structure, the creation of this device was an epoch-making step which brought about a new type of solar cell. Due to the use of the mesoporous alumina scaffold acting in its superstructure, upon which the photoactive layer is further structured, this type of perovskite solar device with Al_2O_3 layer has been defined as meso-superstructured solar cells (MSSCs).[52,53]

Since the Al_2O_3 works as an insulating layer in MSSCs, it raises the debate regarding whether the mesostructure is essential in boosting efficiencies, or if the perovskite layer is able to transport the charges within itself.

2.3.4 Planar Heterojunction Perovskite Solar Cells

The first planar heterojunction perovskite solar cells were fabricated via solution processing, and they delivered around 5% efficiency in the absence of

mesostructure.[53] This demonstrates that a perovskite semiconductor is capable of operating in a much simpler planar architecture while remaining competent in its performance in ambipolar charge transport. This device fulfils all the principle roles of photovoltaic operation, i.e. light absorption, generation of electrons and holes, and transport of charge carriers. The use of a positive-intrinsic-negative (*p*-*i*-*n*) heterojunction has improved carrier collection. However, no planar heterojunction perovskite solar cells had achieved high efficiency at the time of this report, and the fabrication of a high quality film capable of achieving optimal thin film configuration, was still highly challenging.

2.3.5 Tandem Solar Cells

The efficiency of single junction solar cells is limited as shown in Figure 2.3 and only photons possessing higher energies than the bandgap of the semiconducting material can be absorbed to generate charges. One of the strategies to further enhance the efficiency of solar cells entails increasing the range of bandgaps to utilise different photon energies. Tandem cells usually refer to two or more sub-cells stacked together to absorb more light across a broader spectrum from the sun, with the primary objective of further improving the power efficiency (Figure 2.7a, b). There are two basic configurations for connecting the sub-cells together in order to create tandem device: serial or parallel connections (Figure 2.7c). In either structure, short wavelength light is preferentially absorbed first in a wide bandgap cell and longer wavelength light is absorbed in a smaller bandgap cell subsequently. The tandem device in parallel requires independent electrical contacts on the top and bottom of each sub-cell which is hard to achieve in practice. On the other hand, constructing the sub-cells in series is more feasible where a single current passes through, and the

voltages across the sub-cells are added (i.e., two terminals).

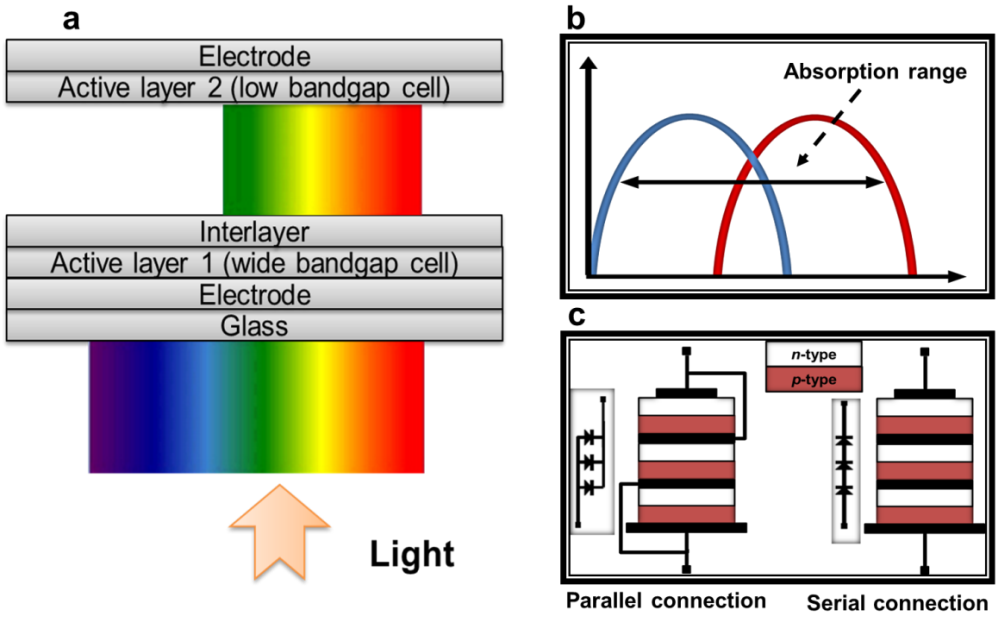


Figure 2.7: Tandem device. (a) Schematic **(b)** Absorption spectra **(c)** Constructions of tandem cells

The balance limit of the performance of tandem devices has been extensively studied by De Vos in 1980.[54] The theoretical maximum PCE was calculated from 33.7% of a single-junction cell to 42% and 49% of tandem devices consisting of two and three optimal sub-cells respectively.[54]

Experimentally, an inorganic tandem device based on InGaP/GaAs/InGaAs has obtained a high conversion efficiency of 37.9±1.2% under AM1.5G,[8] and an organic polymer tandem cell consisting of two sub-cells has just reached a PCE of 10% recently.[55] A prospective interesting application for the perovskite technology is to employ it as the "top cell" in a "hybrid tandem junction" with either c-Si, CIGS or other emerging PV material concepts.[56]

2.4 Operation Mechanisms of Perovskite Solar Cells

Considering that the perovskite-sensitized system is purely analogous to an ssDSSC system, where the absorbed photons are converted into charges by the injection of the electrons and regeneration of holes, a fast injection of carriers from the light absorber, into their respective conductive media (e.g., mesoporous TiO_2) is involved without any carrier transports within the absorber itself. Therefore, as mentioned before, a good distribution of the perovskite absorbers, sensitized on the mesoporous layer to provide sufficient internal surface area will maximise the light absorption. The limitations of this architecture will thus, be similar to that of the classical ssDSSCs which have been widely studied.[12] The first consideration of loss may originate from the light absorption, while the high extinction coefficient of the perovskite material ensures good absorption of the light at relatively low mesoporous film thickness compared to the ssDSSCs system. Secondly, losses could also arise from the charge transportation from excited states to charge transporters due to the energy offsets. In addition to these voltage losses associated with energy level mismatches and charge transportation, charge recombination is another factor that could limit the performance of these devices. Thicker perovskite films increase the light absorption, while simultaneously increasing the possibility of charge carriers' recombination. This results in a reduction of the external quantum efficiency (EQE) and consequently the current.[48,57,58] Therefore, carefully tuning the recombination mechanism and its characterisation is critical for further improving the efficiency of perovskite-sensitized solar cells.

In contrast to the perovskite-sensitized solar cell, the meso-superstructured perovskite device employs the insulating layer of Al_2O_3 as a scaffold instead of the sensitized

TiO_2 layer where the Al_2O_3 scaffold provides roughness to the absorber layer (note that analysis in Chapter 6 proposes that Al_2O_3 scaffold also functions as slightly *n*-doped layer), resulting in efficient light absorption. Hole transportation from the photoexcited perovskite to the hole transport material (HTM) in the MSSCs performs in the same way as compared to the ssDSSCs. However, unlike the sensitized cells where the electrons are transferred into the mesoporous TiO_2 layer, the electrons in the Al_2O_3-based cells remain in the perovskite phase until they are collected at the electrode.[49] A schematic illustration of the operational mechanism of a TiO_2 based perovskite-sensitized and alumina based MSSCs, along with the illustration of charge transport in each system are shown in Figure 2.8.

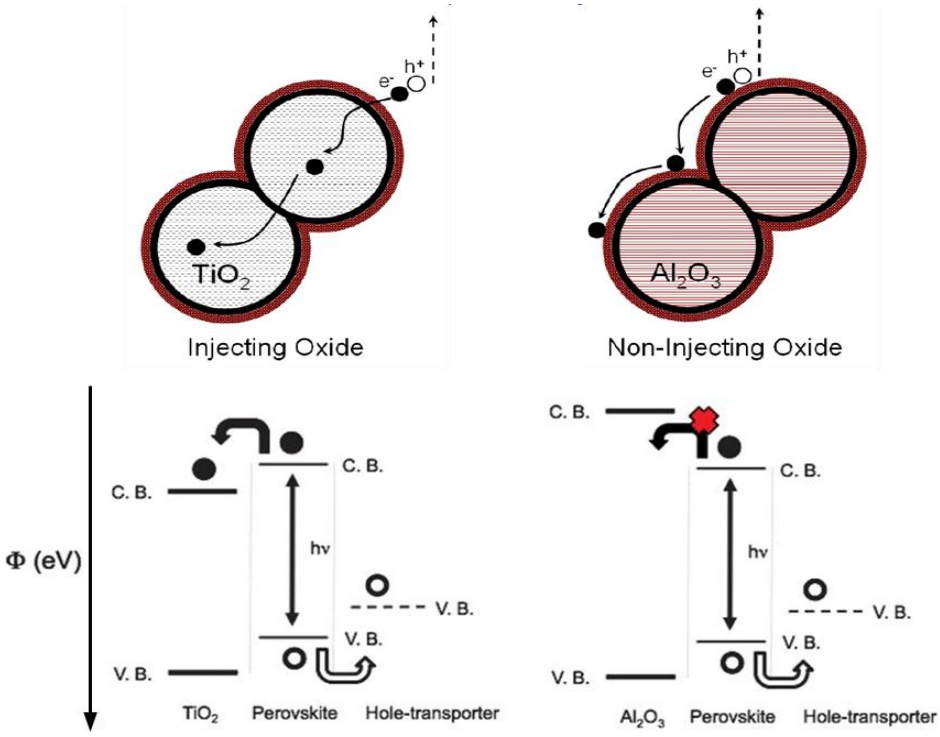


Figure 2.8: Charge transport of perovskite solar cells in mesoporous TiO_2 and mesoporous Al_2O_3 scaffold. This figure is modified from ref.49.

By removing the Al_2O_3 layer completely in a planar heterojunction perovskite device, it confirms that the extracted electrons are able to flow within the perovskite itself.[49,53]

The key physical operation mechanism of the planar heterojunction perovskite device is that the perovskite does not only absorb photons but also transports both electrons and holes, benefiting therefore from its ambipolar conducting nature.[53]

In order to understand the charge mechanism of this planar heterojunction configuration, it is critical to investigate the nature of the first excited state. If the binding energy of the photogenerated electron–hole pair is low enough that is comparable to thermal energy at room temperature, i.e. $k_BT \approx 25.2$ meV at $T = 293$ K, charge generation can take place within the absorber, analogous to thin film silicon solar cells.[59] This could explain the relatively high efficiency of the device, since the voltage drop due to the dissociation of the electron-hole pairs is avoided. Classical studies have suggested that electron-holes pairs in a $CH_3NH_3PbI_3$ perovskite film behave as a Mott-Wannier exciton, with binding energies in the range of 19meV[60] to 50meV[15]. The binding energy of $CH_3NH_3PbI_{3-x}Cl_x$ has been also roughly estimated to be about 55meV.[61] Due to the closeness of these binding energies to the thermal energy, dynamically interchanging populations of both free carriers and excitons have to be considered. To the present day, a consistent picture of the coexistence of the two species is still emerging.

Additionally, Stranks *et al* conducted photoluminescence quenching measurement to understand the transport of holes and electrons from the perovskite film to the hole transport layer (spiro-OMeTAD) or to the electron collector ([6,6]-phenyl-C61-butyric acid methyl ester: PCBM) respectively in order to evaluate the electron-hole diffusion length.[62] The results showed that the carrier diffusion lengths are over 1 μm in mixed-halide perovskite ($CH_3NH_3PbI_{3-x}Cl_x$) film and over 100 nm in triiodide perovskite ($CH_3NH_3PbI_3$) film. Similar results were also confirmed by Xing *et al*.[63]

The low binding energy and long charge carrier diffusion lengths indicate the possibility of charge separation within the absorber itself. It also explains the good performance of perovskite device in a thin film configuration.[59]

However, defects states are common in solid surfaces where intrinsic defects due to interruption of the crystal structure, while extrinsic defects due to absorbed impurity atoms. This tends to introduce other electronic states within the bandgap localised most likely near the interface. These behave as recombination centres and influence the potential distribution at the interface by trapping charge carriers which may not respond to thermal excitation (i.e., deep trapping) thereby rendering them immobile to the detriment of the photocurrent.[1] Therefore, in the thin film perovskite configuration, the bulk recombination within the perovskite gains prominence and the elimination of the energetic defects is necessary for the enhancement of thin film devices. Accurate control of the film morphology and crystallinity is crucial to reduce defect states. Therefore, choosing carefully from various deposition techniques will determine the crystal growth, film formation, and consequently the device performance.

2.5 Fabrication Techniques for Perovskite Films

2.5.1 Spin-Coating

The hybrid organic-inorganic perovskite films can be prepared by spin coating because of its strong self-assembling propensity accompanied with solvent evaporation processes.[13,64] In the laboratory, the spin-coating technique is commonly used due to its low-cost, and convenient simplicity for device fabrication. Studies show that it has been used to prepare various organic-inorganic perovskite films.[2] The process involves dissolving the original precursors (e.g., methylammonium halide

MAX and lead halide PbX_2 for synthesising $MAPbX_3$ halide perovskite), in a polar aprotic solvent. The resulting solution is then spin coated on the substrate at room temperature.

However, it is not easy to find a common effective solvent, due to the solubility level of different precursors. In addition, the films do suffer from poor control of film formation and crystallisation through spin-coating, leading to defect states in the resultant crystal structure. These defects often take the form of vacancies, dislocations, and grain boundaries. As mentioned before, such interface states caused by the defects may result in trap states within the band gap of the semiconductor.

2.5.2 Sequential Two-Step Deposition

The sequential two-step deposition was initially proposed by Mitzi *et al* to prepare the multilayered $(RNH_3)_2$-$(CH_3NH_3)_{n-1}M_nI_{3n+1}$ (n=1, 2,…) and $CH_3NH_3PbI_3$ perovskite films.[65] The inorganic metal halide MI_2 was initially vapour deposited on a substrate. Next, the substrate was dipped into an organic ammonium iodide solution for a short period (1-5 min) depending on the desired thickness. Alternatively, perovskite thin films can be fabricated by firstly depositing a film of organic alkyldiammonium salt on a substrate, followed by dipping it into the metal halide solution.[66] Moreover, a sequential-dipping technique entailing dipping into solutions of organic amine salts and then metal halides in sequence, is also capable of forming perovskite films.[67] Again, it is challenging to find a suitable solvent that effectively dissolves the metal halide, without affecting the organic ammonium salt or other chemicals around.

2.5.3 Vapour Deposition

Vapour deposition is one of the most common fabrication methods in large scale manufacturing. It conventionally refers to depositing a layer via the condensation of a vaporised form of the desired material onto a surface in vacuum. Reports have shown that hybrid organic-inorganic perovskites, such as $(C_6H_5C_2H_4NH_3)_2PbI_4$ and $(C_6H_5C_2H_4NH_3)_2PbBr_4$, have been evaporated through single source thermal deposition (Figure 2.9a).[68] In the single source deposition process, a small amount of solvent containing the organic and inorganic components was placed on a common tantalum heater, then the mixture was evaporated onto a substrate within a very short time (<1s). In addition, dual-source thermal deposition has been proposed as an alternative vapour deposition technique to evaporate the solid-state organic source (RNH_3I) and inorganic source (PbI_2) simultaneously to form a perovskite material ($(RNH_3)_2PbI_4$) (Figure 2.9b).[69]

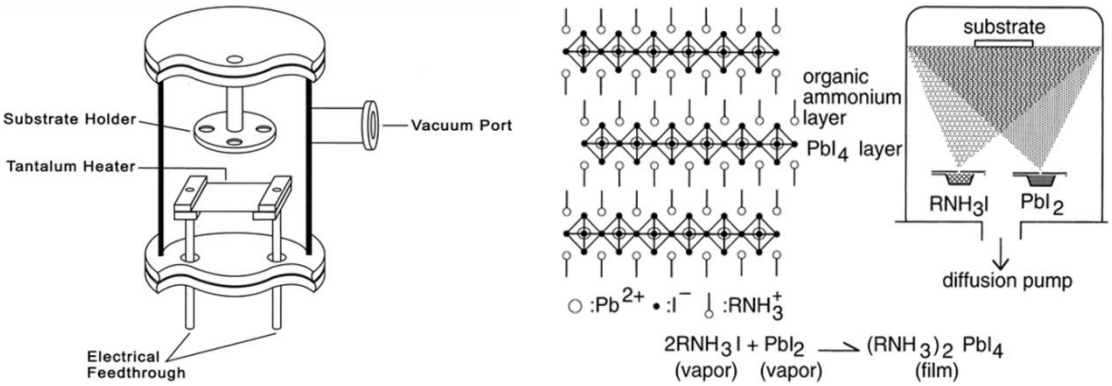


Figure 2.9: Vapour deposition system for perovskite film. (a) single-source vapour deposition system; reprinted from ref.68; **(b)** Dual-source vapour deposition system; reprinted from ref.69

Furthermore, vapour deposition is a straightforward route to constructing multi-junction architectures. It is an established technique for building inorganic multi-junction devices, such as silicon-based, and III-V semiconductor-based

multijunction solar PV devices.[70,71,72] Within recent years, small molecular organic photovoltaics (OPV) fabricated by vapour deposition have also effectively competed with solution-processed OPV for creating tandem devices.[73,74]

2.5.4 Other Deposition Methods

Calcination of perovskites based on the synthesis of constituent elements or their compounds whilst solid at high temperatures (>1000^{o}C) is another conventional way of fabricating inorganic perovskites.[75] However, high temperature circumstances are usually not suitable for processing organic precursors. Other deposition methods for depositing perovskite films have also been properly researched for decades such as pulsed-laser deposition,[76,77] chemical solution deposition,[78,79] etc. However, they are rarely utilised due to their high cost, complexity, and low availability of the required facilities.

Although various hybrid inorganic-organic halide perovskites for light absorbers have been proposed as promising research materials for PV technology, they are still at their infancy, and many challenges have emerged simultaneously. In order to utilise perovskite PV technology for commercial applications, it is essential to enhance power conversion efficiency whilst preserving the feasibility of large scale fabrication. The following work will give an insight into fabrication techniques, especially into vapour deposition, aimed at delivering efficient thin film perovskite solar cells. This work hopes to pave the way for perovskite PV technology in the manufacturing industry.

References

1. Nelson, J. *The Physics of Solar cells*. (Imperial College Press, 2003).

2. Mitzi, D. B. Synthesis,Structure,and Properties of Organic-Inorganic Perovskites and Related Materials. *Prog. Inorg. Chem.* **48,** 1–121 (1999).

3. Mills, A. & Le Hunte, S. An overview of semiconductor photocatalysis. *J. Photochem. Photobiol. A Chem.* **108,** 1–35 (1997).

4. Lorenzo, E. et al. *Solar Electricity: Engineering of Photovoltaic Systems*. 316 (PROGENSA, 1994).

5. National Renewable Energy Laboratory of the U.S. Solar Spectral Irradiance: Air Mass 1.5. at <http://rredc.nrel.gov/solar/spectra/am1.5/>

6. Glunz, S. W. Crystalline Silicon Solar Cells with High Efficiency. in *Adv. Concepts Photovoltaics* (eds. Nozik, A. J., Conibeer, G. & Beard, M. C.) 1–29 (Royal Society of Chemistry, 2014). doi:10.1039/9781849739955

7. Green, M. A. Thin-film solar cells: review of materials, technologies and commercial status. *J. Mater. Sci. Mater. Electron.* **18,** 15–19 (2007).

8. Green, M. A., Emery, K., Hishikawa, Y., Warta, W. & Dunlop, E. D. Solar cell efficiency tables (version 44). *Prog. Photovoltaics Res. Appl.* **22,** 701–710 (2014).

9. Andersson, B. A. Materials availability for large-scale thin-film photovoltaics. *Prog. Photovoltaics Res. Appl.* **8,** 61–76 (2000).

10. He, Z. *et al.* Enhanced power-conversion efficiency in polymer solar cells using an inverted device structure. *Nat. Photonics* **6,** 593–597 (2012).

11. O'Regan, B. & Grätzel, M. A low-cost, high-efficiency solar cell based on dye-sensitized colloidal TiO_2 films. *Nature* **353,** 737 (1991).

12. Snaith, H. J. Estimating the Maximum Attainable Efficiency in Dye-Sensitized Solar Cells. *Adv. Funct. Mater.* **20,** 13–19 (2010).

13. Mitzi, D. B., Feild, C. A., Harrison, W. T. A. & Guloy, A. M. Conducting tin halides with a layered organic-based perovskite structure. *Nature* **369,** 467–469 (1994).

14. Mitzi, D. B. Templating and structural engineering in organic–inorganic perovskites. *J. Chem. Soc. Dalt. Trans.* 1–12 (2001). doi:10.1039/b007070j

15. Tanaka, K. *et al.* Comparative study on the excitons in lead-halide-based perovskite-type crystals $CH_3NH_3PbBr_3$ $CH_3NH_3PbI_3$. *Solid State Commun.* **127,** 619–623 (2003).

16. Gao, P., Grätzel, M. & Nazeeruddin, M. K. Organohalide lead perovskites for photovoltaic applications. *Energy Environ. Sci.* **7,** 2448–2463 (2014).

17. Chang, Y. H. & Park, C. H. First-Principles Study of the Structural and the Electronic Properties of the Lead-Halide-Based Inorganic-Organic Perovskites $(CH_3NH_3)PbX_3$ and $CsPbX_3$ (X=Cl, Br,I). *J. Korean Phys. Soc.* **4,** 889–893 (2004).

18. Borriello, I., Cantele, G. & Ninno, D. Ab initio investigation of hybrid organic-inorganic perovskites based on tin halides. *Phys. Rev. B* **77,** 235214 (2008).

19. Kulkarni, S. A. *et al.* Band-gap tuning of lead halide perovskites using a sequential deposition process. *J. Mater. Chem. A* **2,** 9221 (2014).

20. Noh, J. H., Im, S. H., Heo, J. H., Mandal, T. N. & Seok, S. Il. Chemical Management for Colorful, Efficient, and Stable Inorganic-Organic Hybrid Nanostructured Solar Cells. *Nano Lett.* **13,** 1764–1769 (2013).

21. Green, M. A., Ho-Baillie, A. & Snaith, H. J. The emergence of perovskite solar cells. *Nat. Photonics* **8,** 506–514 (2014).

22. Li, C. *et al.* Formability of ABX_3 (X = F, Cl, Br, I) halide perovskites. *Acta Crystallogr. B.* **64,** 702–7 (2008).

23. Galasso, F. S. *Structure, properties, and preparation of perovskite-type compounds*. 207 (Pergamon Press, 1969).

24. Trots, D. M. & Myagkota, S. V. High-temperature structural evolution of caesium and rubidium triiodoplumbates. *J. Phys. Chem. Solids* **69,** 2520–2526 (2008).

25. MØLLER, C. K. A Phase Transition in Cæsium Plumbochloride. *Nature* **180,** 981–982 (1957).

26. Salau, A. M. Fundamental absorption edge in PbI_2:KI alloys. *Sol. Energy Mater.* **2,** 327–332 (1980).

27. Takahashi, Y. *et al.* Charge-transport in tin-iodide perovskite $CH_3NH_3SnI_3$: origin of high conductivity. *Dalton Trans.* **40,** 5563–8 (2011).

28. Stoumpos, C. C., Malliakas, C. D. & Kanatzidis, M. G. Semiconducting tin and lead iodide perovskites with organic cations: phase transitions, high mobilities, and near-infrared photoluminescent properties. *Inorg. Chem.* **52,** 9019–38 (2013).

29. Kawamura, Y., Mashiyama, H. & Hasebe, K. Structural Study on Cubic–Tetragonal Transition of $CH_3NH_3PbI_3$. *J. Phys. Soc. Japan* **71,** 1694–1697 (2002).

30. Baikie, T. *et al.* Synthesis and crystal chemistry of the hybrid perovskite $(CH_3NH_3)PbI_3$ for solid-state sensitised solar cell applications. *J. Mater. Chem. A* **1,** 5628 (2013).

31. Poglitsch, A. & Weber, D. Dynamic disorder in methylammoniumtrihalogenoplumbates (II) observed by millimeter-wave spectroscopy. *J. Chem. Phys.* **87,** 6373 (1987).

32. Mitzi, D. B. Synthesis, Crystal Structure, and Optical and Thermal Properties of $(C_4H_9NH_3)_2MI_4$ (M = Ge, Sn, Pb). *Chem. Mater.* **8,** 791–800 (1996).

33. Papavassiliou, G. C. & Koutselas, I. B. Structural, optical and related properties of some natural three- and lower-dimensional semiconductor systems. *Synth. Met.* **71,** 1713–1714 (1995).

34. Thiele, G., Rotter, H. W. & Schmidt, K. D. Kristallstrukturen und Phasentransformationen von Caesiumtrihalogenogermanaten(II) $CsGeX_3$ (X = Cl, Br, I). *Zeitschrift fur Anorg. und Allg. Chemie* **545,** 148–156 (1987).

35. Feng, J. Mechanical properties of hybrid organic-inorganic $CH_3NH_3BX_3$ (B = Sn, Pb; X = Br, I) perovskites for solar cell absorbers. *APL Mater.* **2,** 081801 (2014).

36. Huang, L. & Lambrecht, W. R. L. Electronic band structure, phonons, and exciton binding energies of halide perovskites $CsSnCl_3$, $CsSnBr_3$, and $CsSnI_3$. *Phys. Rev. B* **88,** 165203 (2013).

37. Kitazawa, N., Watanabe, Y. & Nakamura, Y. Optical properties of $CH_3NH_3PbX_3$ (X = halogen) and their mixed-halide crystals. *J. Mater. Sci.* **37,** 3585–3587 (2002).

38. Noh, J. H., Im, S. H., Heo, J. H., Mandal, T. N. & Seok, S. Il. Chemical management for colorful, efficient, and stable inorganic-organic hybrid nanostructured solar cells. *Nano Lett.* **13,** 1764–9 (2013).

39. Wang, L. *et al.* Composition-dependent photoluminescence intensity and prolonged recombination lifetime of perovskite $CH_3NH_3PbBr_{3-x}Cl_x$ films. *Chem. Commun.* (2014). doi:10.1039/C4CC04973J

40. Colella, S. *et al.* $MAPbI_{3-x}Cl_x$ Mixed Halide Perovskite for Hybrid Solar Cells: The Role of Chloride as Dopant on the Transport and Structural Properties. *Chem. Mater.* **25,** 4613–4618 (2013).

41. Mosconi, E., Amat, A., Nazeeruddin, M. K., Grätzel, M. & De Angelis, F. First-Principles Modeling of Mixed Halide Organometal Perovskites for Photovoltaic Applications. *J. Phys. Chem. C* **117,** 13902–13913 (2013).

42. Kagan, C. R. Organic-Inorganic Hybrid Materials as Semiconducting Channels in Thin-Film Field-Effect Transistors. *Science.* **286,** 945–947 (1999).

43. Tanaka, K. *et al.* Electronic and Excitonic Structures of Inorganic–Organic Perovskite-Type Quantum-Well Crystal $(C_4H_9NH_3)_2PbBr_4$. *Jpn. J. Appl. Phys.* **44,** 5923–5932 (2005).

44. Bach, U. *et al.* Solid-state dye-sensitized mesoporous TiO_2 solar cells with high photon-to-electron conversion efficiencies. **395,** 583–585 (1998).

45. Kojima, A., Teshima, K., Miyasaka, T. & Shirai, Y. Novel Photoelectrochemical Cell with Mesoscopic Electrodes Sensitized by Lead-Halide Compounds (2). in *210th ESC Meet.* 397 (The Electrochemical Society, 2006). at <http://ma.ecsdl.org/content/MA2006-02/7/397.abstract>

46. Kojima, A., Teshima, K., Shirai, Y. & Miyasaka, T. Organometal halide perovskites as visible-light sensitizers for photovoltaic cells. *J. Am. Chem. Soc.* **131,** 6050–6051 (2009).

47. Im, J.-H., Lee, C.-R., Lee, J.-W., Park, S.-W. & Park, N.-G. 6.5% Efficient Perovskite Quantum-Dot-Sensitized Solar Cell. *Nanoscale* **3,** 4088–93 (2011).

48. Kim, H.-S. *et al.* Lead iodide perovskite sensitized all-solid-state submicron thin film mesoscopic solar cell with efficiency exceeding 9%. *Sci. Rep.* **2,** 591 (2012).

49. Lee, M. M., Teuscher, J., Miyasaka, T., Murakami, T. N. & Snaith, H. J. Efficient hybrid solar cells based on meso-superstructured organometal halide perovskites. *Science* **338,** 643–7 (2012).

50. Burschka, J. *et al.* Tris(2-(1H-pyrazol-1-yl)pyridine)cobalt(III) as p-type dopant for organic semiconductors and its application in highly efficient solid-state dye-sensitized solar cells. *J. Am. Chem. Soc.* **133,** 18042–5 (2011).

51. Snaith, H. J. & Schmidt-Mende, L. Advances in Liquid-Electrolyte and Solid-State Dye-Sensitized Solar Cells. *Adv. Mater.* **19,** 3187–3200 (2007).

52. Lee, M. M., Teuscher, J., Miyasaka, T., Murakami, T. N. & Snaith, H. J. Efficient Hybrid Solar Cells Based on Meso-Superstructured Organometal Halide Perovskites. *Science* **338,** 643–647 (2012).

53. Ball, J. M., Lee, M. M., Hey, A. & Snaith, H. J. Low-temperature processed meso-superstructured to thin-film perovskite solar cells. *Energy Environ. Sci.* **6,** 1739–1743 (2013).

54. Vos, A. De. Detailed balance limit of the efficiency of tandem solar cells. *J. Phys. D. Appl. Phys.* **13,** 839–846 (1980).

55. You, J. *et al.* 10.2% power conversion efficiency polymer tandem solar cells consisting of two identical sub-cells. *Adv. Mater.* **25,** 3973–8 (2013).

56. Beiley, Z. M. & McGehee, M. D. Modeling low cost hybrid tandem photovoltaics with the potential for efficiencies exceeding 20%. *Energy Environ. Sci.* **5,** 9173 (2012).

57. Heo, J. H. *et al.* Efficient inorganic-organic hybrid heterojunction solar cells containing perovskite compound and polymeric hole conductors. *Nat. Photonics* 1–6 (2013). doi:10.1038/NPHOTON.2013.80

58. Zhao, Y. & Zhu, K. Charge Transport and Recombination in Perovskite $(CH_3NH_3)PbI_3$ Sensitized TiO_2 Solar Cells. *J. Phys. Chem. Lett.* **4,** 2880–2884 (2013).

59. Shah, a. V. *et al.* Thin-film silicon solar cell technology. *Prog. Photovoltaics Res. Appl.* **12,** 113–142 (2004).

60. Sun, S. *et al.* The origin of high efficiency in low-temperature solution-processable bilayer organometal halide hybrid solar cells. *Energy Environ. Sci.* **7,** 399 (2014).

61. D'Innocenzo, V. *et al.* Excitons versus free charges in organo-lead tri-halide perovskites. *Nat. Commun.* **5,** 3586 (2014).

62. Stranks, S. D. *et al.* Electron-hole diffusion lengths exceeding 1 micrometer in an organometal trihalide perovskite absorber. *Science* **342,** 341–4 (2013).

63. Xing, G. *et al.* Long-range balanced electron- and hole-transport lengths in organic-inorganic $CH_3NH_3PbI_3$. *Science* **342,** 344–7 (2013).

64. Xu, C. *et al.* Magneto-optical effects of excitons in $(C_{10}H_{21}NH_3)_2PbI_4$ under high magnetic fields up to 40 T. *Solid State Commun.* **79,** 249–253 (1991).

65. Liang, K., Mitzi, D. B. & Prikas, M. T. Synthesis and Characterization of Organic-Inorganic Perovskite Thin Films Prepared Using a Versatile Two-Step Dipping Technique. *Chem. Mater.* 403–411 (1997).

66. Takeoka, Y. *et al.* Intercalated formation of two-dimensional and multi-layered perovskites in organic thin films. *Chem. Commun. (Camb).* 378–80 (2005). doi:10.1039/b413398f

67. Matsui, T., Yamaguchi, A., Takeoka, Y., Rikukawa, M. & Sanui, K. Fabrication of two-dimensional layered perovskite $[NH_3(CH_2)_{12}NH_3]PbX_4$ thin films using a self-assembly method. *Chem. Commun. (Camb).* **3,** 1094–5 (2002).

68. Mitzi, D. B., Prikas, M. T. & Chondroudis, K. Thin Film Deposition of Organic-Inorganic Hybrid Materials Using a Single Source Thermal Ablation Technique. *Chem. Mater.* **11,** 542–544 (1999).

69. Era, M. & Hattori, T. Self-Organized Growth of PbI-Based Layered Perovskite Quantum Well by Dual-Source Vapor Deposition. *Chem. Mater.* **9(1),** 8–10 (1997).

70. Sugo, M., Takanashi, Y., Al-jassim, M. M. & Yamaguchi, M. Heteroepitaxial growth and characterization of InP on Si substrates. *J. Appl. Phys.* **68,** 540 (1990).

71. Dupuis, R. D. III-V semiconductor heterojunction devices grown by metalorganic chemical vapor deposition. *IEEE J. Sel. Top. Quantum Electron.* **6,** 1040–1050 (2000).

72. King, R. R. *et al.* 40% efficient metamorphic GaInP⁄GaInAs⁄Ge multijunction solar cells. *Appl. Phys. Lett.* **90,** 183516 (2007).

73. Riede, M. *et al.* Efficient Organic Tandem Solar Cells based on Small Molecules. *Adv. Funct. Mater.* **21,** 3019–3028 (2011).

74. New, E., Howells, T., Sullivan, P. & Jones, T. S. Small molecule tandem organic photovoltaic cells incorporating an α-NPD optical spacer layer. *Org. Electron.* **14,** 2353–2359 (2013).

75. Xu, X., Randorn, C., Efstathiou, P. & Irvine, J. T. S. A red metallic oxide photocatalyst. *Nat. Mater.* **11,** 595–8 (2012).

76. Tabata, H., Tanaka, H. & Kawai, T. Formation of artificial $BaTiO_3/SrTiO_3$ superlattices using pulsed laser deposition and their dielectric properties. *Appl. Phys. Lett.* **65,** 1970 (1994).

77. Yun, K. Y., Noda, M. & Okuyama, M. Prominent ferroelectricity of $BiFeO_3$ thin films prepared by pulsed-laser deposition. *Appl. Phys. Lett.* **83,** 3981 (2003).

78. Schwartz, R. W. Chemical Solution Deposition of Perovskite Thin Films. *Chem. Mater.* **9(11),** 2325–2340 (1997).

79. Singh, S. K., Ishiwara, H. & Maruyama, K. Room temperature ferroelectric properties of Mn-substituted $BiFeO_3$ thin films deposited on Pt electrodes using chemical solution deposition. *Appl. Phys. Lett.* **88,** 262908 (2006).

Chapter 3

Methodology

Previous chapters have introduced the current issues in the research field of perovskite solar cells. This chapter is firstly going to present the synthesis methods of precursors followed by the fabrication processes of perovskite solar cells with different configurations. Subsequently, the techniques selected to characterise the devices are introduced.

3.1 Synthesis of Precursors

This section introduces the synthesis process of methylammonium (MA) halide (CH_3NH_3X) and lead halide (PbX_2) that are fundamental precursors either by vapour deposition or solution processing for forming halide perovskite films. The synthesis process of halide perovskite ($MAPbX_3$) precursor prepared for solution processing is then presented.

3.1.1 Synthesis of Methylammonium Iodide (CH_3NH_3I)

To syntheses methylammonium iodide (MAI), methylamine (CH_3NH_2) solution (33 wt% in absolute ethanol) was very slowly reacted with hydroiodic acid (HI) (57 wt % in water) in ethanol at room temperature with continuous stirring for 30 min. Typical quantities were 24 mL methylamine, 10 mL hydroiodic acid and 100 mL ethanol. The prepared solution subsequently was dried on a hot plate at 100^{o}C for 4h to crystallise MAI. Formation of a white coloured powder indicated successful crystallisation.[1]

3.1.2 Synthesis of Methylammonium Bromide (CH_3NH_3Br)

Similarly, methylamine (40% in methanol) was slowly reacted with hydrobromide acid (48% in water, Aldrich) in a 1:1 molar ratio with continuous stirring at room temperature for 2h. The product was crystallised by drying at 100 °C for 4 h in air.[2]

3.1.3 Purchase of Metal Halide

Lead halide PX_2 (i.e., lead iodide PbI_2, lead chloride $PbCl_2$, and lead bromide $PbBr_2$) were purchased from Sigma-Aldrich.

3.1.4 Synthesis of Hybrid Halide Perovskites

The synthesis of hybrid organic-inorganic halide perovskite $MAPbX_3$ (where X= I, Br or $I_{3-x}Cl_x$) for single solvent spin-coating was followed the recipe as below:

- $MAPbI_3$ perovskite solution was prepared by dissolving MAI and PbI_2 in 1:1 molar ratio in dimethylformanide (DMF) at 0.88 M. Typically, 560 mg MAI and 1622 mg PbI_2 were dissolved in 4 mL DMF in sequence.[3]

- $MAPbBr_3$ perovskite solution was prepared by dissolving MABr and $PbBr_2$ in 1:1

molar ratio in DMF at 0.88 M. Usually, 394 mg MABr and 1292 mg $PbBr_2$ were dissolved in 4 mL DMF subsequently.[2]

- $MAPbI_{3-x}Cl_x$ perovskite solution (known as mixed-halide perovskite throughout this thesis) was prepared by dissolving MAI and $PbCl_2$ in 3:1 molar ratio in DMF at 40 wt%.[1]

3.2 Device Assembly

Perovskite solar cells discussed in this thesis employ two configurations, meso-superstructure and planar heterojunction. Solution processing via spin-coating has been demonstrated elsewhere to fabricate both meso-superstructured perovskite solar cells and planar heterojunction perovskite solar cells,[1,4] while vapour deposition will be investigated in the following chapters to fabricate efficient planar heterojunction perovskite solar cells. This section introduces the procedures for fabricating meso-superstructured and planar heterojunction perovskite solar cells via solution processing and vapour deposition respectively.

3.2.1 FTO Glass Preparation

The procedures of substrate preparation has been presented elsewhere[1,4] and it was undertaken in ambient conditions. Briefly, Fluorine-doped tin oxide (FTO) glass (TEC7, 7 Ω/□ sheet resistivity) was etched by using Zn metal powder and 2M HCl. Following the removal of the FTO in the required areas, the patterned substrate was cleaned with Hellmanex™ cuvette detergent (2% in de-ionised water). Subsequently the substrate was rinsed with de-ionised water, acetone and ethanol in turn, and dried with clean dry air at the end. Oxygen plasma treatment was used to treat the substrate for 10 min.

3.2.2 Fabrication of Meso-superstructured Perovskite Device

3.2.2.1 Solution Processing

Process in air: After cleaning the FTO-coated substrate, an acidic solution of titanium isopropoxide (diluted in ethanol) was deposited on top by spin-coating at 2,000 r.p.m for 1 min, followed by drying at 150^{o}C for 10 min to drive out the solvent (e.g., ethanol and water) and then sintering at 500°C for 30 min to form a *n*-type electron-selective compact layer of titania (TiO_2).[4] To fabricate the meso-superstructured devices, a mesoporous Al_2O_3 scaffold layer was then spin-coated (speed 2,500 r.p.m, ramp 2,500 r.p.m.s^{-1}, 60s) by using a colloidal dispersion of alumina (Al_2O_3) nanoparticles (<50 nm particles purchased from Sigma-Aldrich) in isopropanol (1:2 by volume). The substrate was immediately dried at 150^{o}C for 30 min mainly to drive out the solvent, giving approximately 400 nm mesoporous scaffold.[4] The perovskite precursor as described in section 3.1.4 was spin-coated (speed 2,000 r.p.m., ramp 2,000 r.p.m.s^{-1}, 45s) on top of the mesoporous layer and heated at 100^{o}C for 45 min in an oven in air.

Process in nitrogen-filled glovebox: To avoid the influence of the moisture while film formation, the perovskite precursor was spin-coated in the glovebox (speed 2,000 r.p.m., ramp 2,000 r.p.m.s^{-1}, 45s) on top of the mesoporous Al_2O_3 and heated at 100^{o}C for 2 h.[5] Note that the fabrication of compact layer of TiO_2 and the mesoporous Al_2O_3 scaffold was undertaken in air as described before.

3.2.3 Fabrication of Planar Heterojunction Perovskite Device

3.2.3.1 Solution Processing

Process in air: The procedures for fabricating planar heterojunction perovskite devices was similar with the meso-superstructured perovskite as stated in section 3.2.2, but without depositing the mesoporous Al_2O_3 scaffold. The *n*-type compact layer TiO_2 was fabricated in the same way as described in section 3.2.2. The perovskite precursor solution prepared as the description in section 3.1.4 was directly spin-coated on top of the compact TiO_2 layer (speed 2,000 r.p.m., ramp 2,000 r.p.m.s^{-1}, 45s). The substrate was then immediately placed in an oven ($MAPbI_{3-x}Cl_x$ for 45 min at 100^oC; $MAPbI_3$ and $MAPbBr_3$ for 10 min at 150^oC).

Process in nitrogen-filled glovebox: High humidity in ambient condition (≥50%) may lead to the widespread pin holes in the perovskite film, mainly due to the highly hygroscopic nature of the perovskite precursor solution. The influence of humidity was predominant to the performance of the planar heterojunction devices via spin-coating where no Al_2O_3 mesostructure was involved. To avoid the influence of the moisture while film formation, the perovskite precursor was spin-coated in a glovebox (MBraun) (speed 2,000 r.p.m., ramp 2,000 r.p.m.s^{-1}, 45s) on top of the *n*-compact TiO_2 layer.[5] Note that the glovebox always was filled with nitrogen that contains a moisture level of <0.1 ppm and an oxygen level of 150 ppm. The perovskite film was then annealed on a hotplate at 90^oC for 2 h for $MAPbI_{3-x}Cl_x$ and $MAPbI_3$ for 30 min at 150^oC respectively. The fabrication of the compact layer of TiO_2 was undertaken in air as described before.

3.2.3.2 Vapour Deposition

3.2.3.2.1 System Description

The evaporated perovskite film was deposited through a vapour evaporation system (Kurt J. Lesker Mini Spectros) integrated into a nitrogen-filled glovebox (MBraun) as shown in Figure 3.1. The specifications of the deposition system are as follows[6]:

- Vacuum level able down to 5×10^{-7}mbar using a dry scroll pump and turbo drag pump;
- 2x Metal Joule affect Evaporation Sources.
- 2x Organic light emitting diode (OLED) sources with ceramic crucibles heating up to 400^{o}C, which were used to thermally heat the precursor salts: inorganic source (i.e., PbI_2 or $PbCl_2$) and organic source (MAI). The OLED sources were integrated with thermocouples to allow closed-loop temperature control.
- 2x Film thickness quartz crystal monitors above the OLED sources to control individual deposition rate and thickness of each OLED source; the third quartz crystal monitor at substrate holder level to monitor the total thickness.
- 4''x4'' substrate size, compatible with up to 100 mm x 100 mm square or Φ150mm round substrates, with a rotating platform to ensure the uniformity of the deposited film.
- Water-cooled stainless steel chamber with MBraun glovebox interface flange.

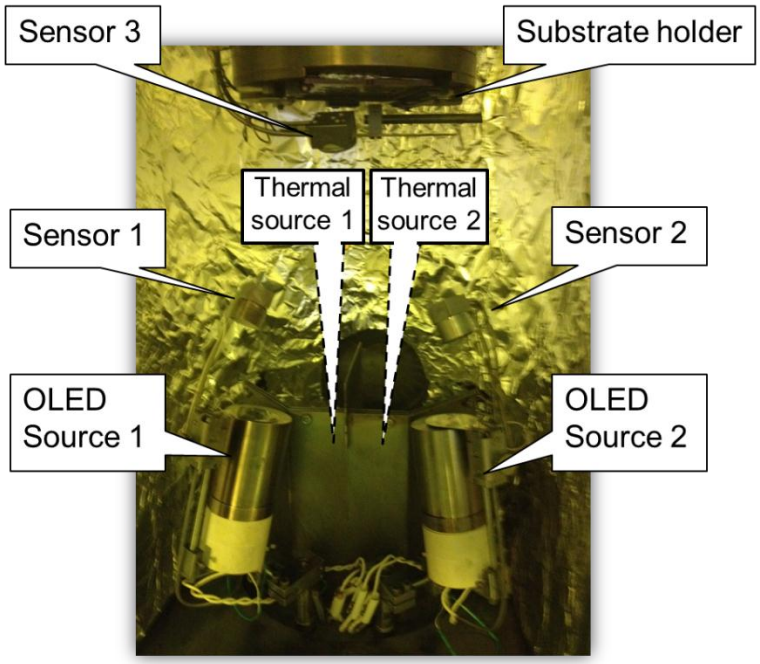


Figure 3.1: Illustration of Kurt J. Lesker Mini Spectros evaporation chamber.

3.2.3.2.2 Fabrication of Perovskite Films via Vapour Deposition

In this work, MAI and lead halide (i.e., PbI_2 and $PbCl_2$) were used as the precursors to fabricate the hybrid inorganic-organic halide perovskite films in the evaporation system. The combination of MAI and $PbCl_2$ was aimed to produce mixed-halide perovskite $MAPbI_{3-x}Cl_x$ films and the combination of MAI and PbI_2 was used to fabricate triiodide perovskite $MAPbI_3$ films. Two vapour deposition techniques, dual-source vapour deposition (DSVD) and two-layer sequential vapour deposition (SVD), were studied in this work to fabricate perovskite films.

Tooling factor estimation: A quartz crystal monitor was positioned a short distance from each vapour-deposition OLED source (as shown in Figure 3.1) and a tooling factor (a ratio of the material deposited on the sensors to that on the substrate) was estimated for each OLED source individually. The acoustic impedance and density of the MAI were both unknown, so both are set to be 1 (this density value 1 g/cm^3 of

MAI is probably close, since the density of MACl has been reported as 1.1g/cm^3 (see ref.7 and ref.8); any possibly absolute difference was taken into account by using the tooling factor). To build an initial appreciation of the temperature and its relation to deposition rates for each material, firstly the deposition rate was recorded while the temperature of each source was ramping up in turn. Then a suitable temperature range with a fixed deposition rate, which would give a reasonable thickness, for each material was selected over a deposition period of 30 min. In other words, a deposition of each source for a total time of approximately 30 min at a constant deposition rate was carried out and the actual deposited thickness of each material on the substrate was then measured with a surface profileometer. The tooling factor of each source was calculated by dividing the thickness reading on the sensor by the actual thickness.

The tooling results are stated in the following chapters corresponding to different batches of evaporation and subsequently applied into the deposition for fabricating perovskite layers.

Perovskite films fabricated by vapour deposition: organic and inorganic precursors were placed into the OLED crucibles separately. The device substrate was loaded in a substrate holder and the TiO_2/FTO (i.e., material side) was faced down towards the OLED sources. In order to ensure homogeneous coated film, the substrate holder was rotated while depositing, since the right-hand OLED source mainly deposits the right-hand side of the substrate and vice versa for the left as shown in Figure 3.1. For the dual-source vapour deposition processing, the inorganic and organic OLED sources were evaporated simultaneously while in the processing of two-layer sequential vapour deposition, the inorganic precursor (i.e., lead halide) was deposited first and subsequently the organic precursor (i.e., MAI) was deposited under high

vacuum (approximately below 10^{-5} mbar). The best device performance was optimised by varying key deposition parameters such as deposition rate and deposition time of the two sources. The optimal deposition parameters for each batch of evaporation are stated in the following chapters correspondingly.

After evaporation, the post-annealing conditions were critical to fully crystallise the perovskite films. The annealing temperature and dwell time closely correlated to the crystallisation and hence device performance.

3.2.4 Hole-Transporter Deposition and Electrode Deposition

To form a *p*-type hole-transport layer, 25 μL of hole transporting solution in chlorobenzene, that contained 61.4 mM spiro-OMeTAD with the additives of tert-butylpyridine (tBP) (55 mM) and lithium bis(trifluoromethylsyfonyl)imide salt (Li-TFSI) (26 mM), was spin-coated (2,000 r.p.m., ramp 2,000 r.p.m.s^{-1}, 45s) on top of the fully crystallised perovskite film. Before deposition the top metal electrode, the samples were left in a desiccator in dark overnight, mainly to expose the device to oxygen while avoiding exposure to humidity. The oxygen exposure improves the performance of these devices by increasing the conductivity of the HTM (Spiro-OMeTAD).[9] 120 nm of a top metal electrode of silver metal was then deposited to complete the device fabrication. Note that spin-coating the hole transporting layer was processed in the nitrogen-filled glovebox.

3.3 Characterisation Techniques

Four characterisation techniques were applied in this work to study the film properties and device performance including crystallography, microstructure, photo-physics, and solar cells performance.

3.3.1 Crystallographic Analysis

3.3.1.1 X-ray Diffraction

Samples preparation: The perovskite film was deposited on glass. To protect the samples from moisture, a thin layer of polymethyl methacrylate (PMMA) (10 mg/mL in chlorobenzene) was coated on the top of the film to prevent exposure from humidity in ambient condition. Two important considerations for sample preparation should be noticed that the sample must be as flat and at a constant height to fulfil diffraction conditions. Otherwise, the peaks would be shifted from their proper positions.

System description: This technique uses the Bragg-condition of X-ray to determine the spacing between parallel planes of atoms in a crystal. From these inter-planar distances a crystal structure can be deduced. The X-ray diffractometer (Panalytical X'Pert Pro) employs a vertical goniometer (theta-theta) with maximum usable range of (depending on accessories) $-40^{o}<2\theta<220^{o}$. The 2θ position of the X-ray diffraction patterns was usually set from 5^{o} to 65^{o} with a step size of 0.0167^{o} and 360.045s per step. Where different settings were used they will be stated specifically in this thesis.

3.3.2 Microstructural Analysis

3.3.2.1 Scanning Electron Microscopy (SEM)

Sample preparation: To increase the sample's conductivity, samples were always coated with platinum (Pt) for a few nanometres to tens of nanometres depending on the requirement, making sure to get a better contrast but not to hide the microstructural information on the film. Moreover, since samples with low

conductivity may lead to image distortion or drift, low acceleration voltage should be applied to reduce the charge effect if samples cannot be coated with a conductive coating.

System description: **A** field emission scanning electron microscope (Hitachi S-4300 field) that uses an electron beam accelerated at 0.5 kV to 30 kV enabling operation at a fixed filament current of 10 μA was used for collecting the SEM images.

3.3.2.2 Atomic Force Microscopy (AFM)

Samples preparation: The atomic force microscopy (AFM) images were obtained from the perovskite film deposited on the TiO_2/FTO-coated glass.

System description: ThermoMicroscope M5 was used to collect the atomic force microscopy (AFM) images by using a non-contact mode and scanning over a range of 20 μm by 20 μm at a resolution of 256 x 256 data points. The surface roughness was measured as the root mean squared roughness over the scanning area.

3.3.3 Photo-physical Analysis

3.3.3.1 Absorption Measurement

The absorption spectra of perovskite films on glass were measured (reference to glass) on a Carry 300 Bio (Agilent Technologies). To reduce the sample variance, at least 3 samples were determined for each group and the average of all spectra presented.

3.3.3.2 Photoluminescence

Sample preparation: all perovskite films were deposited on glass via either solution processing or vapour deposition. The samples were sealed with a 100 nm layer of the inert PMMA (10 mg/mL PMMA in chlorobenzene spin-coated at 1000 r.p.m for 45s)

to prevent from exposing to moisture. The PMMA layer was spin-coated in a nitrogen filled glovebox and then the samples were transferred to a desiccator filled with dry air where they were stored until being measured.[10]

3.3.3.2.1 Steady-State Photoluminescence

System description: Time-correlated single photon counting (TCSPC) setup (FluoTime 300, PicoQuant GmbH) in time integrating mode was used to collect the steady-state PL measurement. Samples were photo-excited via using a Xeon lamp. Hybrid photomultiplier detector assembly (PMA Hybrid 40, PicoQuant GmbH) and a high resolution monochromator were used to collect the PL.

3.3.3.2.2 Time-resolved Photoluminescence

System description: Time-resolved Photoluminescence experiments were also performed on a PicoQuant FluoTime 300 fluorescence spectrometer by means of TCSPC. The samples were photo-excited using a 507 nm laser head (LDH-P-C-510, PicoQuant GmbH) at repetition rate between 1 MHz-10 MHz with pulse duration of 4 ps or 16 ps and a fluence of ~0.13 $\mu J/cm^2$. PL was collected through a lens and then detected at perpendicular polarisation direction associated with the excitation light. In order to keep the counting rate below 1% of the repetition rate and to avoid multi-photon phenomena, an adjustable attenuator in the emission path was utilised in the system. τ_e was defined as the time taken after excitation for the PL intensity to drop to 1/e of its peak intensity.

3.3.3.3 Fourier Transform Photocurrent Spectroscopy (FTPS)

FTPS is a spectroscopic method where a detector is replaced by the measured device itself to generate photocurrent and a monochromator is replaced by Fourier Transform

Infrared spectrophotometer (FTIR).[11,12] The benefit in such measurement is that the single wavelength of light is not isolated but the light is encoded in full spectra so that all wavelengths shine on the sample simultaneously. Therefore, the photocurrent on the full spectrum can be mathematically decoded to yield spectral distribution of photocurrent by using fast Fourier transform (FFT) algorithm which is a build-in function in the FTIR setup.

The FTPS system was calibrated with a National Renewables Energy Laboratory (NREL) KG5-filtered Si reference cell (the rated error in the short-circuit photocurrent on this Si reference cell is 1.36% to 95% certainly) and the incident photon-to-current efficiency (IPCE or known as EQE) of perovskite devices was obtained by using[13],

$$\mathrm{EQE}_{measured}\,(\lambda) = \frac{J_{sc-measured}\,(\lambda)}{J_{sc-reference}\,(\lambda)}\,\mathrm{EQE}_{reference}\,(\lambda)$$

where $J_{sc\text{-}reference}$ and $EQE_{reference}$ were known and provided by NREL and $J_{sc\text{-}measured}$ was measured by the FTPS setup. More information of the experimental design of the FTPS measurement is stated in section 6.2.5 and its corresponding results are discussed in sections 6.3.5 in Chapter 6.

Sample preparation: the devices for the FTPS measurement were completed devices as described in 3.2. All the devices were tested by the solar simulator in order to evaluate the device performance prior to measuring the FTIR spectra.

System description: The VERTEX 80v vacuum FT-IR spectrometer is built on the aligned UltraScan™ interferometer and also it has an evacuated optics bench to reduce atmospheric moisture absorptions and to improve the sensitivity and stability

of the experiment. All the samples were under vacuum while measuring.

3.3.4 Solar Cell Performance Characterisation

Current-voltage (*JV*) characteristics were measured (using 2400 Series SourceMeter, Keithley Instruments) based STC under simulated AM 1.5 sunlight, generated by an Abet Class AAB Sun 2000 simulator. The intensity of the simulator was also calibrated with the NREL KG5-filtered Si reference cell as used in the FTPS measurement. The mismatch factor was measured to be less than 1%. In addition, an active area about 0.0625 cm^{-2} of the solar devices was defined by using a mask with a metal aperture, and the solar devices were measured in a light-tight sample holder to minimise any edge effect. Note that both the reference and test cells have to be in the same spot within the solar simulator while measuring.

References

1. Lee, M. M., Teuscher, J., Miyasaka, T., Murakami, T. N. & Snaith, H. J. Efficient hybrid solar cells based on meso-superstructured organometal halide perovskites. *Science* **338,** 643–7 (2012).

2. Noh, J. H., Im, S. H., Heo, J. H., Mandal, T. N. & Seok, S. Il. Chemical management for colorful, efficient, and stable inorganic-organic hybrid nanostructured solar cells. *Nano Lett.* **13,** 1764–9 (2013).

3. Kim, H.-S. *et al.* Lead iodide perovskite sensitized all-solid-state submicron thin film mesoscopic solar cell with efficiency exceeding 9%. *Sci. Rep.* **2,** 591 (2012).

4. Ball, J. M., Lee, M. M., Hey, A. & Snaith, H. J. Low-temperature processed meso-superstructured to thin-film perovskite solar cells. *Energy Environ. Sci.* **6,** 1739–1743 (2013).

5. Eperon, G. E., Burlakov, V. M., Docampo, P., Goriely, A. & Snaith, H. J. Morphological Control for high performance, Solution-processed Planar Heterojunction Perovskite Solar Cells. *Adv. Funct. Mater.* **24,** 151–157 (2014).

6. Kurt J. Lesker Company. at <http://www.lesker.com/newweb/vacuum_systems/deposition_systems_pvd_mini_spectros.cfm>

7. Scharlab. Technical Data Sheet (ME0355). (2006). at <http://www.scharlab.com/>

8. Merck KGaA. 806020 Methylammonium chloride for synthesis. (2013). at <http://www.kimyaevi.org/d01/806020.pdf>

9. Abate, A. *et al.* Lithium salts as “redox active” p-type dopants for organic semiconductors and their impact in solid-state dye-sensitized solar cells. *Phys. Chem. Chem. Phys.* **15,** 2572–9 (2013).

10. Stranks, S. D. *et al.* Electron-hole diffusion lengths exceeding 1 micrometer in an organometal trihalide perovskite absorber. *Science* **342,** 341–4 (2013).

11. Vanecek, M. & Poruba, A. Fourier-transform photocurrent spectroscopy of microcrystalline silicon for solar cells. *Appl. Phys. Lett.* **80,** 719 (2002).

12. Goris, L. *et al.* Observation of the subgap optical absorption in polymer-fullerene blend solar cells. *Appl. Phys. Lett.* **88,** 052113 (2006).

13. Hod’áková, L., Poruba, A., Kravets, R. & Vaněček, M. Fast quantum efficiency measurement of solar cells by Fourier transform photocurrent spectroscopy. *J. Non. Cryst. Solids* **352,** 1221–1224 (2006).

Chapter 4

Efficient Planar Heterojunction Perovskite Solar Cells by Dual-Source Vapour Deposition

Content and Summary

A plethora of different PV technologies are being developed for large scale solar energy conversion.[1,2,3,4] Beyond first generation wafer-based PVs[1] exist a second generation of thin-film concepts which are based on solid semiconductor absorber layers, sandwiched between two charge selective contacts[3] and an emerging generation of meso or nanostructured solar cells that rely on a distributed heterojunction for the generation of charges, and the subsequent transportation of positive (*p*) and negative (*n*) charges in spatially separated phases.[4,5,6] Although a variety of materials have led to the improvement of nanostructured devices, very little progress has been made in recent years on the synthesis of highly efficient thin-film solar cells.[7] Within the past couple of years, however, hybrid organic-inorganic perovskites have shown great promise in nano or mesostructured devices.[8,9,10,11]

In this chapter, a *p-i-n* planar heterojunction perovskite solar cell with solar to electrical PCE values exceeding 15%, as measured under simulated full sunlight, is achieved by dual-source vapour deposition (DSVD). This is a strong indication that perovskite absorbers possess the ability to function at high efficiencies in simplified device architectures, without the need for complex nanostructures. Since vapour deposition technique can be readily integrated with current manufacturing practices, this work is expected to shorten the timeline towards large-scale manufacturing of perovskite solar cells.

4.1 Introduction

Solar to electrical energy conversion via PV devices emerged as one of the most promising renewable energy sources over half a century ago and the PV industry still continues to experience steady growth. First generation PV solar cells that are based on crystalline silicon (c-Si),[12] have consistently led to a reduction in manufacturing costs hence, the price of Si-PV is now approaching grid parity in some locations.[1] However, this cost reduction is likely to plateau because of the large embodied energy in c-Si ingots.[13]

The second generation of solar cells are based on thin-films of silicon or compound semiconductors, which in principle, result in much lower manufacturing costs.[3] Nonetheless, the large-scale production of complex ternary compounds such as CIGS have proven to be challenging for a number of reasons - these include the specific defect chemistry, high sintering temperatures, and the rarity of required raw chemical elements.[13] Regarding the latter, Te and In which are relatively scarce constitute two of the best performing thin film devices. Thus, the innovation of solar cells utilising cheap and abundant materials, is required for a sustainable terra watt (TW) PV industry capable of serving as a major global energy source.[14]

A solar cell consists of different components which perform discrete roles, with different tolerance levels for impurities and other optoelectronic properties. The concept of the hybrid inorganic-organic solar cell is “material agnostic”, aiming to optimise each material for its corresponding individual function. Numerous hybrid solar cells have been studied in π-conjugated polymer blends containing semiconductors such as CdSe[15], $CuInS_2$[16] and PbS[17]. Dye-sensitized solar cells (DSSCs) are another emerging class of hybrid solar cells that have attracted much attention in

recent years. They are constructed with a mesostructured inorganic *n*-type oxide (typically TiO_2), sensitized with an organic or metal complex dye as the light absorber, and infiltrated with an organic *p*-type hole-conductor (e.g., Spiro-OMeTAD).[4] Basically, any conducting material that is easy to process, inexpensive, and abundant, can be utilised towards delivering highly efficient solar cells.

Progressing from DSSCs, hybrid organometal halide perovskite absorbers with a general formula of $(RNH_3)MX_3$ (where $R=C_nH_{2n+1}$; X= halogen I, Br, Cl; M=Pb, Sn)[18], have replaced the dye in DSSCs as the light absorber, and have resulted in solid-state solar cells with PCEs over 10%.[8,11,19] In these organometal halide perovskite devices, the replacement of the mesoporous TiO_2 layer by a mesoporous Al_2O_3 scaffold led to a noteworthy improvement in efficiency, with an open-circuit voltage (V_{oc}) surpassing 1.1V. Therefore, these devices, employing the mesoporous Al_2O_3 scaffold, were termed meso-superstructured solar cells (MSSCs).[8] The confinement of photo-excited electrons within the perovskite phase has been credited for the observed enhancement in V_{oc}. The former facilitates the splitting of quasi Fermi levels for electrons and holes under illumination, which is instrumental to generating the V_{oc}. Further eliminating the need for thermal sintering of the mesoporous Al_2O_3 layer, and further optimisation of the fabrication process, MSSCs with PCEs greater than 12% have been achieved.[20] In addition, $CH_3NH_3PbI_{3-x}Cl_x$ perovskite can operate both as a thin-film absorber, as well as a charge transporter in a solution-processed planar heterojunction solar cell configuration, delivering a power conversion efficiency approaching 5%, despite the absence of a mesostructured layer.[20] This suggests that a simple planar architecture is highly conducive to the efficient operation of the perovskite absorber, questioning the role and influence of the mesostructure pertaining to efficiency enhancement, and

highlighting the emergence of the thin film planar heterojunction as a potentially superior technology.

4.2 Methods

4.2.1 Method Summary

The FTO substrate preparation has been described in detail in section 3.2.1. A compact layer of TiO_2 was deposited on the clean FTO coated glass by spin-coating a mildly acidic solution of titanium isopropoxide in ethanol,[20] before depositing the perovskite film. In the process of dual-source vapour deposition (DSVD), methylammonium iodide (CH_3NH_3I) and lead chloride ($PbCl_2$) acted as organic and inorganic precursor salts that were evaporated simultaneously at an optimal approximate molar ratio (AMR) of 4:1 under 10^{-5} mbar vacuum. Annealing the perovskite absorbers at 100^{o}C for 45 min prior to spin-coating the hole-transporter layer, led to the complete crystallisation of the perovskite layer. After spin-coating the HTM spiro-OMeTAD (dissolved a chlorobenzene solution including Li-TFSI and *t*BP as additives), the devices were capped with silver metal electrodes deposited through thermal evaporation at 10^{-6} mbar to form the photoactive layer.[8] Details of the DSVD of the hybrid mixed-halide perovskites ($CH_3NH_3PbI_{3-x}Cl_x$) are provided in the following sections. All other characterisation and measurement techniques were stated in section 3.3.

4.2.2 Perovskite Film Fabricated by Dual-Source Vapour Deposition

The perovskite film was deposited onto the TiO_2 compact layer-coated FTO substrates through the DSVD of lead chloride ($PbCl_2$) and methylammonium iodide (CH_3NH_3I, i.e., MAI) simultaneously under 10^{-5} mbar vacuum.

Tooling factor estimation: the tooling factor was estimated prior to depositing the perovskite film (see details in section 3.2.3.2.2). Each source was heated up individually, and their deposition rates were monitored. A constant evaporation rate was maintained for each source, and the elapsed time duration was 30 min. The actual deposited thickness on the substrate was measured with a surface profilometer and then the tooling factor for each source was calculated by dividing the sensor-recorded thickness by the actual deposited thickness (refer to Table 4.1). These tooling factors were subsequently applied to the following DSVD process. The deposition rate for MAI typically varied by ±15% during evaporation, while the rate for $PbCl_2$ varied by approximately ±10%.

Source	Density	Evaporation rate	Values on sensors	Real thickness in average	Tooling factor
Source 1: CH_3NH_3I	1 g cm^{-3}*	15 Å s^{-1}	30 kÅ	1.39 μm	**2.16**
Source 2: $PbCl_2$	5.85 g cm^{-3}	5 Å s^{-1}	10 kÅ	185 nm	**5.41**

Table 4.1: Tooling factor measurements of the dual-source vapour-deposition system
*The density of CH_3NH_3I is assumed to be 1 g cm^3 because its precise density is not known.

Dual-Source Vapour Deposition (DSVD): The experimental system and setup for the DSVD method have been described in section 3.2.3.2. The inorganic ($PbCl_2$) and organic (MAI) sources were simultaneously thermally-evaporated under a 10^{-5} mbar vacuum chamber to form the mixed-halide perovskite film. The best performing perovskite devices were optimised by varying key parameters of the deposition conditions such as the deposition rates and times, of both sources. In particular, device performance was also found to react sensitively to the composition ratio of MAI relative to $PbCl_2$, and the overall deposited thickness, which created an avenue for device optimisation.

Device Optimisation: The following steps were trialled to optimise device efficiency. (1) The approximate molar ratio (AMR) of MAI to $PbCl_2$ was varied from 1:1 to 7:1 while the as-annealed film thickness was kept constant at 125 nm as shown in Figure 4.1a. (2) With the AMR of MAI to $PbCl_2$ kept at the discovered optimum AMR of 3.5:1, the film thickness was allowed to vary from 125 nm to 500 nm, where a film thickness around 250 nm was discovered to be optimal range (refer to Figure 4.1b). (3) The AMR of MAI:$PbCl_2$ was further tuned for 330 nm films to obtain the optimum AMR of 4:1 (Figure 4.1c). (4) The hole-transporter thickness (i.e., varying solution concentration) and Li-TFSI dopant concentration were optimised to maximise the performance of the deposited ~330 nm-thick perovskite films, with a MAI:$PbCl_2$ AMR of 4:1. The conditions for the optimisation of device performance as the Li-TFSI concentration was varied are shown in Figure 4.1d.

Having established the optimal conditions for device performance, the optimal deposition rates were realised at 5.3 A s^{-1} for MAI (crucible temperature around 116 °C) and 1 A s^{-1} for $PbCl_2$ (crucible temperature around 320 °C), for an evaporation time of 128 min as shown in Table 4.2.

Source	Evaporation rate	Values on sensors	Tooling factor	Approximate molar ratio on substrate* (CH_3NH_3I:$PbCl_2$)
Source 1: CH_3NH_3I	5.3(±0.8) Å s^{-1}	42.4 kÅ	**2.16**	4:1
Source 2: $PbCl_2$	1 Å s^{-1}	8 kÅ	**5.41**	

Table 4.2: Optimised deposition conditions for the evaporated perovskite solar devices.
*The calculation of the approximate molar ratio is based on the assumption of the densities shown in Table 4.1 as well as the relative molecular mass of 157 for CH_3NH_3I and 278 for $PbCl_2$.

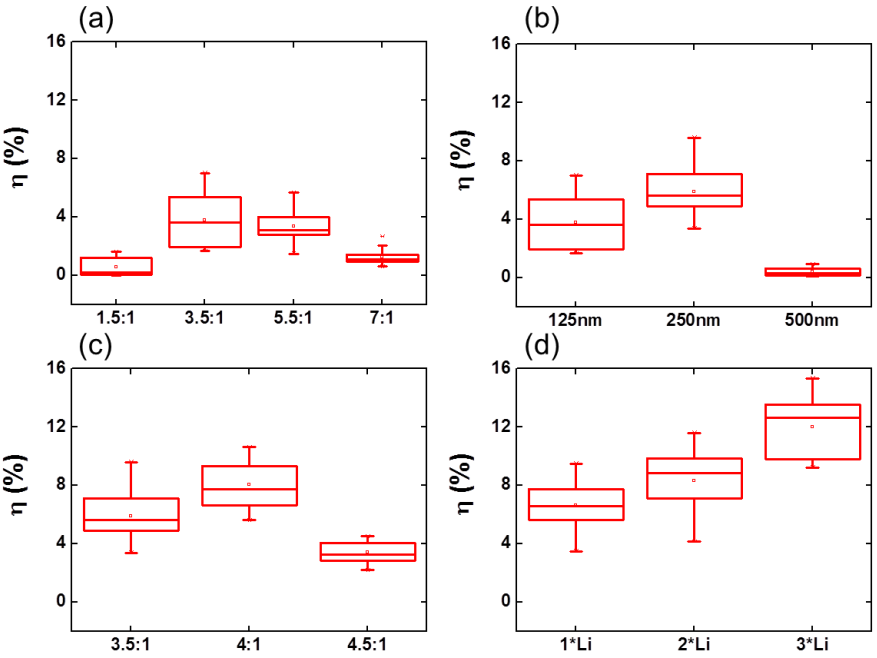


Figure 4.1: **Statistics of solar cells optimisation**. Solar cells efficiency statistics for (a) the AMR from 1.5:1 to 7:1 at thickness of 125 nm; (b) the thickness from 125 nm to 500 nm at the AMR of 3.5:1; (c) the AMR from 3.5:1 to 4.5:1 at thickness of 330 nm; (d) Li-TFSI dopant concentration at 8.5 mM (1*Li), 17 mM (2*Li) and 26 mM (3*Li) at the AMR of 3.5:1 and thickness of 330 nm.

4.2.3 Perovskite Film Fabricated by Solution Processing

The fabrication of solution-processed planar heterojunction devices has been described in detail in section 3.2.3.1.

4.2.4 Hole-Transporter Deposition and Electrode Deposition

Details regarding the deposition of the HTM and metal electrode for both vapour-deposited and solution-processed devices have been covered in section 3.2.4.

4.3 Results and Discussion

4.3.1 Dual-Source Vapour Deposition and Crystallographic Analysis

The DSVD technique was applied to create uniform flat films of the mixed halide perovskite (i.e., $CH_3NH_3I_{3-x}Cl_x$). An illustration of the DSVD's setup along with an

illustration of a planar heterojunction *p-i-n* perovskite solar cell is shown in Figure 4.2. As shown in the bottom of the device illustrated in Figure 4.2b (the side from which the light is incident), the device was constructed on FTO-coated glass, which was firstly coated with a compact layer of *n*-type TiO_2, acting as the electron transporting contact. On top of the *n*-type compact layer, the perovskite layer was then deposited, followed by spin-coating the *p*-type hole conductor spiro-OMeTAD, which assures holes-selective contacts at the silver cathode. Given that the purpose of this work was to study the properties of the vapour-deposited perovskite films, the *n*-type compact layer of TiO_2 and *p*-type HTM spiro-OMeTAD hole transporter were both fabricated via spin-coating as is standard procedure, described in Chapter 3.[17]

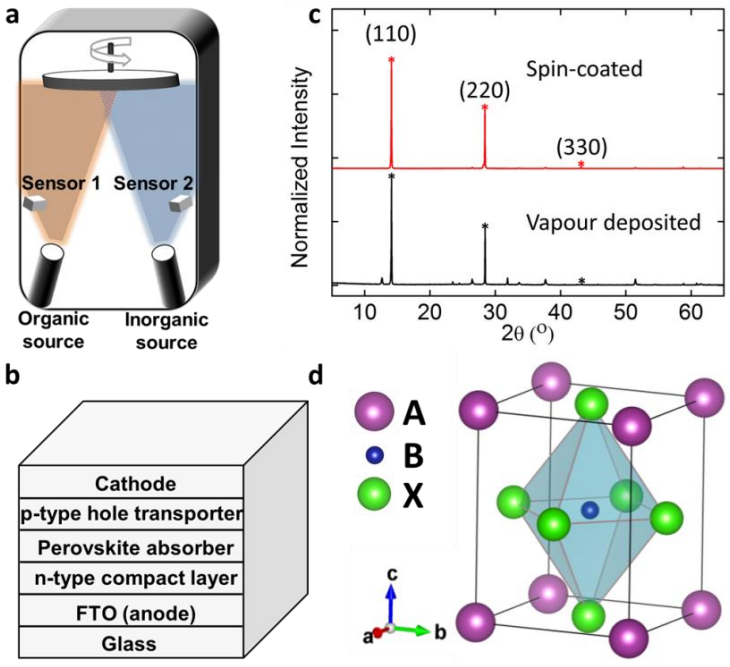


Figure 4.2: Material deposition system and characterisation. Illustration of **(a)** Dual-source thermal evaporation system for depositing the perovskite absorbers; the organic source was methylammonium iodide (CH_3NH_3I) and the inorganic source lead chloride ($PbCl_2$); **(b)** Generic structure of a planar heterojunction *p-i-n* perovskite solar cell; **(c)** X-ray diffraction (XRD) spectra of a solution processed perovskite film (red) and vapour deposited mixed halide perovskite film (black) onto compact TiO_2-coated FTO glass,. The baseline is offset for ease of comparison and the intensity has been normalised. **(d)** Crystal structure of the perovskite absorber adopting the perovskite ABX_3 form, where A = methylammonium, B = Pb and X = I or Cl.

In Fig. 4.2c, the XRD patterns of $CH_3NH_3PbI_{3-x}Cl_x$ perovskite films fabricated by spin-coating and vapour-deposition were compared. The major diffraction peaks at 14.12°, 28.44°, and 43.23°, corresponding to the (110), (220), and (330) phases are in identical positions for both solution processed and vapour deposited films. This is a clear indication that the same mixed halide $CH_3NH_3PbI_{3-x}Cl_x$ perovskite film with a tetragonal crystal structure, has been successfully fabricated via both techniques.[8] Despite the presence of the small peak at 12.65°for PbI_2 (the (001) diffraction peak) and the lack of a measurable peak at 15.68° for $CH_3NH_3PbCl_3$ (the (110) diffraction peak) in the vapour deposited film, which indicates a high level of phase purity. Moreover, the XRD reflections from the vapour deposited film generated more diffraction peaks in comparison to those from the spin-coated sample. This suggests that the vapour-deposited perovskite film displayed lower crystallinity, and possessed more amorphous parts. Further study regarding the additional multiple diffraction peaks and its relation to the processing conditions will be discussed in detail in Chapter 5. A diagram of the crystal structure is shown in Figure 4.2d. With regards to the difference between single halide $CH_3NH_3PbI_3$ and the mixed halide $CH_3NH_3PbI_xCl_{3-x}$ perovskite materials, the contribution of Cl^- toms is still rather unclear. A theoretical prediction has been made by De Angelis and co-researchers that Cl atoms are expected to reside in the apical positions, out of the PbI_4 plane, as opposed to the equatorial octahedral sites.[21]

4.3.2 Microstructural Analysis

To understand the morphology of perovskite films, a comparison between the thin film topology and cross-sectional structure of devices fabricated by both DSVD and the solution process, was conducted. First, considerable differences in film morphologies produced by the two fabrication methods are clearly highlighted in the top-view

scanning electron microscope (SEM) images in Figure 4.3a and Figure 4.3b. The vapour-deposited film appears to fully cover the layer underneath, with crystalline features on the hundreds of nanometre length-scale. Contrarily, the perovskite film fabricated by spin-coating only partial films coats on the substrate, with what appears to be crystalline "platelets" evident on the tens of microns length-scale. The voids between the crystals grain boundaries in the spin-coated films directly extend to the compact TiO_2 layer. Figure 4.3c and 4.3d show the cross-sectional images of the completed devices and display further structural information on crystal size. The vapour deposited perovskite layer in Figure 4.3c appears similar feature to the FTO layer, despite of slightly larger crystal size, and the solution-processed perovskite layer in Figure 4.3d is extremely smooth, which agrees with a much larger grain size than the range of view of the SEM images. Note that for both set of films, the crystal sizes are larger than what can be determined from the peak width of the XRD spectra (~ 400nm) because of the machine broadening. Upon zooming out, the vapour deposited film in Figure 4.3e remains uniform with an average film thickness of approximately 330 nm. However, the solution-processed film in Figure 4.3f shows an undulating nature with considerable variations in film thickness spanning from 50 to 410 nm. Note that the cross section in Figure 4.3f is still within a single "platelet", showing even greater long-range roughness in areas where the perovskite film appears to be entirely absent (additional multiple SEM images of this sample show a thickness variation from 0 to 465 nm).

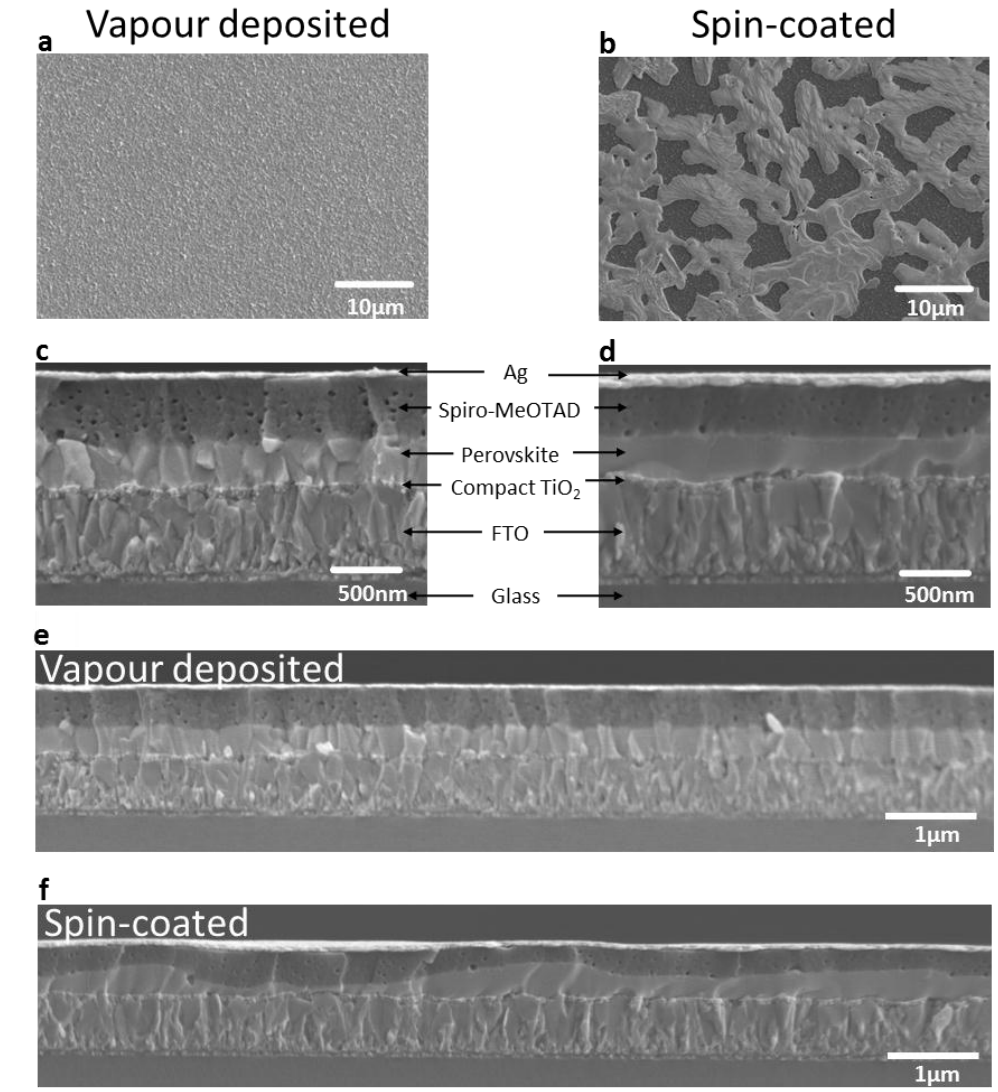


Figure 4.3: Thin-film topology characterisation. Scanning electron microscopy (SEM) top views of **(a)** a dual-source deposited and **(b)** a spin-coated perovskite film; Cross-sectional SEM images under high magnification of complete solar cells constructed with a **(c)** dual-source deposited perovskite film and **(d)** spin-coated perovskite film; Cross-sectional SEM images under lower magnification of completed solar cells constructed with **(e)** dual-source deposited and **(f)** spin-coated perovskite films.

After deposition, the colour of the samples varied in response to the composition of the two sources. For the best-performing devices, a reddish-brown colour was observed and the film appears to be partially crystallised in the topological SEM image of the as-deposited film (Figure 4.4a). Annealing the as-deposited films at 100 °C for 45 min in the N_2-filled glove box before spin-coating the hole-transporter enabled full crystallisation of the perovskite. This process also darkens the colour and

results in an apparent growth of the crystal grains that are made visible in the SEM image, (as shown in Figure 4.4b). After annealing, the best-performing samples were found to exhibit an average thickness of approximately 330 nm. As would be expected from the non-stoichiometric as-deposited molar ratio, there is a clear significant mass loss and therefore, thickness loss, that occurs during perovskite film formation.

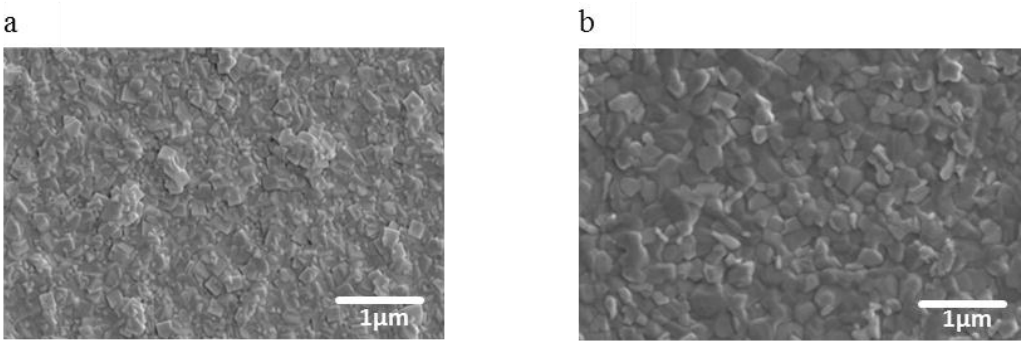


Figure 4.4: Top-view SEM images for the vapour-deposited perovskite films. (a) As-deposited perovskite film; **(b)** post-annealed perovskite film.

4.3.3 Photo-physical Analysis

To understand the photo-physical properties of the vapour-deposited perovskite film, the optical absorption and reflection spectra were studied as shown in Figure 4.5. A rising edge, centred approximately at 1.64 eV was identified as the absorption onset, which is consistent with previous reports on solution-processed $CH_3NH_3PbI_{3-x}Cl_x$[8,22] and $CH_3NH_3PbI_3$[23] perovskite films. However, the identification of a precise bandgap energy poses some difficulty due to the lack of information on excitonic effects and the accurate physical nature of the electronic structure near the band edge.[21,24,25,26] In theory, the absorption onset for a direct semiconductor is expected to exhibit a broad regime for which $\alpha \propto (E-E_g)^{½}$ absence of electrons-holes interaction according to

Fermi Golden rule.[27] However, if the Coulomb interaction between electrons and holes is considered, the optical absorption agrees with Elliot theory, and the absorption coefficient α is given by Elliot formula.[28] The creation of resonant exciton will result in enhancements effects of absorption at the band edge that could be as a possible reason for the initial steep rise of the absorption as shown in Figure 4.5b.[29] For the tri-halide $CH_3NH_3PbI_3$ perovskite, the range of exciton binding energies have been recognised from 19 meV[30] to 50 meV[31], that are comparable to the characteristic thermal energy at room temperature. In other words, the exciton binding energy is sufficiently high, for enhancement effects of the absorption at the band edge to be observed at room temperature. In addition, as can be seen in Figure 4.5a, the transmission and reflectance spectra present thin-film-interference (Fabry-Perot) effects where photon energies are smaller than the absorption onset of 1.64 eV. It suggests that the film thickness is homogeneous and uniform and that the film surface is optically flat with a constant refractive index, thereby, preventing light scattering.

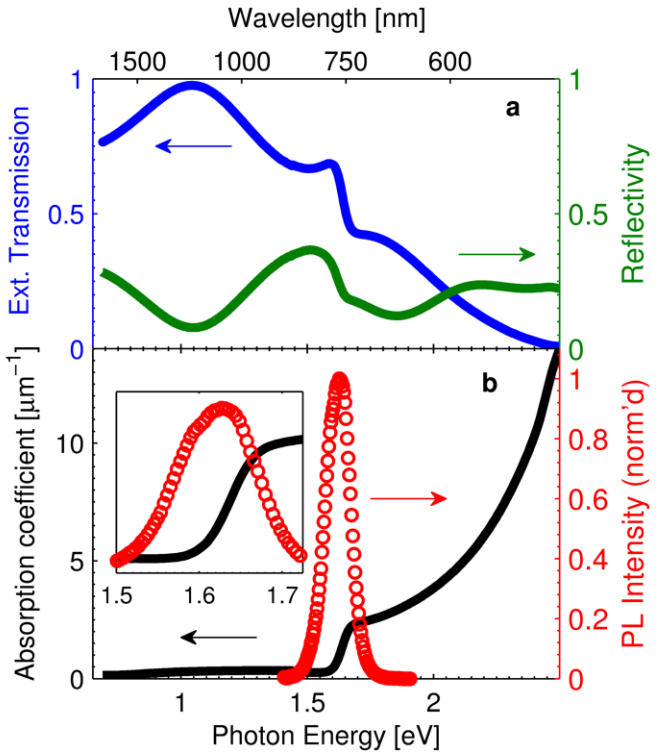


Figure 4.5: Optical properties. (a) External optical transmission ($T_{ext} = I_{transmitted}/I_{incident}$, blue) and reflection spectrum ($R = I_{reflected}/I_{incident}$, green) of evaporated $CH_3NH_3PbI_{3-x}Cl_x$. (b) Absorption coefficient $\alpha = -1/d \ln(T_{ext}/(1-R))$, calculated from the data in (a) and the thickness d. Inset: magnified plot of α^2 vs E, (E: photon energy) around the absorption edge from which a band gap energy of 1.620eV was determined (see text). Data in this figure was taken by *Christian Wehrenfennig*.

The photoluminescence emission spectrum of vapour-deposited $CH_3NH_3PbI_{3-x}Cl_x$ is shown alongside the absorption data in Figure 4.5b. It clearly shows that the PL emission occurs at a slightly down-shifted energy in comparison to the absorption of the bandgap, where its centre of mass takes place at 1.617 eV near the tail of the absorption edge on the low-energy site. Such shift in energy is known as Stokes shifts, which are a very common phenomenon in semiconductor materials due to various reasons - including electronic migration to lower energy[32] and lattice relaxation (polaronic effects).[33,34]

4.3.4 Solar Cell Characterisation

Figure 4.6 shows the current density–voltage (*J-V*) curves measured under simulated AM1.5 101 mWcm^{-2} irradiance sun light for the most efficient dual-source vapour deposited and spin-coated planar heterojunction perovskite devices. The best dual-source vapour deposited perovskite device exhibited J_{sc} of 21.5 mAcm^{-2}, V_{oc} of 1.07 V, and a fill factor of 0.68 - yielding a PCE of 15.4%. In the same batch, the best performing spin-coated flat-junction perovskite solar cell produced a J_{sc} of 17.6 mA cm^{-2}, V_{oc} of 0.84 V, and a fill factor of 0.58 - yielding an overall η of 8.6%. The extracted performance parameters for these best performing cells and the average and standard deviation of a batch of 12 dual-source vapour deposited perovskite solar cells are shown in Table 4.3.

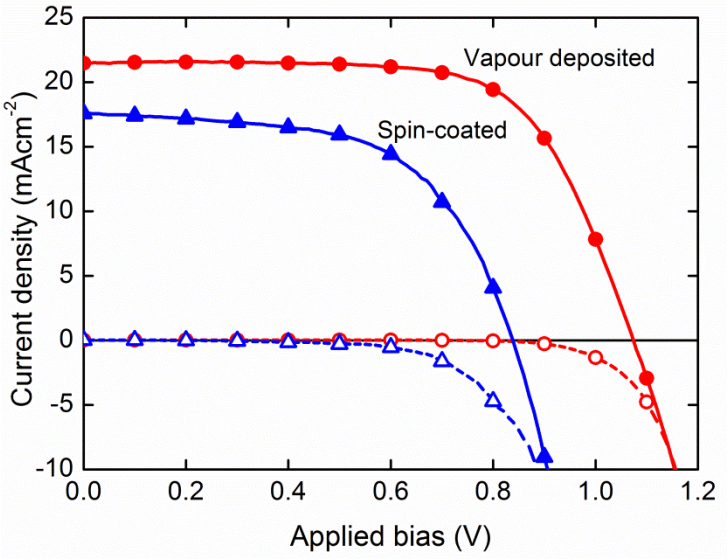


Figure 4.6: Solar cell performance. Current density-voltage (J-V) curves of the best performing solution processed (blue lines, triangles) and vapour deposited (red lines, circles) planar heterojunction perovskite solar cells measured under simulated AM1.5 sunlight of 101 mWcm^{-2} irradiance (solid lines) and in the dark (dashed lines).

	J_{sc} (mAcm^{-2})	V_{oc}(V)	*FF*	PCE (%)
Vapour deposited	21.5	1.07	0.68	15.4
Vapour deposited (average ± s.d.)	18.9 ± 1.8	1.05 ± 0.03	0.62 ± 0.05	12.3 ± 2.0
Spin-coated	17.6	0.84	0.58	8.6

Table 4.3: Solar cell performance parameters. Solar cell performance parameters extracted from the current voltage curves presented in Figure 4.6, and additionally the average and standard deviation (s.d) of a batch of 12 identically processed planar heterojunction vapour deposited $CH_3NH_3PbI_{3-x}Cl_x$ perovskite solar cells

The dual-source vapour deposition technique provides superior uniformity of the coated perovskite films over a range of length-scales, which substantially results in improved solar cell performance. In optimising the performance of the planar heterojunction perovskite solar cells, perovskite film thickness is a critical parameter. If the film is too thin, it would result in insufficient absorption of sunlight. Whereas, in the case of an excessively thick film, there is a high risk of the electron and hole (or exciton) diffusion length being shorter than the thickness of the film, presenting a bottleneck that the charge would not be extracted at the *p* and *n*-type heterojunctions. Moreover, the complete absence of perovskite material in some areas of the solution-processed films (pinholes) will cause direct contact of the *p*-type HTM and *n*-type electron-selective layer. This creates to a shunting path that is probably, partially responsible for the lower V_{oc} and fill factor in the spin-coated planar heterojunction devices.[20,35]

The results presented above not only set a lower limit of 330 nm (the film thickness) for the electron and hole diffusion length in this perovskite film, but also demonstrate that the solid perovskite layer can operate extremely well in planar heterojunction solar cells.

A follow-up study showed that the PL spectrum of the perovskite film derived by DSVD is homogeneously broadened with a line width of 103meV. This film was

characterised by a relatively slow decay of the carrier lifetime over several hundred nanoseconds.[36] More work on electron-hole diffusion length has been carried out to understand the role and mechanisms of primary excitation and free charge generation in these materials post the publication of this work.[36,37,38] Stranks *et al* determined that the carrier diffusion lengths are over 1 μm in mixed-halide perovskite ($CH_3NH_3PbI_{3-x}Cl_x$) film.[36] This further explains the superior performance in the planar heterojunction mixed-halide perovskite solar cells.

4.4 Summary

In this chapter, thin-film perovskite solar cells fabricated by the DSVD technique achieved a solar-to-electrical PCE of over 15% with an open-circuit voltage of 1.07 V, highlighting the importance of a high-quality perovskite film in realising a superior performance in planar heterojunction devices. This currently represents the highest efficiency yet reported for any emerging PV technology. Other advantages of the derived perovskite film include compatibility with low temperature processing methods, feasibility of solution and vapour deposition, coupled with the simplicity of the device architecture, and a plethora of other conceivable metal and organic salts which could form the perovskite structure, it is no wonder the perovskite absorbers appear to be uniquely positioned for incorporation into highly efficient solar cells. Additionally, an interesting possibility for the vapour-deposited perovskite technology is to employ it as a "top cell" in a "hybrid tandem junction" with either c-Si, CIGS or other emerging concepts. Though ultimately, an "all-perovskite" multi-junction cell should be realisable.[39] In Chapter 7, a demonstration of an "all-perovskite" tandem device will be proposed.

References

1. Green, M. A. Silicon Photovoltaic Modules: a Brief History of the First 50 Years. *Prog. Photovoltaics Res. Appl.* **13,** 447–455 (2005).

2. Graetzel, M., Janssen, R. A. J., Mitzi, D. B. & Sargent, E. H. Materials interface engineering for solution-processed photovoltaics. *Nature* **488,** 304–12 (2012).

3. Chopra, K. L., Paulson, P. D. & Dutta, V. Thin-film solar cells: an overview. *Prog. Photovoltaics Res. Appl.* **12,** 69–92 (2004).

4. O'Regan, B. & Grätzel, M. A low-cost, high-efficiency solar cell based on dye-sensitized colloidal TiO_2 films. *Nature* **353,** 737 (1991).

5. Halls, J. J. M. *et al.* Efficient photodiodes from interpenetrating polymer networks. *Nature* **376,** 498 (1995).

6. Yu, G., Gao, J., Hummelen, J. C., Wudl, F. & Heeger, A. J. Polymer Photovoltaic Cells: Enhanced Efficiencies via a Network of Internal Donor-Acceptor Heterojunctions. *Science.* **270,** 1789–1791 (1995).

7. Green, M. A., Emery, K., Hishikawa, Y., Warta, W. & Dunlop, E. D. Solar cell efficiency tables (version 40). *Prog. Photovoltaics Res. Appl.* **20,** 606–614 (2012).

8. Lee, M. M., Teuscher, J., Miyasaka, T., Murakami, T. N. & Snaith, H. J. Efficient Hybrid Solar Cells Based on Meso-Superstructured Organometal Halide Perovskites. *Science* **338,** 643–647 (2012).

9. Kojima, A., Teshima, K., Shirai, Y. & Miyasaka, T. Organometal halide perovskites as visible-light sensitizers for photovoltaic cells. *J. Am. Chem. Soc.* **131,** 6050–6051 (2009).

10. Kim, H.-S. *et al.* Lead iodide perovskite sensitized all-solid-state submicron thin film mesoscopic solar cell with efficiency exceeding 9%. *Sci. Rep.* **2,** 591 (2012).

11. Noh, J. H., Im, S. H., Heo, J. H., Mandal, T. N. & Seok, S. Il. Chemical management for colorful, efficient, and stable inorganic-organic hybrid nanostructured solar cells. *Nano Lett.* **13,** 1764–9 (2013).

12. Zhao, J., Wang, A., Green, M. A. & Ferrazza, F. 19.8% Efficient "Honeycomb" Textured Multicrystalline and 24.4% Monocrystalline Silicon Solar Cells. *Appl. Phys. Lett.* **73,** 1991 (1998).

13. Shah, A., Torres, P., Tscharner, R., Wyrsch, N. & Keppner, H. Photovoltaic Technology: The Case for Thin-Film Solar Cells. *Science.* **285,** 692–698 (1999).

14. Tao, C. S., Jiang, J. & Tao, M. Natural resource limitations to terawatt-scale solar cells. *Sol. Energy Mater. Sol. Cells* **95,** 3176–3180 (2011).

15. Huynh, W. U., Dittmer, J. J. & Alivisatos, A. P. Hybrid nanorod-polymer solar cells. *Science* **295,** 2425–2427 (2002).

16. Arici, E., Sariciftci, N. S. & Meissner, D. Hybrid Solar Cells Based on Nanoparticles of CuInS2 in Organic Matrices. *Adv. Funct. Mater.* **13,** 165–171 (2003).

17. McDonald, S. A. *et al.* Solution-processed PbS quantum dot infrared photodetectors and photovoltaics. *Nat. Mater.* **4,** 138–142 (2005).

18. Cheng, Z. & Lin, J. Layered organic–inorganic hybrid perovskites: structure, optical properties, film preparation, patterning and templating engineering. *CrystEngComm* **12,** 2646–2662 (2010).

19. Heo, J. H. *et al.* Efficient inorganic-organic hybrid heterojunction solar cells containing perovskite compound and polymeric hole conductors. *Nat. Photonics* 1–6 (2013). doi:10.1038/NPHOTON.2013.80

20. Ball, J. M., Lee, M. M., Hey, A. & Snaith, H. J. Low-temperature processed meso-superstructured to thin-film perovskite solar cells. *Energy Environ. Sci.* **6,** 1739–1743 (2013).

21. Mosconi, E., Amat, A., Nazeeruddin, M. K., Grätzel, M. & De Angelis, F. First Principles Modeling of Mixed Halide Organometal Perovskites for Photovoltaic Applications. *J. Phys. Chem. C* (2013). doi:10.1021/jp4048659

22. Stoumpos, C. C., Malliakas, C. D. & Kanatzidis, M. G. Semiconducting tin and lead iodide perovskites with organic cations: phase transitions, high mobilities, and near-infrared photoluminescent properties. *Inorg. Chem.* **52,** 9019–38 (2013).

23. Cai, B., Xing, Y., Yang, Z., Zhang, W.-H. & Qiu, J. High performance hybrid solar cells sensitized by organolead halide perovskites. *Energy Environ. Sci.* **6,** 1480 (2013).

24. Umebayashi, T., Asai, K., Kondo, T. & Nakao, A. Electronic structures of lead iodide based low-dimensional crystals. *Phys. Rev. B* **67,** 155405 (2003).

25. Koutselas, I. B., Ducasse, L. & Papavassiliou, G. C. Electronic properties of three- and low-dimensional semiconducting materials with Pb halide and Sn halide units. *J. Phys. Condens. Matter* **8,** 1217–1227 (1996).

26. Even, J., Pedesseau, L., Jancu, J.-M. & Katan, C. Importance of Spin–Orbit Coupling in Hybrid Organic/Inorganic Perovskites for Photovoltaic Applications. *J. Phys. Chem. Lett.* **4,** 2999–3005 (2013).

27. Fox, M. *Optical Properties of Solids*. 416 (OUP Oxford, 2010).

28. Elliott, R. Intensity of Optical Absorption by Excitons. *Phys. Rev.* **108,** 1384–1389 (1957).

29. Sturge, M. Optical Absorption of Gallium Arsenide between 0.6 and 2.75 eV. *Phys. Rev.* **127,** 768–773 (1962).

30. Sun, S. *et al.* The origin of high efficiency in low-temperature solution-processable bilayer organometal halide hybrid solar cells. *Energy Environ. Sci.* **7,** 399 (2014).

31. Tanaka, K. *et al.* Comparative study on the excitons in lead-halide-based perovskite-type crystals $CH_3NH_3PbBr_3$ $CH_3NH_3PbI_3$. *Solid State Commun.* **127,** 619–623 (2003).

32. Bässler, H. & Schweitzer, B. Site-Selective Fluorescence Spectroscopy of Conjugated Polymers and Oligomers. *Acc. Chem. Res.* **32,** 173–182 (1999).

33. Pope, M. & Swenberg, C. E. *Electronic Processes in Organic Crystals and Polymers*. 1328 (Oxford University Press, 1999).

34. Pelant, I. & Valenta, J. *Luminescence Spectroscopy of Semiconductors*. 542 (Oxford University Press, 2012).

35. Snaith, H. J., Greenham, N. C. & Friend, R. H. The Origin of Collected Charge and Open-Circuit Voltage in Blended Polyfluorene Photovoltaic Devices. *Adv. Mater.* **16,** 1640–1645 (2004).

36. Stranks, S. D. *et al.* Electron-hole diffusion lengths exceeding 1 micrometer in an organometal trihalide perovskite absorber. *Science* **342,** 341–4 (2013).

37. Xing, G. *et al.* Long-range balanced electron- and hole-transport lengths in organic-inorganic $CH_3NH_3PbI_3$. *Science* **342,** 344–7 (2013).

38. Wehrenfennig, C., Eperon, G. E., Johnston, M. B., Snaith, H. J. & Herz, L. M. High Charge Carrier Mobilities and Lifetimes in Organolead Trihalide Perovskites. *Adv. Mater.* **26,** 1584–1589 (2014).

39. Beiley, Z. M. & McGehee, M. D. Modeling low cost hybrid tandem photovoltaics with the potential for efficiencies exceeding 20%. *Energy Environ. Sci.* **5,** 9173 (2012).

Chapter 5

A Comparison between Two-Layer Sequential Vapour Deposition and Dual-Source Vapour Deposition Fabrication Methods

Content and Summary

Efficient planar heterojunction mixed halide (i.e., $CH_3NH_3PbI_{3-x}Cl_x$) perovskite solar cells fabricated by dual-source vapour deposition (DSVD) have been presented in Chapter 4. The previous work showed that the performance of perovskite devices is strongly dependent on film morphology. To expand the vapour deposition technique and to attain further control over the film deposition process, this chapter develops an alternative vapour deposition method, i.e., two-layer sequential vapour deposition (SVD), to fabricate efficient planar heterojunction solar cells incorporating with single halide perovskite $CH_3NH_3PbI_3$ as the light absorber. Analyses into the crystallographic and photo-physical properties of the perovskite films fabricated under various conditions demonstrate that regardless of the film morphology, the

amount of precursors reacting in the fabrication process play a critical role in forming the appropriate material properties, while an optimal annealing process improves the crystallinity of the perovskite films. Additionally, this chapter compares the halide perovskite films fabricated between the SVD and DSVD in terms of crystallinity, uniformity, and carrier lifetimes. Integrating the optimised perovskite films fabricated by both (SVD and DSVD) techniques results in the devices that both are able to produce PCEs surpassing 15%. This work highlights the merits of the vapour deposition techniques utilised, and emphasises the feasibility of employing these techniques for the fabrication of efficient planar heterojunction devices.

5.1 Introduction

Due to its easy processability, cost-effectiveness and abundance, hybrid organic-inorganic halide perovskite materials have gained much attention over the past 2 years.[1,2,3,4,5] The perovskite film acts not only as a light harvester, but also as an electron and hole conductor.[1] Furthermore, its ambipolar semiconducting nature enables the feasible construction of planar heterojunction configurations in the absence of a mesostructure.[6,7,8,9] This feature has also been demonstrated in Chapter 4.

The conventional one-step solution-based technique via spin coating has been used to fabricate planar heterojunction perovskite devices, in which a mixture of the organic and inorganic precursors (e.g., methylammonium halide MAX and lead halide PbX_2 where X is the halogen I, Br or Cl) was dissolved in a polar aprotic solvent.[10,12] While this presents a simple method that can be used to deposit the thin film, it often results in pinholes and incomplete surface coverage, which allow undesired contact between the HTM and the underlying electron collecting layer.[7] The top metal electrode may also penetrate through the pinholes, resulting in the shunting paths. Recently, a solution-based sequential two-step deposition method was successfully used to fabricate high quality perovskite films resulting in efficient perovskite devices.[11] In this two-step method, lead halide is spin-coated on various substrates such as ZnO[6], TiO_2,[12] as well as the conducting polymer poly(3,4-ethylenedioxythiophene): poly(4-styrenesulfonate) (PEDOT: PSS),[13] prior to the subsequent deposition of methyl halides either by dip coating,[11] or spin coating[14]. However, the solution-based two-step processing method often results in surface roughness, which is characteristic of a coat that can be readily peeled off from the substrate. In addition, the efficiency of converting the entire PbI_2 film into a perovskite layer in the

spin-coating/dip-coating two-step technique is determined by the extent of penetration achieved by the organic precursor, which in essence limits the transformation process into pure perovskite. Also, finding suitable solvents for the solution-associated two-step technique is a significant challenge and this also restricts expansion into other families of perovskites.[15]

Vacuum evaporation is amongst the most promising techniques currently been used for the construction of multi-junction solar cells. It is already being employed in the large scale industrial production of high quality photovoltaic thin-films (e.g., a-Si, $Cu(InGa)S_2$, and CdTe).[16,17] Chapter 4 has showed that the optimal dual-source vapour deposited mixed-halide perovskite film yields a device with a PCE of over 15%. Recently, a SVD technique has been proposed for the fabrication of a perovskite film on top of a fullerene C_{60} bi-layer without a hole transporter layer.[18] However, the device performance achieved by using this method falls very short of that achieved by the DSVD method at a PCE of 5.4%[18]– this raises the question of whether various vapour deposition techniques can lead to significant differences in the film properties, and overall device performance.

This work entailed the development of a SVD method for the fabrication of planar heterojunction solar cells incorporating with the single halide perovskite $CH_3NH_3PbI_3$ film. In order to acquire a better understanding of this technique, an investigation was conducted to determine the crystallographic and photo-physical properties of the perovskite films fabricated by the SVD technique under different optimisation conditions. The findings indicated that an appropriate composition of the precursors is vital to forming the right perovskite material. Any excess of organic and inorganic constituents resulted in a lower crystallinity crystal structure within the perovskite

films. Furthermore, it showed that an optimal annealing condition assists in improving the crystallinity and the purity of the perovskite film, while extended annealing degrades the perovskite film, possibly increasing the amorphous parts of the films. A complementary study of the crystallographic and photo-physical properties of films produced by SVD and DSVD techniques, established that both vapour deposition techniques are capable of producing high-quality perovskite films with remarkable crystallinity, uniformity, and long carrier lifetimes. Hence, the optimisation of perovskite films utilising SVD and DSVD techniques enabled the fabrication of efficient planar heterojunction devices with PCEs exceeding 15%.

5.2 Methods

5.2.1 Method Summary

The preparation of the FTO substrate was described in detail in section 3.2.1. A compact layer of TiO_2 was deposited on a clean FTO–coated glass, by spin-coating a mildly acidic solution of titanium isopropoxide in ethanol. Subsequently, the perovskite film was deposited onto the compact TiO_2-coated FTO substrate by vapour deposition (i.e. SVD and DSVD). The schematic illustration of the SVD fabrication process is shown in Figure 5.1. PbI_2 and MAI were employed respectively as the organic and inorganic precursor salts to form triiodide perovskite ($CH_3NH_3PbI_3$) film and they were evaporated from separate OLED sources in sequence at 10^{-5} mbar. The DSVD procedures for fabricating triiodide perovskite devices is practically similar to that for the mixed-halide perovskite devices as described in Chapter 4, excluding the categories and composition of the precursors. After the process of vapour evaporation, thermal-annealing helped to fully crystallise the perovskite films prior to spin-coating

spiro-OMeTAD (incorporating Li-TFSI and tBP as additives) from a chlorobenzene solution as the HTM. Fabrication of devices was then completed with the thermal evaporation of silver metal electrodes at 10^{-6} mbar.

5.2.2 Perovskite Films Fabricated by Vapour Deposition

Tooling factor estimation: The tooling factor (ratio of the material deposited on the sensors to the amount on the substrate) was estimated by the procedures described in section 3.2.3.2.2. The tooling results are shown in Table 5.1. These tooling factors were subsequently applied throughout the following process of vapour deposition to estimate the as-deposited thickness of the films.

Source	Density	Evaporation rate	Values on sensors	Real thickness in average	Tooling factor
Source 1: PbI_2	6.15 g cm^{-3}	5 Å s^{-1}	10 kÅ	500 nm	**2**
Source 2: CH_3NH_3I	1 g cm^{-3}*	15 Å s^{-1}	30 kÅ	1.39 μm	**2.16**

Table 5.1: Tooling factor measurement of the two-layer sequential deposition system.
*The density of CH_3NH_3I is assumed to be 1 g cm^{-3} because its precise density is not known.

Two-layer sequential vapour deposition (SVD) and film optimisation: As described in section 3.2.3.2.2, after loading the samples and pumping down the chamber below 10^{-5}mbar, the inorganic precursor (i.e., PbI_2) was heated up so that the deposition rate was kept at 2 Å/s to enable the forming of the PbI_2 layer on the TiO_2/FTO-coated glass. This was followed by the deposition of the organic source (i.e., MAI) at 20 Å/s. PbI_2 reached 2 Å/s approximately at 270^{o}C while MAI reached 20 Å/s at approximately 130^{o}C.

Upon taking an initial glance at the vapour-deposited films from Chapter 4, it was observed that the optimal perovskite film possessed an approximate total thickness of

330 nm. The resulting film clearly indicated the occurrence of a significant mass and thickness loss during the perovskite film formation, so the compositions of PbI_2 and CH_3NH_3I were examined with a fixed PbI_2 thickness of approximately 250 nm, while the equivalent thicknesses of deposited amount of CH_3NH_3I were varied between 275 nm and 1.85 μm. The different compositions demonstrated in this study are summarised in Table 5.2. The "approximate molar ratio (AMR)" was calculated from the assumed MAI densities and the equivalent thickness which is estimated by the tooling results.

In addition, to understand the crystallisation of the perovskite film under different annealing conditions, various annealing temperature and time were analysed for each composition. It was found that an annealing temperature of 100^{o}C was appropriate to form perovskite films with less organic content (AMR at 1:0.5 and 1:1 of PbI_2: MAI), while an annealing temperature of 120^{o}C was suitable for perovskite films with surplus organic components (AMR at 1:1.7 and 1:3.5 of PbI_2 to MAI) because higher temperatures accelerate the removal of excess organic constituents. The optimum perovskite film was obtained from an AMR of 1:1 corresponding to PbI_2 and MAI, and it was subsequently annealed at 100^{o}C for 30 min. The entire optimisation process and corresponding characterisation are discussed in detail in section 5.3.

PbI_2 thickness		**CH_3NH_3I thickness**		**Approximate molar ratio****
Values on sensors	**Equivalent thickness**	**Values on sensors**	**Equivalent thickness***	
5 kÅ	250 nm	5.9 kÅ	275 nm	**1:0.5**
		11.8kÅ	546 nm	**1:1**
		20 kÅ	925 nm	**1:1.7**
		40 kÅ	1.85μm	**1:3.5**

Table 5.2: Compositional tuning between the organic and inorganic precursors for the two-layer sequential vapour deposited perovskite film. *The equivalent thickness is calculated by using the tooling factor measured in Table 1; **The calculation of AMR is based on the relative molecular mass of 157 for CH_3NH_3I and 461 for Pbl_2 as well as the assumption of the densities shown in Table 5.1.

Dual-source vapour deposition (DSVD): PbI_2 and MAI were used as the precursors to form $CH_3NH_3PbI_3$ perovskite materials. Fabrication and optimisation processes of $CH_3NH_3PbI_3$ perovskite by the DSVD technique in this study followed similar procedures described in Chapter 4 for fabricating mixed-halide perovskite film. The AMR composition of PbI_2 to MAI was varied from 1:0.5 to 1:3 while maintaining the overall film thickness at approximately 320±10 nm. Optimised composition of PbI_2 to MAI was found at 1:1.1 and the optimised deposition rates are summarised in Table 5.3 where PbI_2 and MAI were heated to 2 Å/s and 5 Å/s approximately at 270^{o}C and 115^{o}C respectively. An approximate evaporation time of 40 min was maintained to achieve the described perovskite films.

Source	Evaporation rate	Values on sensors	Tooling factor	Thickness ratio	Approximate molar ratio
Source 1: PbI_2	2 Å s^{-1}	5kÅ	**2**	**1:2.3**	**1:1.1**
Source 2: CH_3NH_3I	5 (±0.8) Å s^{-1}	12.5kÅ	**2.16**		

Table 5.3: Optimised deposition conditions for the dual-source vapour deposited perovskite solar devices. The densities shown in Table 5.1 and the relative molecular mass of 157 for CH_3NH_3I and 461 for PbI_2 are used to calculate the approximate molar ratio of as-deposited materials

5.2.3 Hole-Transporter Deposition and Cathode Deposition

The hole-transporter layer and silver cathode were deposited as described in section 3.2.4. The HTM fabrication followed the HTM deposition recipe optimised in Chapter 4.

5.3 Results and Discussion

In this section, the crystallographic evolution of the perovskite films fabricated by the SVD technique under different conditions (i.e., various compositions of precursors and annealing conditions) were initially investigated. The properties of the optimised perovskite films fabricated via the SVD technique were then compared symmetrically with those of films obtained from DSVD technique with regards to their photo-physical behaviour, microstructure, thermal stability, and device performance.

5.3.1 Optimisation of Perovskite Films Fabricated by the Two-Layer Sequential Vapour Deposition

Generally, the SVD method involved the initial deposition of PbI_2 on the top of the *n*-type compact TiO_2 layer, followed by the evaporation of MAI. The as-deposited films were then annealed to achieve a pure and highly crystalline perovskite film. A *p*-type hole conductor, spiro-OMeTAD was spin coated on top of the perovskite material, to ensure the selective collection of holes at the silver cathode. The schematic for the fabrication procedures is shown in Figure 5.1 and experimental details are provided in section 5.2.

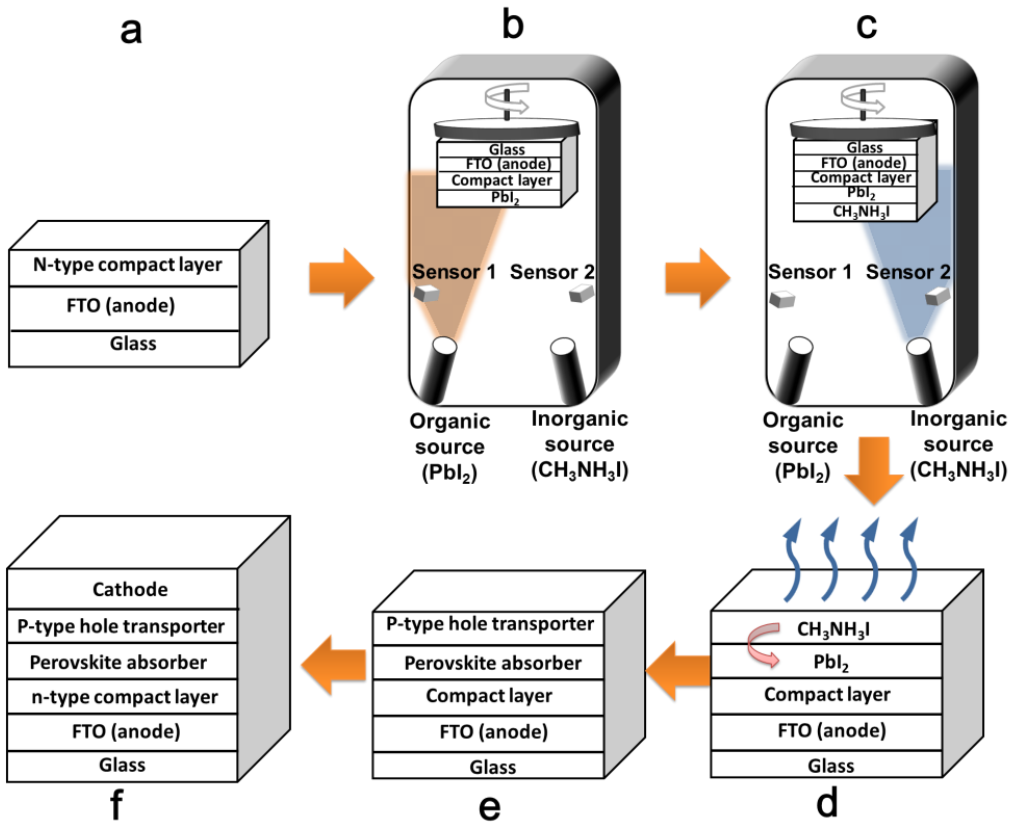


Figure 5.1: Fabrication procedures of two-layer sequential vapour deposition. Illustration of **(a)** deposition of *n*-compact layer on FTO-coated glass; two-layer sequential vapour deposition system for depositing **(b)** the inorganic precursor lead iodide (PbI_2) and **(c)** the organic methylammonium iodide precursor (CH_3NH_3I); **(d)** post-annealing to fully crystallise perovskite; deposition of **(e)** hole transporter layer and **(f)** metal electrode.

To determine the appropriate perovskite film content, the composition between the inorganic and organic precursors was varied. It is critical to drive off unreacted excess organic components and fully crystallise the perovskite film, since the possible traceable insulating precursors or nonstoichiometric compounds always have an adverse effect on the device performance. Also, unreacted organic components especially hygroscopic MAI, easily react with moisture leading to degradation of device stability. Therefore, a proper management of the post-annealing conditions (i.e., time and temperature), was amongst the key factors relevant to achieving stable and high performing perovskite devices. The following section presents the optimisation process with respect to the composition as well as the annealing conditions.

A systematic study on perovskite crystal structure formation within the films for varied PbI_2 and MAI compositions, as a function of annealing times was performed. The X-ray diffraction patterns of these films fabricated with the approximate molar ratios (AMRs) of 1:0.5, 1:1, 1:1.7 and 1:3.5, for PbI_2 with respect to MAI, for various annealing times, are shown in Figure 5.2a, 5.2b, 5.2c, and 5.2d. All perovskite films regardless of the MAI concentration exhibited a brown-pink colour just after the SVD processing without thermal annealing. The colouring instantly progressed to a dark brown shade when the devices were annealed on a hotplate. Interestingly, the film colouration after the SVD fabrication gradually changed from brown-pink to dark-brown without any thermal annealing, when the samples were exposed in a nitrogen-filled glovebox for an extended period (>24h). This is in correlation with the observation that inter-diffusion occurs in the solution-processed stacked layers of PbI_2 and MAI, drawn from a previously published report.[14]

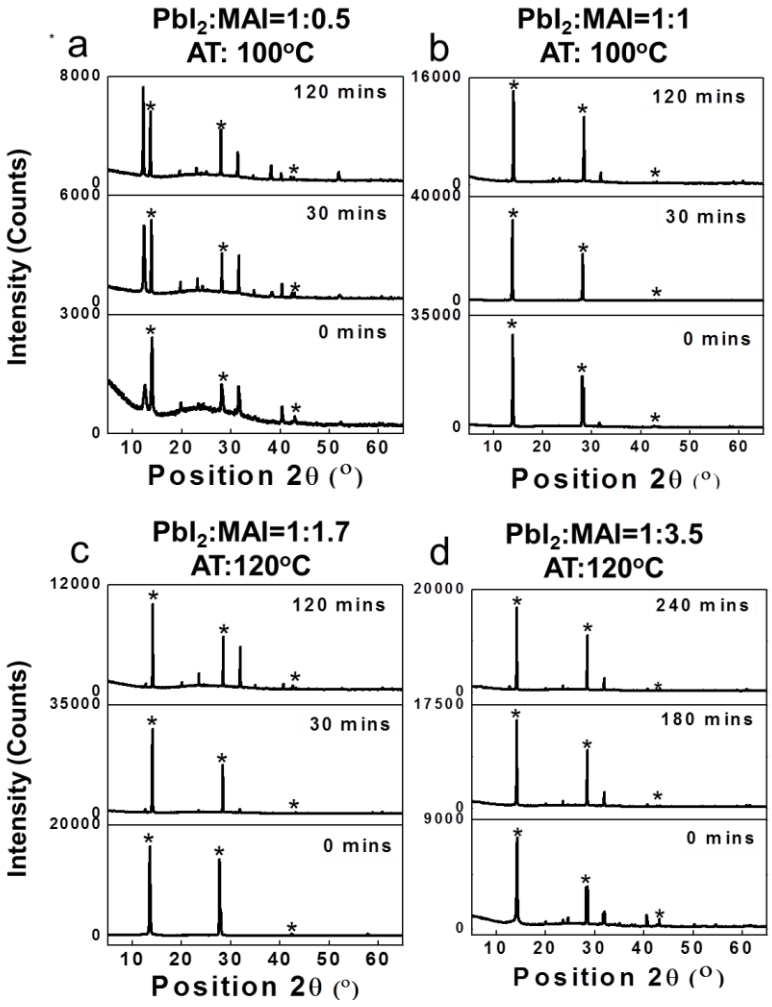


Figure 5.2: Crystal structure of the perovskite films for different compositions of inorganic and organic precursors by sequential vapour deposition. X-ray diffraction (XRD) spectra of sequential vapour deposited films fabricated with the approximate molar ratios of PbI_2 and CH_3NH_3I at (a) 1:0.5; (b) 1:1; (c) 1:1.7 and (d) 1:3.5. The tetragonal symmetry of the perovskite crystal assigned to the (110), (220) and (310) at 14.13°, 28.49° and 43.27°respectively are indicated by star (*). Note that all samples fabricated via the SVD were exposed in the glovebox for at least 24h before measuring the XRD spectra. The sample without any post-annealing (0 min) presented a dark-brown colour during the measuring process.

XRD patterns of the perovskite films fabricated by the SVD technique at an AMR 1:0.5 of PbI_2 to MAI are shown in Figure 5.2a. The formation of $CH_3NH_3PbI_3$ is confirmed by the X-ray diffractometry and the reflections 2θ-angle of (110), (220), and (310) at 14.13°, 28.49° and 43.27° correspond to the tetragonal phase as described elsewhere.[2,11,19,20] A strong peak at 12.65° corresponding to PbI_2 is observed when the sample wasn't annealed (0 min), and the intensity of this reflection increases with the

subsequent annealing at 100^{o}C for 30 min and 120 min successively. The presence of unreacted PbI_2 content suggests that the MAI concentration is insufficient and hence unable to fully convert the PbI_2 into perovskite $MAPbI_3$ at the given AMR of 1:0.5. The relative increase in PbI_2 peaks with respect to (001) reflection of perovskite in the XRD spectrum after long annealing process indicates a thermal degradation of the perovskite into PbI_2 and other organic constituents.

Further increasing the organic content (MAI) to the AMR of 1:1 (PbI_2 to MAI), the perovskite structure is formed after the SVD processing without any thermal-annealing (0 min), as shown by the XRD patterns in Figure 5.2b. The predominant diffraction peaks of the unannealed perovskite film are in good agreement with the data reported by literature pertaining to the tetragonal peaks of (110), (220) and (310) at 14.13°, 28.49° and 43.27° respectively.[2,11,19,20] It should be noted that there are no measurable peaks for unreacted PbI_2 and MAI, at 12.65° and 19.70° respectively contrary to the earlier composition (1:0.5) where a strong unreacted PbI_2 peak was observed. This indicates that both PbI_2 and MAI components reacted completely and have been converted into the perovskite before the annealing step. The increase in the peak intensity is observed when the film is subjected to thermal annealing for 30 min at 100^{o}C, suggesting an improvement in film crystallinity. Interestingly, the extended annealing duration of 120 min generates a few new peaks. The appearance of new peaks with the longer thermal annealing could possibly be due to multiple phase formation as $MAPbI_3$ adopts cubic structure when the temperature exceeding 100^{o}C. It might be associated with the peaks pertaining to the tetragonal phase of the perovskite crystal which may not have been visible due to strong texture effect and preferred orientations of crystallites as discussed by Baikie *et al*.[20] This emphasises that an optimal annealing condition is critical. A short annealing

time would lead to the incomplete crystallisation of the perovskite films while longer annealing times could possibly lead to highly textured films. It must be noted that appearance of new peaks after thermal annealing needs further investigations.

The XRD spectrum in Figure 5.2c obtained from films with the AMR of 1:1.7 also exhibits the predominant tetragonal peaks associated to perovskite structure at (110), (220) and (310), with and without thermal annealing. Annealing for 30 min on the one hand improves film crystallinity with increasing peak intensity. On the other hand, it results in the realigning of crystal domains and/or deteriorating of the crystallinity, indicated by a small PbI_2 peak at 12.65° and the new diffraction peaks which possibly correspond to the tetragonal phase of perovskite films as mentioned before.[20] These additional peaks become more pronounced upon further increasing of annealing time.

Further addition of excessive amounts of MAI up to the AMR of 1:3.5 (PbI_2 to MAI) as shown in Figure 5d, generates a greater number of diffraction peaks in comparison to situations with less organic content as depicted by Figures 5b and 5c. Longer periods of thermal-annealing facilitate the crystallisation and proper orientation of the perovskite films in this case where the number of the peaks has been reduced due to preferred orientation of crystal domains. However, films formed with this composition are unable to achieve a high quality orientation completely in comparison to compositions with relatively less organic content (Figure 5.2b and 5.2c). This is presumably due to the additional phase remaining trapped within the film.

It is worth noting, that the $CH_3NH_3PbI_3$ perovskite crystals are in a tetragonal phase for all composition ranges at room temperature. However, their preferred orientation varies depending on precursor composition and thermal annealing. As a highly

oriented perovskite film shows fewer number of peaks associated more closely with a cubic symmetry[20], due mainly to the strong c-axis orientation, XRD only detects a few of reflections belonging to the tetragonal phase. Any disturbance in such an alignment could lead to the detection of the other x-ray diffraction peaks, which may go undetected otherwise.

All things considered, with regards to the SVD fabrication, identifying the appropriate composition between the inorganic and organic precursors is deemed beneficial to the film formation, especially, since excess of either organic or inorganic content, introduces impurities into the system. Additionally, even though the thermal-annealing processing helps to fully crystallise the perovskite crystal, further-annealing tends to result in the thermal degradation of perovskite films and distortion in crystal structure which may create trap states within the film. Therefore, carefully handling the trade-off between compositions and annealing conditions is a key factor for obtaining the desired high purity crystalline perovskite films. According to the analysis above, the perovskite film with the AMR of 1:1 presented a relatively high crystallinity.

5.3.2 Comparison of Two-Layer Sequential Vapour Deposition and Dual-Source Vapour Deposition

The optimal $CH_3NH_3PbI_3$ perovskite film derived from the DSVD method employed the AMR of 1:1.1 for PbI_2 to MAI. The optimisation process and optimal parameters of the DSVD for fabricating the perovskite film have been stated in section 5.2.2 and summarised in Table 5.3 respectively. The influence on the crystallographic property of the optimal films under various annealing times is depicted by the XRD spectra in

Figure 5.3. Similar to the SVD technique, the DSVD method also produces perovskite films with the predominant tetragonal peaks at 14.13°, 28.49° and 43.27°. A small indication of PbI_2 at 12.65^o existing in the perovskite films without thermal-annealing was observed. Upon increasing the annealing time to 30 min, the PbI_2 peak vanished, while the predominant tetragonal peaks become stronger. This suggests that PbI_2 is fully converted into perovskite by thermal-annealing in the DSVD fabrication. This is unlike the SVD process where the PbI_2 completely reacts with the MAI before annealing. Long annealing time of 120 min generates multiple peaks possibly associated to the tetragonal phase defined by Baikie *et al* that appears in the XRD spectrum.[20] As discussed previously, the appearance of the multiple peaks could be due to the formation of tetragonal domains, which certainly requires further investigation.

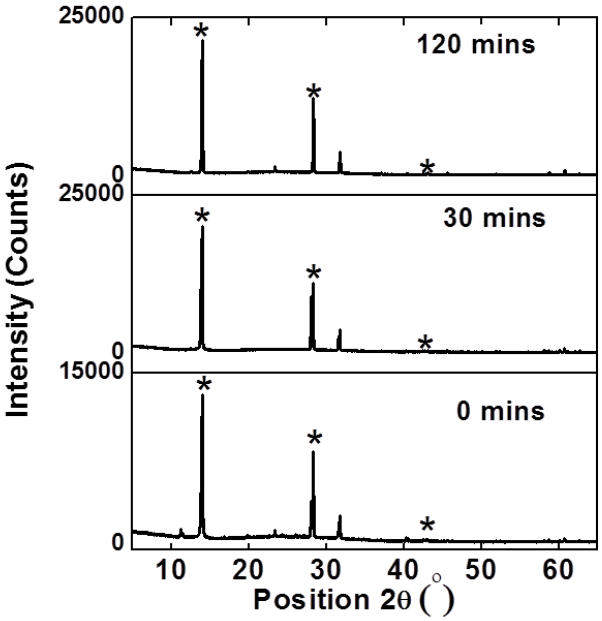


Figure 5.3: X-ray diffraction of the dual-source vapour deposited perovskite films at the optimal composition of 1:1.1 approximate molar ratio

5.3.1.1 Photo-physical Properties

In order to further understand the effects on the photo-physical properties for different annealing times, steady state and time-resolved PL measurements for the perovskite films fabricated by the two vapour deposition techniques at their optimal compositions were performed as shown in Figure 5.4. The perovskite films were fabricated on a glass substrate and a layer of PMMA polymer dissolved in chlorobenzene was spin coated on top to prevent exposure to humidity. The PL emission peak position coincides well at 770 nm for all samples fabricated by both SVD and DSVD techniques, suggesting homogeneity of the probed area of the films.

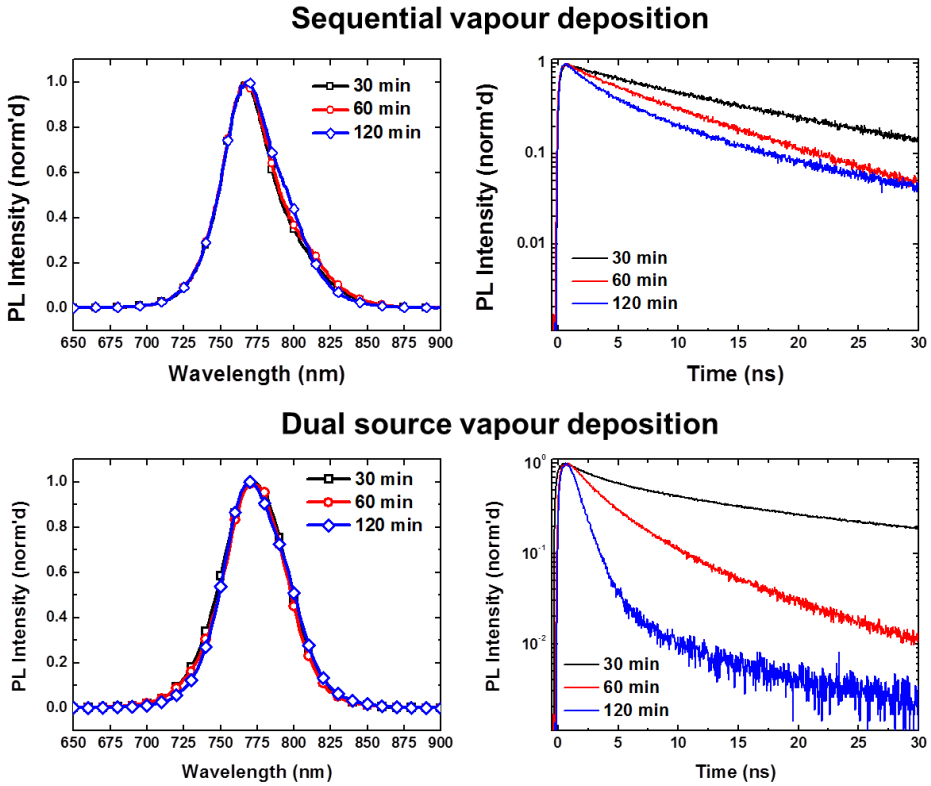


Figure 5.4: Steady state PL and Time-resolved PL. Steady state PL (normalised) of **(a)** a sequential and **(c)** a dual-source vapour deposited films at various annealing time; Time-resolved PL of **(b)** a sequential and **(d)** a dual-source vapour deposited films at various annealing time. Time-resolved PL measurements taken at the peak emission wavelength (770nm) for $CH_3NH_3PbI_3$ perovskite film deposited by SVD and DSVD techniques at 30 min (black), 60 min (red) and 120 min (blue). The data was taken by a pulsed excitation source at wavelength of 507 nm with a fluence of 0.13 μJ/cm^2 impinged on the glass substrate side.

However, in Figure 5.4a, an additional shoulder peak is observed at 800 nm for the SVD fabricated perovskite film annealed for longer periods (i.e. 120 min). This suggests that the divergence of the peaks is possibly related to the two different crystal domains, or perhaps simply due to the different crystal sizes. It could also be due to an additional intermediate crystal phase which appears when annealed for such long duration. Baikie *et al* have reported a reversible phase transition between tetragonal to cubic crystal phase at approximately 57^{o}C.[20] A relatively larger band gap (1.43 eV, 867nm) for the tetragonal phase in comparison to the cubic phase (1.3 eV, 954nm), has been derived based on density function theory (DFT).[21] These calculations agree qualitatively with the PL emission spectra above, which show two distinct peaks at 770 and 800 nm for the longer annealed film. Note that DFT calculations typically underestimate the bandgap energy.[22,23] Therefore, the main PL emission peak at 770 nm may correspond to a tetragonal phase whereas the observed shoulder at 800 nm may be indicative of the presence of the cubic phase in the film.[20] However, as discussed for the XRD data shown in Figure 5.3, perovskite films deposited by the SVD show predominantly tetragonal phases. At this stage, the presence of two distinct dissimilar phases in the perovskite films has not been confirmed.

Figure 5.4b and 5.4d show the corresponding time-resolved PL decay for the perovskite films fabricated by the SVD and DSVD techniques annealed at various times. The time-resolved PL spectra were measured at a peak emission of 770 nm at 0.13 μJ/cm² excitation fluence. This clearly shows that PL decay occurs faster as the annealing time is increased for perovskite films prepared by both techniques. Defining Lifetime $\tau_{e,}$ as the time taken to reach 1/e of the initial intensity, the carrier lifetime of the sequential vapour deposited film diminishes from τ_e= 21.8 ns (at 30 min) to τ_e=

10.4 ns (at 120 min), while the perovskite film produced though DSVD method decays even faster from 11.8 ns (at 30 min) to 4.6 ns (at 120 min). The reduction in carrier lifetimes for the longer annealed perovskite films is perhaps due to degradation of films or improperly orientated crystals, or possibly multiple phases formation (i.e., tetragonal and cubic) capable of driving photo-excitation to lower energetic states. The potential separate phase with a relatively lower band gap (especially the additional PL peak at 800 nm as shown in the steady state PL in Figure 5.4a), may allow photo-excited carriers to relax to lower energetic states, forming trap states in the predominant ABX_3 type perovskite phases, hence, promote charge carrier recombination.

The slightly longer lifetime exhibited by the films fabricated by the SVD technique as compared to that derived by the DSVD method is presumably due to the relatively rougher surface (data will be shown later). It has been recognised that a highly roughened interface strengthens internal light scattering by inducing multiple reflections, the larger crystallites and interface area are also beneficial to charge transport.[24,25]

An investigation into the ultraviolet-visible absorption and photoluminescence emission spectrum of the optimal perovskite films fabricated by the two vapour deposition techniques with an annealing time of 30 min is shown in Figure 5.5. The films fabricated by the two vapour deposition techniques (i.e., SVD and DSVD) exhibited identical UV-Vis spectra responses, where the absorption onset has been identified as an edge centred approximately at 755nm (i.e., 1.64eV). Both PL emission peak positions are at 770 nm (i.e., 1.61eV), with very little down-shift as compared to the absorption spectra. Same phenomenon regarding mixed-halide

perovskite fabricated by the DSVD technique was observed in Chapter 4. Such shifts known as Stokes-shifts are commonly present in organic semiconductors, presumably due to the migration of excitations to low-energy sites,[26] or the vibronic relaxation of the perovskite crystal[27].

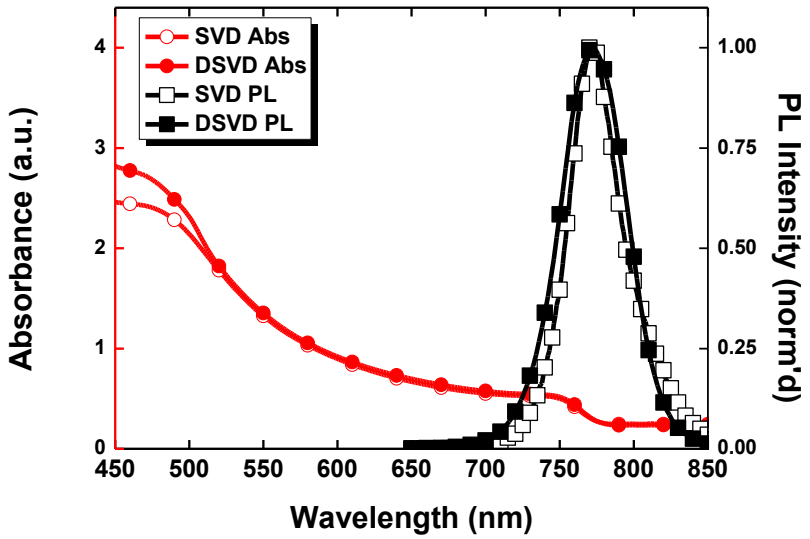


Figure 5.5: Absorption (red) and PL spectra (black). The $CH_3NH_3PbI_3$ perovskite films fabricated by SVD and DSVD methods are represented by open and solid symbols respectively; the perovskite films are coated with PMMA.

According to the discussion above, the optimal films were constructed with an AMR of 1:1 and 1:1.1 (PbI_2 to MAI), for the SVD and DSVD techniques respectively, followed by annealing for 30 min. In the following sections, these optimised films are incorporated into solar cells to evaluate their capability in photovoltaic devices.

5.3.2.2 Microstructural Properties

Figure 5.6 shows scanning electron microscope (SEM) images of the thin-film topology, cross-sectional structure, and film uniformity of the devices constructed by the optimal perovskite films that were fabricated by both SVD and DSVD techniques. The SEM images reveal that there is no significant difference between the

microstructure of the perovskite films deposited by either vapour techniques. The two techniques produce high-quality thin films with full surface coverage and excellent uniformity (i.e.,(300 ±15)nm thickness for the sequential deposited film; (320 ±10)nm thickness for the dual-source deposited film). In addition, atomic force microscopy (AFM) images were used to characterise the roughness of the films that were derived from either technique. The AFM images clearly show that variations in the roughness of the films were slightly larger for those fabricated by SVD (Figure 5.6d) compared to DSVD (Figure 5.6h). Quantitatively, the root mean squared roughness of the perovskite films in Figures 5.6d and 5.6h, for areas of 20 μm × 20 μm were calculated to be 29.78 nm and 23.23 nm respectively. This agrees with previous literature where recorded that solution-based two-step deposition increases the roughness of films.[11,28]

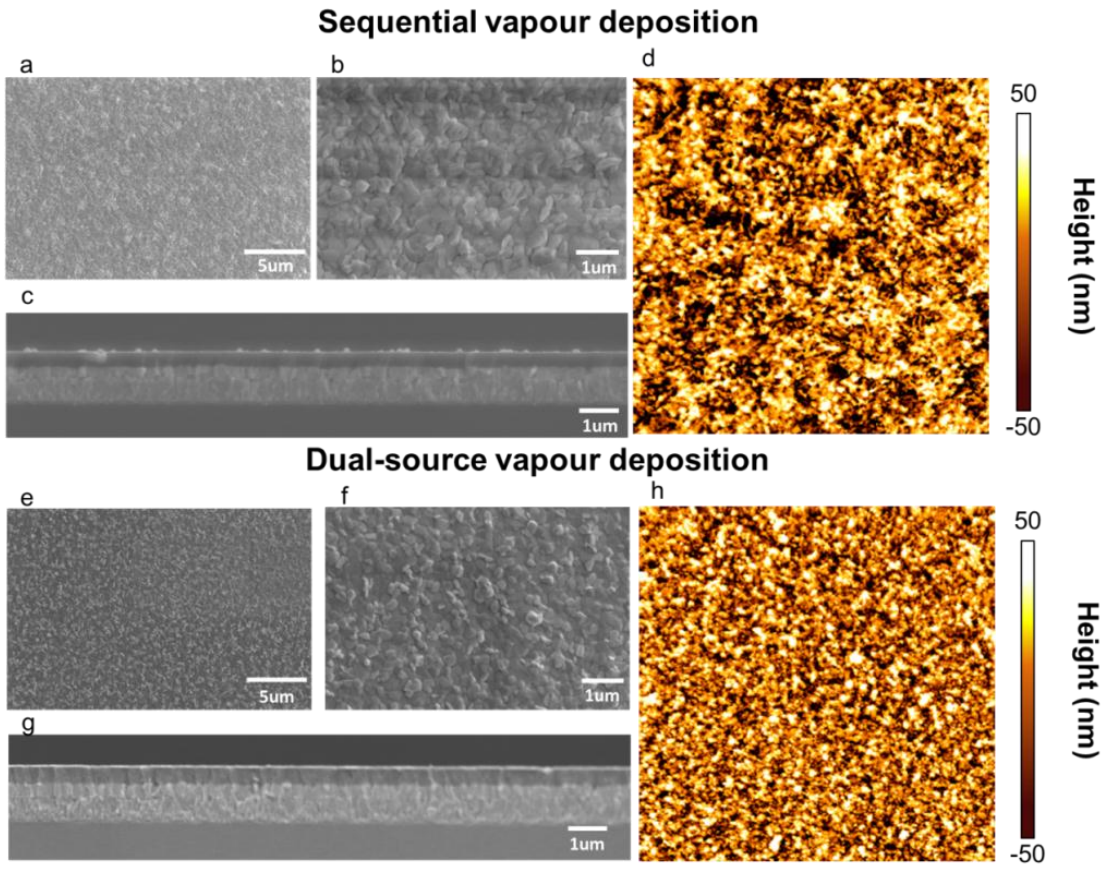


Figure 5.6: Thin-film topology characterisation. Scanning electron microscopy (SEM) top views of **(a)** a sequential and **(b)** a dual-source vapour deposited films; top views under high magnification of **(c)** a sequential and **(d)** a dual-source vapour deposted films; Cross-sectional SEM images under lower magnification of completed solar cells constructed by **(e)** a sequential and **(f)** a dual-source vapour deposited perovskite films; (20 μm x 20 μm) AFM images of perovskite films deposited on a c-TiO_2/FTO substrate derived from **(g)** a sequential and **(h)** a dual-source vapour deposited films.

5.3.2.3 Solar Cell Characterisation

Optimal processing conditions are very critical to the device performance. For example, devices without annealing do not generate any PCEs because of the uncompleted crystallisation. On the other hand, in the case of long annealing, PCEs of devices will be reduced due to deterioration of the crystallinity in the perovskite film as discussed above. Integrating the optimised $CH_3NH_3PbI_3$ perovskite films fabricated by the SVD and DSVD techniques, the J-V curves of the best performing devices

show very similar PCEs both over 15% under simulated AM 1.5 G solar irradiation in air as depicted in Figure 5.7. The SVD technique leads to a device with J_{sc} = 19.87 mA cm^{-2}, V_{oc} = 1V and *FF* = 0.742 yielding a PCE of 15.4%. The optimised performance of the device through the DSVD technique features a J_{sc} of 19.72 mA cm^{-2}, V_{oc} of 1 V, *FF* of 0.746 and therefore a *PCE* of 15.4%. There is a slight trade-off between the J_{sc} and the *FF* of the two devices, with the SVD device exhibiting a slightly larger J_{sc} but smaller *FF*.

In addition, Table 5.4 presents the average and standard deviation of device performance for two batches of cells fabricated by the DSVD and SVD methods respectively, where DSVD technique has less variation in its device performance in comparison to the SVD method. A possible explanation is that different types of reactions occur between the organic and inorganic precursors in the two vapour deposition techniques (i.e., SVD and DSVD). In the process of the SVD fabrication, MAI reacts with PbI_2 by means of inter-diffusion which possibly leads to the inhomogeneous distribution. The size of the perovskite crystals formed by the SVD method may vary from the outer PbI_2 surface where the perovskite crystalline domains are initially formed, to the underlying layer where they are subsequently converted into perovskites by CH_3NH_3I diffusion. This process may produce slight variations in the crystal symmetry and the electronic properties of the films in comparison to perovskite films produced via the DSVD technique. On the other hand, DSVD technique provides a relatively even reaction of the MAI and PbI_2 precursors and therefore results in more stable device performance.

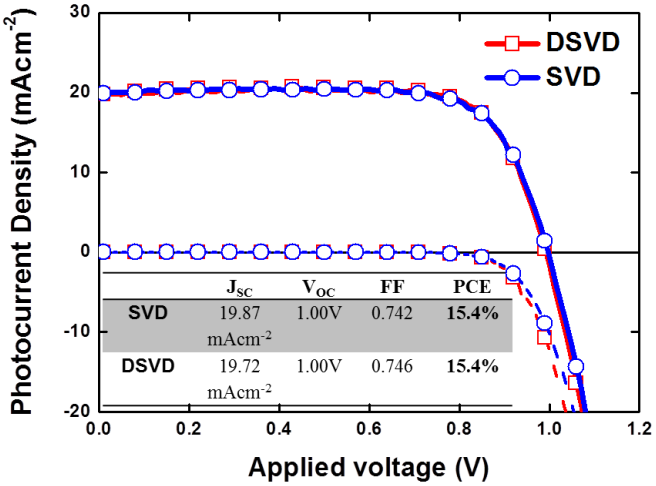


Figure 5.7: Solar cell performance. Photocurrent density-voltage (J-V) curves of the best performing dual-source (red lines, squares) and sequential vapour deposited (blue lines, circles) planar heterojunction triiodide perovskite solar cells. All the devices were measured under simulated AM1.5 sunlight of 95.6 mWcm^{-2} (solid lines) and in the dark (dashed lines).

	J_{sc} (mAcm^{-2})	V_{oc} (V)	FF	PCE (%)
SVD (average ± s.d.)	16.99 ± 2.22	0.98 ± 0.03	0.71 ± 0.02	13.17± 1.37
DSVD (average ± s.d.)	17.77 ± 1.58	0.99± 0.02	0.71 ± 0.02	13.64± 1.13

Table 5.4: Comparison of solar cell performance. Average and standard deviation (s.d) of device performance for two batches of planar heterojunction $CH_3NH_3PbI_3$ perovskite solar cells fabricated by SVD and DSVD respectively. 12 identical cells were included in a batch for each technique.

5.3.2.4 Stability of the Perovskite Film

It has been known that perovskite-type hybrids are easily decomposed in the presence of moisture due to the presence of hygroscopic amine salts. To investigate the influence of the excess of the organic precursor on thermal stability, the optimised perovskite films deposited via the two aforementioned vapour deposition techniques were aged at 80^{o}C in ambient condition. The results were then correlated with the changes in the absorption spectra of the relevant films.

The images and the corresponding UV-Vis spectra were collected at regular time intervals (i.e. 0, 3, 6, 9, 12 and 15 hours). Only the representative UV-Vis diagrams are shown (0h, 6h, 12h &15h) in Figure 5.8. The diagrams demonstrate that films fabricated by SVD and DSVD techniques show a very similar pace of degradation. This similar degradation speed is not surprising, since the amount of organic to inorganic precursors used for the fabrication process was very similar. Both samples remain stable for up to 6 hours of heating at 80^{o}C in air and this is depicted in Figure 5.8a by the retention of the dark colour. Both sets of samples started to degrade after 6 hours, as the edge of the films began to turn yellow. The UV-Vis absorbance spectra of the respective films at the intervals 0, 6, 9, 12 and 15 hrs are shown in Figure 5.8b. Material degradation is indicated by the loss of perovskite absorption features predominantly at ~755 nm. These observations infer that the halide perovskite compound degrades to yellow PbI_2 and other organic constituents. This is consistent with the earlier analysis in the XRD section.

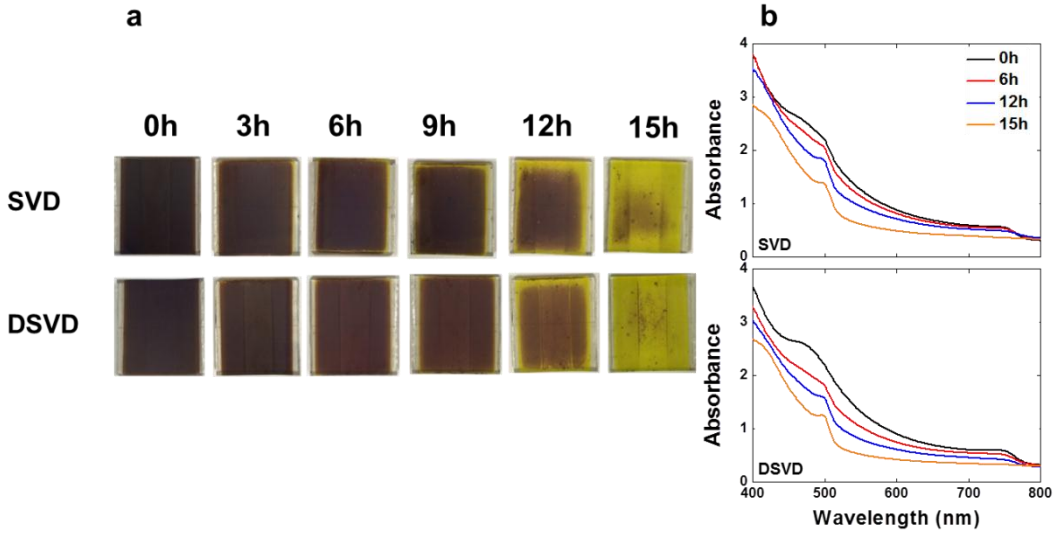


Figure 5.8: Thermal stability in air. (a) Colour change of triiodide perovskite film deposited by SVD and DSVD aging at 80^{o}C in ambient condition. **(b)** Ultraviolet–visible (UV-vis) absorbance spectra of triiodide perovskite film at 0h, 6h, 12h and 15h deposited by SVD and DSVD.

5.4 Conclusion

In this study, SVD technique has demonstrated an alternative vapour deposition technique for fabricating high-efficiency planar heterojunction perovskite solar cells. Both SVD and DSVD techniques have achieved highly performing $CH_3NH_3PbI_3$ perovskite devices with PCEs above 15%. The crystallographic and photo-physical analyses of the perovskite films fabricated by the abovementioned vapour deposition techniques suggested that the fabrication conditions such as the composition of the precursors and the annealing conditions greatly affect the properties of the films.

Regarding the merits shared between the SVD and DSVD methods, although the best performing devices produced by SVD and DSVD methods were equivalent, variation within the DSVD batch was slightly less. On the other hand, from a manufacturing perspective, the SVD is a less complicated technique, offering enhanced control over the reaction between the two precursors, simply by the individual manipulation of the organic and inorganic constituent's deposition parameters. While preparing the work described in this chapter, a similar SVD technique that incorporated with mixed-halide perovskite to fabricate planar heterojunction solar cells was published with a PCE of 15.4%.[29] The expansion of vapour deposition techniques is a step towards the commercialisation of perovskite solar photovoltaic cells.

References

1. Lee, M. M., Teuscher, J., Miyasaka, T., Murakami, T. N. & Snaith, H. J. Efficient Hybrid Solar Cells Based on Meso-Superstructured Organometal Halide Perovskites. *Science* **338,** 643–647 (2012).

2. Kim, H.-S. *et al.* Lead iodide perovskite sensitized all-solid-state submicron thin film mesoscopic solar cell with efficiency exceeding 9%. *Sci. Rep.* **2,** 591 (2012).

3. Grätzel, M. Dye-sensitized solar cells. *J. Photochem. Photobiol. C Photochem. Rev.* **4,** 145–153 (2003).

4. Noh, J. H., Im, S. H., Heo, J. H., Mandal, T. N. & Seok, S. Il. Chemical management for colorful, efficient, and stable inorganic-organic hybrid nanostructured solar cells. *Nano Lett.* **13,** 1764–9 (2013).

5. Heo, J. H. *et al.* Efficient inorganic-organic hybrid heterojunction solar cells containing perovskite compound and polymeric hole conductors. *Nat. Photonics* 1–6 (2013). doi:10.1038/NPHOTON.2013.80

6. Liu, D. & Kelly, T. L. Perovskite solar cells with a planar heterojunction structure prepared using room-temperature solution processing techniques. *Nat. Photonics* **8,** 133–138 (2013).

7. Eperon, G. E., Burlakov, V. M., Docampo, P., Goriely, A. & Snaith, H. J. Morphological Control for high performance, Solution-processed Planar Heterojunction Perovskite Solar Cells. *Adv. Funct. Mater.* **24,** 151–157 (2014).

8. Jeng, J.-Y. *et al.* $CH_3NH_3PbI_3$ perovskite/fullerene planar-heterojunction hybrid solar cells. *Adv. Mater.* **25,** 3727–32 (2013).

9. Docampo, P., Ball, J. M., Darwich, M., Eperon, G. E. & Snaith, H. J. Efficient organometal trihalide perovskite planar-heterojunction solar cells on flexible polymer substrates. *Nat. Commun.* **4,** 2761 (2013).

10. Heo, J. H. *et al.* Efficient inorganic-organic hybrid heterojunction solar cells containing perovskite compound and polymeric hole conductors. *Nat. Photonics* 1–6 (2013). doi:10.1038/NPHOTON.2013.80

11. Burschka, J. *et al.* Sequential deposition as a route to high-performance perovskite-sensitized solar cells. *Nature* **499,** 316–9 (2013).

12. Yella, A., Heiniger, L.-P., Gao, P., Nazeeruddin, M. K. & Grätzel, M. Nanocrystalline Rutile Electron Extraction Layer Enables Low-Temperature Solution Processed Perovskite Photovoltaics with 13.7% Efficiency. *Nano Lett.* **14,** 2591–6 (2014).

13. Sun, S. *et al.* The origin of high efficiency in low-temperature solution-processable bilayer organometal halide hybrid solar cells. *Energy Environ. Sci.* **7,** 399 (2014).

14. Xiao, Z. *et al.* Efficient, high yield perovskite photovoltaic devices grown by interdiffusion of solution-processed precursor stacking layers. *Energy Environ. Sci.* **7,** 2619 (2014).

15. Cheng, Z. & Lin, J. Layered organic–inorganic hybrid perovskites: structure, optical properties, film preparation, patterning and templating engineering. *CrystEngComm* **12,** 2646 (2010).

16. Shah, a. V. *et al.* Thin-film silicon solar cell technology. *Prog. Photovoltaics Res. Appl.* **12,** 113–142 (2004).

17. Ramanathan, K. *et al.* Properties of 19.2% efficiency ZnO/CdS/$CuInGaSe_2$ thin-film solar cells. *Prog. Photovoltaics Res. Appl.* **11,** 225–230 (2003).

18. Hu, H. *et al.* Vapour-based processing of hole-conductor-free $CH_3NH_3PbI_3$ perovskite/C60 fullerene planar solar cells. *RSC Adv.* **4,** 28964 (2014).

19. Kojima, A., Teshima, K., Shirai, Y. & Miyasaka, T. Organometal halide perovskites as visible-light sensitizers for photovoltaic cells. *J. Am. Chem. Soc.* **131,** 6050–6051 (2009).

20. Baikie, T. *et al.* Synthesis and crystal chemistry of the hybrid perovskite $(CH_3NH_3)PbI_3$ for solid-state sensitised solar cell applications. *J. Mater. Chem. A* **1,** 5628 (2013).

21. Perdew, J. P., Burke, K. & Ernzerhof, M. Generalized Gradient Approximation Made Simple. *Phys. Rev. Lett.* **77,** 3865–3868 (1996).

22. Walle, C. G. V. de & Neugebauer, J. *Advanced Calculations for Defects in Materials: Electronic Structure Methods*. 402 (John Wiley & Sons, 2011).

23. Mosconi, E., Amat, A., Nazeeruddin, M. K., Grätzel, M. & De Angelis, F. First Principles Modeling of Mixed Halide Organometal Perovskites for Photovoltaic Applications. *J. Phys. Chem. C* (2013). doi:10.1021/jp4048659

24. Li, G. *et al.* High-efficiency solution processable polymer photovoltaic cells by self-organization of polymer blends. *Nat. Mater.* **4,** 864–868 (2005).

25. Zheng, L. *et al.* Improved light absorption and charge transport for perovskite solar cells with rough interfaces by sequential deposition. *Nanoscale* **6,** 8171–6 (2014).

26. Bässler, H. & Schweitzer, B. Site-Selective Fluorescence Spectroscopy of Conjugated Polymers and Oligomers. *Acc. Chem. Res.* **32,** 173–182 (1999).

27. Lakowicz, J. R. *Principles of Fluorescence Spectroscopy*. 980 (Springer Science & Business Media, 2007).

28. Liang, K., Mitzi, D. B. & Prikas, M. T. Synthesis and Characterization of Organic-Inorganic Perovskite Thin Films Prepared Using a Versatile Two-Step Dipping Technique. *Chem. Mater*. 403–411 (1997).

29. Chen, C.-W. *et al.* Efficient and Uniform Planar-Type Perovskite Solar Cells by Simple Sequential Vacuum Deposition. *Adv. Mater.* (2014). doi:10.1002/adma.201402461

Chapter 6

Understanding on Hysteresis in Perovskite Solar Cells through Titania Compact-Free System

Content and Summary

The performance of hybrid organic-inorganic perovskite solar cells has been rapidly enhanced over the past two years.[1,2,3,4,5] Nevertheless, anomalous hysteresis has been commonly observed in perovskite-based devices.[6,7,8] To understand and compare the hysteretic behaviour in the meso-superstructured and planar heterojunction perovskite solar cells, a solution processing route (spin-coating) was adopted for fabricating the perovskite solar cells in this specific study, since vapour deposition methods restrict the optimisation of meso-superstructured perovskite solar cells into functional devices.

This chapter commences with an evaluation of the hysteretic behaviour of the devices while in different configurations. Interestingly, observations in this chapter show that planar and meso-superstructured perovskite solar cells can be fabricated completely

free of a hole-blocking layer with high PCEs. However, the PCEs obtained from current-voltage scans could not be maintained whilst holding the cells at the maximum power point. Rather, they appeared to be ‘transient efficiencies’ induced by factors related to the previously observed hysteresis. This work suggests that polarisation of the perovskite diode under forward bias results in effective *n*-type doping of the perovskite near the anode, and *p*-type doping of the perovskite near the cathode; which is essential for charge extraction at the junctions. This facilitates the migration and accumulation of ions within the perovskite to the metallic contacts. Reducing the external field under working conditions however, results in the ions migrating slowly away from the junctions. Therefore, the interface doping and effectiveness of the operation of the devices are weakened. This chapter aims to discuss this hysteretic behaviour in relation to the device performance of perovskite cells in detail.

6.1 Introduction

Research into organic-inorganic metal halide perovskite solar cells has swiftly gained momentum. High-efficiency perovskite solar cells have been demonstrated by both thin film and mesoporous device architectures.[1,2,3,4,5] Regarding the standard architecture for solution-processed perovskite solar cells, a typical mesoporous device is constructed of a TiO_2 or Al_2O_3 mesoporous layer infiltrated with perovskite which is sandwiched between an electron-selective contact compact layer and a HTM.[1,2] On the other hand, planar heterojunction devices exclude the mesoporous layer.[9] For these high-efficiency perovskite devices, a compact layer (mostly titania TiO_2) sintered at high temperatures is always employed in order to extract electrons at the anode, a fabrication procedure that evolved from previous research on DSSCs.[2] In addition, several approaches have recently been employed to enable the low-temperature fabrication of relatively efficient devices.[9,10,11,12]

Nonetheless, hysteretic effects have been commonly observed in perovskite-based devices.[6,7,13] In the case of conventional PV technologies such as CIGS, CdTe, and amorphous silicon, the hysteretic phenomenon is introduced by the high internal capacitances, which have been caused by charge carrier accumulation in the depletion layer or neutral region of the junction.[6,14,15] Under fast forward bias to short circuit (FB-SC) scanning condition, the solar cell tends to charge up in forward bias mode. When the solar device is quickly scanned under FB-SC condition, both the photo-generated charges and the extra-capacitive charges can be extracted. On the other hand, rapidly sweeping from short circuit to forward bias (SC-FB) can result in the photo-generated charges partially charging the devices. As a result, the net charge flowing into the external circuit is decreased. However, in the case of the

perovskite-based solar cells, contrary to the typical expectations from capacitive charging and discharging, there can still be significant hysteresis even at extremely slow scan rates.[6] It suggests that the hysteresis in the perovskite-based devices could also be attributed to factors such as the trapping/de-trapping of charge carriers,[6,16] ferroelectricity,[6,13,17,18,19] and ion migration.[6,13,20,21]

Since the efficiency values of perovskite devices obtained for different scan rates and directions are possibly undervalued or overestimated due to the hysteretic effects, a number of recent observations indicate that the measuring protocol and light exposure history alter the photovoltaic behaviour, the shape of the current-voltage curve, and hence the derived PCEs for perovskite solar cells.[5,6,7,8] It has been suggested that the stabilised maximum power output is a critical parameter for fully evaluating device performance.[6]

In this chapter, the hysteretic performance of perovskite solar cells in various configurations is discussed. Counter intuitively, it was observed that planar heterojunction and mesoporous Al_2O_3 devices completely free of TiO_2 compact layer (hereafter refer TiO_2 compact layer to as Ti-CL) momentarily exhibited PCEs of 11.0% and 13.2% respectively, under relatively slow scan rates (0.38V/s) with substantial hysteresis in the J-V curve. To understand the possibility and impact of fabricating solution-processed perovskite solar cells entirely free of *n*-type charge selective TiO_2 compact layers, a detailed study aimed at probing the stabilised PCE of the devices was conducted by subjecting them to a constant voltage near the maximum power point of the J-V curve. The results showed that the devices stabilise at a much lower PCE than their apparent initially PCE. The contradictions between the temporary photovoltaic behaviour obtained from current-voltage scans and the stabilised power output suggest that a slowly changing temporary field is established during forward

biasing. This temporary field could be due to an intrinsic defect or related to photo/electric stimulations, resulting in the observed hysteretic behaviour.

6.2 Methods

This section focusses particularly on the fabrication methods for compact-free devices, and the relevant FTPS measurements using the FTIR setup. All other fabrication processes and characterisation techniques have been discussed in Chapter 3.

6.2.1 Substrate Preparation and Synthesis of Precursors

The synthesis of the perovskite $CH_3NH_3PbI_{3-x}Cl_x$ solution precursor (40 wt% DMF solution of CH_3NH_3I and $PbCl_2$ at 3:1 molar ratio) has been described in section 3.1, and the preparation of FTO substrates followed the procedures as described in section 3.2.1.

6.2.2 Fabrication of Standard Meso-Superstructured and Planar Heterojunction Perovskite Devices

Methods for fabricating meso-superstructured and planar heterojunction perovskite solar cells in a glovebox through solution-based processes have been described respectively in sections 3.2.2.1 and 3.2.3.1.

6.2.3 Compact-Free Device Fabrication

All Ti CL-free devices were constructed following the standard architecture with the exclusion of *n*-type compact layers (i.e., FTO (/mesoporous Al_2O_3) /perovskite/HTM/Ag), the entire process was performed in a nitrogen-filled glovebox. For the Ti CL-free planar heterojunction devices (FTO/perovskite/HTM/Ag), the cleaned FTO-coated substrates were heated up to 80^oC prior to spinning the perovskite precursor. Note that the spin-coating process was immediately carried out

on the heated substrate at 2000 r.p.m for 45s. For the Ti CL-free meso-superstructured devices (FTO/mesoporous Al_2O_3/perovskite/HTM/Ag), the fabrication of the mesoporous Al_2O_3 layer was similar to the standard meso-superstructured devices as described in Section 3.2.2.1. The perovskite precursor was then spin-coated on top of the mesoporous layer of Al_2O_3 at 2000 r.p.m for 45 s.

6.2.4 Hole-Transporter Deposition and Electrode Deposition

Fabrication procedures of the HTM and metal electrode have been described in section 3.2.4.

6.2.5 Fourier Transform Photocurrent Spectroscopy (FTPS)

The FTPS measurement was aimed at investigating the influence on incident photon-to-current efficiency (IPCE) spectra by varying bias values, under forward and reverse scan directions. More information of how to measure IPCE spectrum of a device has been described in section 3.3.3.3.

Figure 6.1 illustrates and the experimental design and the methodology. By applying a voltage to polarise the devices for a certain duration of time under illumination, an IPCE spectrum of the devices was measured immediately after the devices were short-circuited. The samples were charged firstly in the direction of forward bias and then in reverse bias. Upon recording all IPCE spectra for the corresponding bias values, the mathematical integration of the results of the IPCE spectra were plotted as a function of the applied bias. The integration of the IPCE spectra is equivalent to the photocurrent at the corresponding applied bias.

In this experiment, the period for each bias charging cycle of the devices was set to 20s, while the upper limits of forward bias and reverse bias were at 2 V and -2 V respectively. Each increment (or decrement) of the bias voltage was applied at an

interval of 0.05 V for a corresponding IPCE spectrum. Basically, the integration of the IPCE values was plotted within the range of 2 V to -2 V at intervals of 0.05 V.

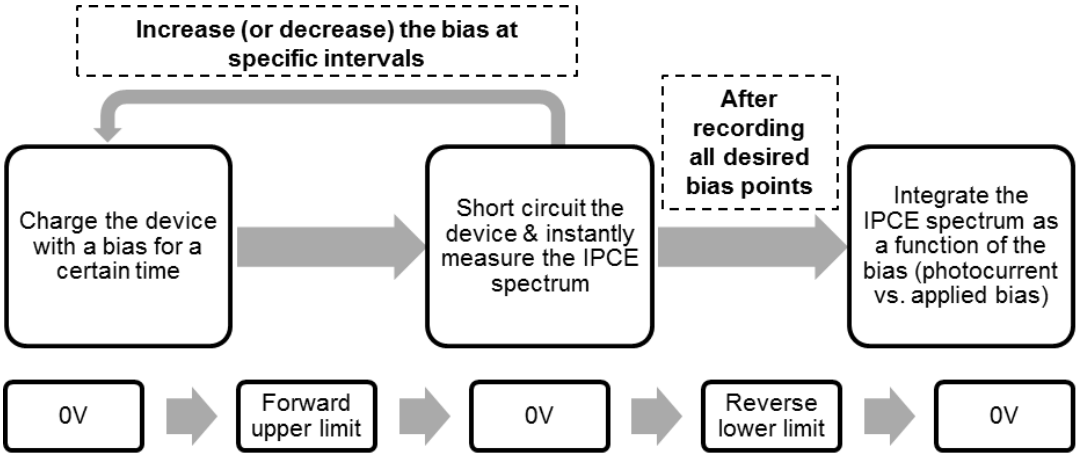


Figure 6.1: FTPS experiment design

6.3 Results and Discussion

6.3.1 Device Configuration

Planar heterojunction and meso-superstructured mixed-halide perovskite solar cells with/without a titania compact layer and/or hole-transporting layer, were fabricated in this work.

Figure 6.2 illustrates that the perovskite, optionally incorporated within an alumina scaffold, was sandwiched between fluorine-doped tin oxide (FTO) - with or without a titania compact layer coated upon it, and with a HTM, spiro-OMeTAD. As has been confirmed by previous work in Chapter 4, such spin-coated planar films typically comprise of well crystallised domains which feature an undulating surface morphology (Figure 6.2b and 6.2d), with an average thickness of 300-500 nm.[22] Utilising the conventional TiO_2 compact layer (Ti-CL), leads to the formation of better planar films in comparison to simply coating the perovskite onto FTO-coated substrates.[23] Thus, the uneven distribution of the perovskite's thickness on FTO could

be detrimental to the performance of the devices, due to shunting paths between the HTM and conductive substrate. Inserting a mesoporous Al_2O_3 layer in between the FTO and HTM results in a much more controllable film with a uniform thickness of approximately 500 nm (Figure 6.2f and h). Note that in these devices an obvious capping layer of perovskite is formed on top of the alumina mesoporous layer that is infiltrated within the perovskite.

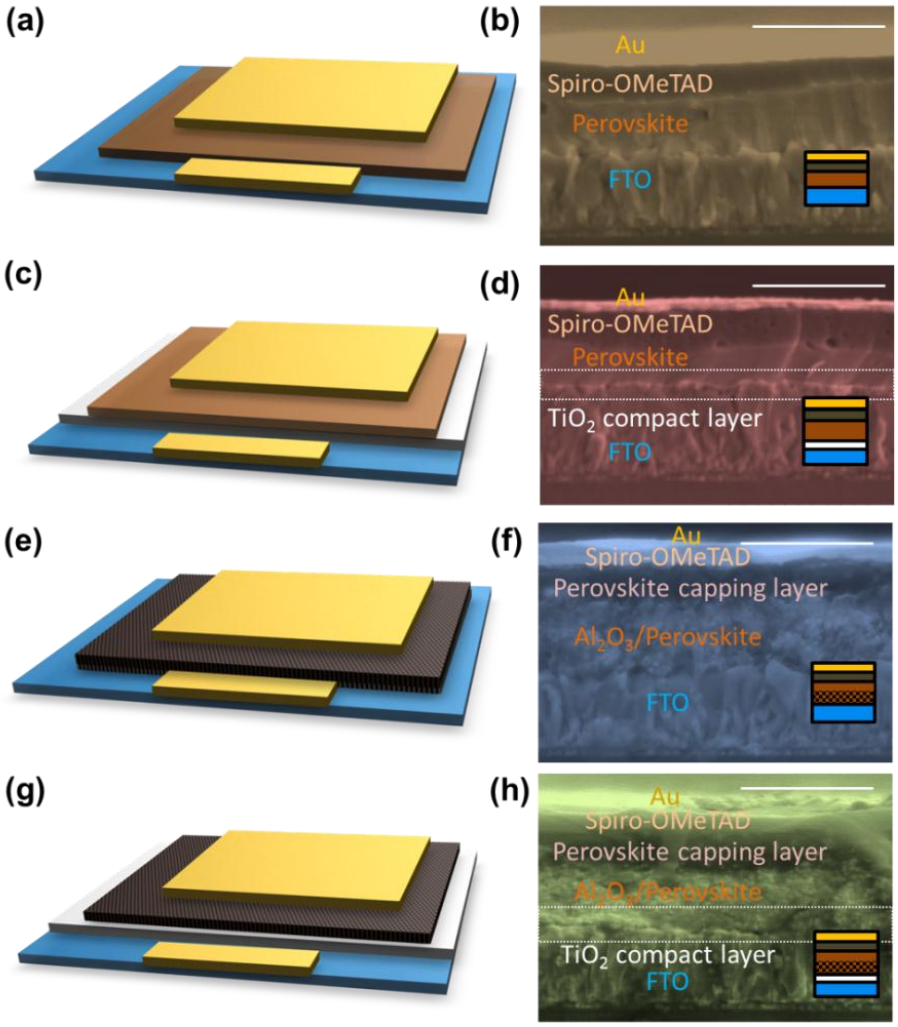


Figure 6.2: Schematic illustrations (Left) and SEM images (Right) of mixed halide perovskite solar cells with or without Ti-compact layer. **(a) (b)** Planar structure without a titania compact layer; **(c) (d)** Planar structure with a titania compact layer **(e) (f)** Mesoporous structure on an Al_2O_3 scaffold without a titania compact layer; **(g)(h)** Mesoporous structure on an Al_2O_3 scaffold with a titania compact layer. Dashed white boxes in **(d)** and **(h)** enclose the Ti-CL. The diagrams indicate cross-sections of each device.

6.3.2 Device Performance and Hysteretic Behaviour

Different device configurations would generally give rise to variance in terms of interfacial contacts of FTO/active layer, active layer/HTM, HTM/Au interface due to film formation, coverage, and more importantly, defect distribution.[24,25,26,27] The performance of solution-processed planar heterojunction devices is generally considered to be substantially more sensitive in comparison to their mesoporous counterparts with regards to humidity, atmosphere, ambient temperature, substrate texture, and other processing parameters.[22,28]

The devices were initially examined with or without a Ti-CL, but always including an HTM layer (spiro-OMeTAD). The solar cell performances of the best devices fabricated for each architecture are shown in Figure 6.3, and the parameters used for the evaluation of device performance are summarised in Table 6.1.

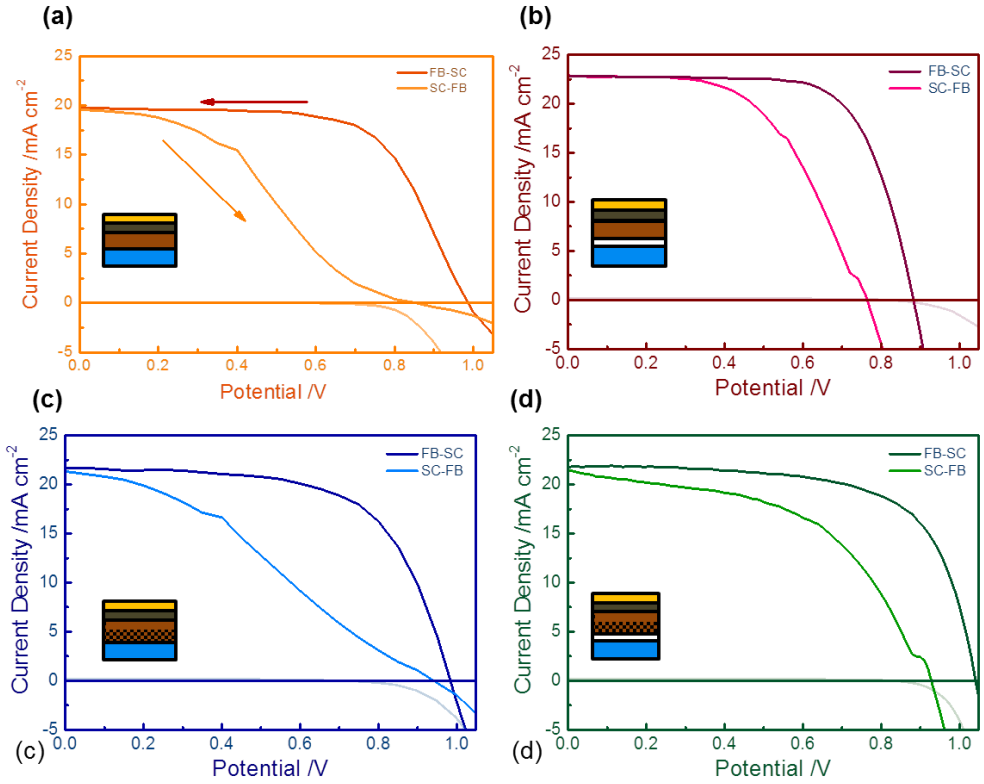


Figure 6.3: Forwards and backwards J-V curves of perovskite solar cells with different structures under simulated AM1.5, 100 mW cm^{-2} solar irradiation of the best performing solar cells. Devices are scanned at 0.38V/s after holding at 1.4V under illumination for 5 seconds. FB-SC refers to forward bias to short circuit; SC-FB is vice versa. **(a)** Planar structure without a titania compact layer **(b)** planar structure with a titania compact layer. **(c)** Mesoporous structure on a Al_2O_3 scaffold without a titania compact layer **(d)** mesoporous structure on a Al_2O_3 scaffold with a titania compact layer. Corresponding dark currents are plotted underneath the *x*-axis. The arrows indicate the scan directions, which represent the photovoltaic behaviour measurement throughout this work. The inserted diagrams indicate cross-sections of each device configuration.

In the planar architecture, upon removal of the Ti-CL, a PCE of 11.5% was obtained yielding a J_{sc} of 19.5 mA cm^{-2} and a V_{oc} of 0.95 V under FB-SC scan. Notably, two weeks after taking the initial measurements, the device showed no observable sign of degradation, delivering an even higher *PCE* of 12.3% (data not shown here). Reversing the scan under SC-FB condition caused a considerable drop in V_{oc} and *FF*, due to the hysteresis of the device. On the other hand, inserting the Ti-CL between the active perovskite layer and underlying FTO substrate as the standard planar configuration, the optimal planar heterojunction device reached a *PCE* of 14.2%, with

a J_{sc} of 22.8 mA cm^{-2}, V_{oc} of 0.88 V, and *FF* of 0.7 during the FB-SC scan. This shows a significant improvement in the *FF* from 0.62 to 0.70 by inserting the Ti-CL, implying that these devices exhibit more efficient charge extraction, less recombination, or smaller resistances at the contacts. However, it is interesting that a device without the Ti-CL still produces good PCE under fast J-V scan. Assuming carrier recombination at the FTO-perovskite interface was critical, much lower values of V_{oc} and *FF* would have been obtained in the situation without a Ti-CL. The V_{oc} in fact, *increases*, most likely because electrons do not have to be transported through the TiO_2 compact layer, which is characterised by a high density of sub gap states limiting the electrons Fermi level, and thus resulting in a drop in voltage due to the incurred energy loss.

Regarding the standard configuration of the meso-superstructured devices with a Ti-CL and mesoporous Al_2O_3 scaffold layer, slightly better repeatability of results was observed as well as less variations of PCE statistical data within-batches for different batches produced. An optimal meso-superstructured device with Ti-CL contributed a PCE of over 15% featuring a J_{sc} of 21.8 mA cm^{-2}, a V_{oc} of 1.04 V, and a *FF* of 0.66 in the FB-SC scan. Notably, the removal of the Ti-CL only leads to a slight decrease in *FF*, which could be due to contact resistance, or increased recombination between the mesoporous/active layers with the FTO substrate. Moreover, the open-circuit voltages measured for these devices are generally higher than those for devices with planar structures (Table 6.1).[25]

Device structure	Ti-CL/ HTM	Scan direction	J_{sc} (mA cm^{-2})	V_{oc} (V)	FF (%)	Dark current onset (V)	PCE (%)	Stabilised PCE (%)
Planar	no/yes	FB-SC	19.54	0.95	0.62	0.84	11.5	**0**
		SC-FB	19.50	0.80	0.41		6.4	
Planar	yes/yes	FB-SC	22.8	0.88	0.70	1.1	14.2	**9.12**
		SC-FB	22.9	0.76	0.54		9.5	
Meso	no/yes	FB-SC	21.68	1.00	0.62	1.1	13.2	**2.7**
		SC-FB	21.31	0.95	0.33		6.5	
meso	yes/yes	FB-SC	21.79	1.04	0.66	1.05	15.5	**13.5**
		SC-FB	21.47	0.93	0.51		10.6	
planar	no/no	FB-SC	7.11	0.77	0.53	0.7	3.2	**0**
		SC-FB	5.19	0.65	0.21		0.7	
Meso	no/no	FB-SC	18.6	0.80	0.47	0.7	7.1	**0**
		SC-FB	16.62	0.70	0.22		2.6	

Table 6.1: Device performance for fabricated mixed halide perovskite solar cells under different scanning directions. Dark current onsets are extracted from the extrapolation of the dark curves from the FB-SC scans. Stabilised PCEs were obtained from holding voltage scans at maximum power point of each individual cell.

From Figure 6.3 and Table 6.1, it is evident that hysteresis also occurs in standard structures of planar heterojunction and meso-superstructured devices with Ti-CL. Cells fabricated in the absence of a Ti-CL have a worse performance, possibly due to increased or faster recombination at the unblocked metallic contacts. At the aforementioned scan rates, forward scans from SC-FB commonly result in almost identical short-circuit current densities (i.e., J_{sc}), similar to backward scans from FB-SC (See Table 6.1). Alternating between opposite scanning direction seems to only compromise the V_{oc} and *FF*. As has been previously reported by Snaith *et al.*, it is likely that slowing down the scan rate would progressively worsen the hysteresis, until it approaches a point where an unfeasibly slow scan rate gives less hysteresis (and likely worse performance).[6] Notably, this behaviour seems to be heavily dependent on device processing conditions and is expected to vary from lab to lab. It should be emphasised that care must be taken for the scanning conditions to evaluate perovskite solar cells to avoid deceptive photovoltaic performance measurements.

In both planar and meso-superstructured configurations, the dark currents as depicted in Figure 6.3 also demonstrate good rectification behaviour, exhibiting neither

obvious leakage currents nor any significant current at reverse bias. This can be seen as evidence that the hysteretic effect is not due to a capacitive current.[29,30] Furthermore, the meso Ti-CL-free sample displays an even later onset. This was quite an unusual observation as without the Ti-CL in system, the photo-generated holes would be unscreened and are expected to be subject to recombination with the electrons immediately before being collected at the electrodes especially since the halide perovskite material is conductive (conductivity on the order of 10^{-3} S cm^{-1}) and assumes the dual role of electron and hole transporter. Therefore, it raises questions regarding whether the Ti-CL functions as is generally conceived, during fast current-voltage scans which is universally employed to determine the PCE of solar PV cells.

6.3.3 Discussion on the Origins of Hysteresis from a Stabilisation Power Perspective

Due to the severe hysteresis observed and the unexpected efficient Ti-CL-free device under fast J-V scan, another method was required to measure the 'real' device performance under working conditions. Therefore, an attempt was made to stabilise these devices at a steady holding voltage, close to the maximum power point, to probe their steady-state output. As shown in Figure 6.4, all cell configurations demonstrate a reduced stabilised power output value compared to their fast J-V scan value, with the most drastic decrease exhibited by the Ti-CL-free samples. The standard mesoporous samples stabilise at close to the PCE value given by the J-V scan at 13.5%, while the Ti-CL-free mesoporous cells stabilise at a much lower value of 2.7%. The Ti-CL-free planar cells generate almost zero current density and hence zero PCE, when subjected to a prolonged hold time.

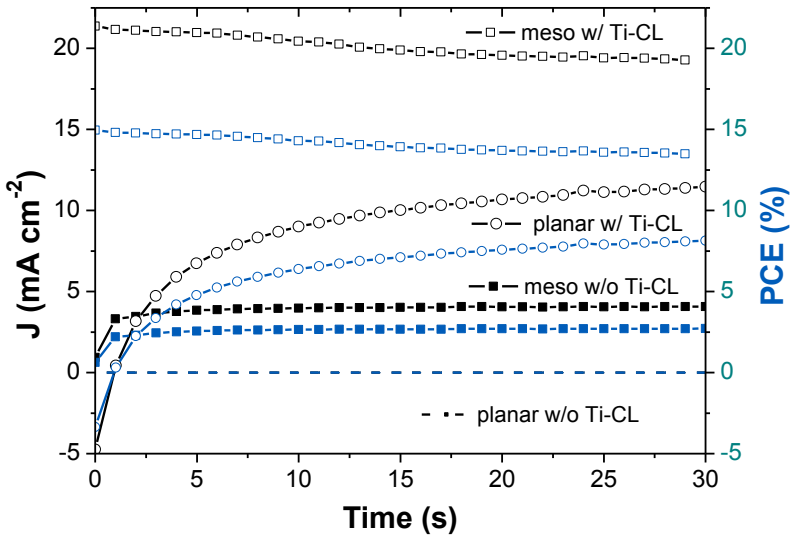


Figure 6.4: Stabilised maximum power output PCE data (blue) and current profile (black) of perovskite solar cells with and without Ti-CL. Dashed lines indicate Ti-CL free planar samples; hollow square symbols indicate standard mesoporous samples; solid square symbols indicated mesoporous samples without Ti-CL; hollow circular symbols indicate planar samples with Ti-CL. Note all the devices investigated here were fabricated with the HTM layer.

Two interesting observations have been extracted from this set of data. Firstly, it is apparent that a short-lived effect is beneficial during FB-SC scans but adverse during the SC-FB scans for the PCE values. This effect tends to disappear during the stabilised power scan and it is responsible for hysteresis in these devices. The stabilised output of the cells with Ti-CL is not critically affected, though the presence of Ti-CL does lead to temporarily enhance the PCE during FB-SC fast scan in comparison to the stabilised output while holding the bias at the maximum power point. In contrast, regarding the devices without Ti-CL, the stabilised output is dramatically diminished in comparison to the fast scan PCE. These observations therefore suggest that the short-lived beneficial effect is responsible for enabling temporarily functional devices without Ti-CL. However, since performance degrades during a stabilisation scan, these devices suffer low stabilised 'real' PCEs (approaching zero in the case of the planar

structure), as a result, it is not feasible to produce Ti-CL free devices with high real PCEs.

Secondly, it has been shown that the Ti-CL MSSCs are able to generate some power output while holding the bias at the maximum power points, but the Ti-CL free planar devices are unable to produce any stabilisation power. These evidences emphasise the importance of the alumina mesoporous layer which does not solely contribute to film formation. As was previously suggested, the perovskite permeated within the mesostructure is likely to be *n*-doped, while the capping layer, or planar perovskite, is almost intrinsic.[25] As such, the mesostructured cells with no Ti-CL would actually possess an *n-i-p* structure, despite the absence of a material-based *n*-dopant for the perovskite material, thereby establishing a permanent built-in-field within the device, which would be able to extract charges while maintaining the bias at the maximum power point. The potential for Ti-CL free planar cells to operate with an *n-i-p* structure is clearly restricted by the field generated at the HTM interface which is not enough to extract charges over the long term, or the recombination of carriers at the FTO-intrinsic perovskite interface which also compromises the device performance.

This suggests that the temporary built-in-field, which induces the observed hysteresis, may be present when the cell is charged at forward bias before scanning. This field is expected to be in the direction favourable to charge extraction, and to possibly temporarily enhance the efficient extraction of charges while preventing recombination at the contacts. On the subject of cells with Ti-CL, this field boosts their efficiency temporarily, leading to the improved 'fast scan' efficiencies. The stabilised PCE in this case is only slightly lower because the presence of selective contacts prevents recombination at the contacts. Regarding the Ti-CL-free planar devices, which have no built-in-field of their own, the temporary field only enables them to function initially.

Whereas for the Ti-CL free mesostructured devices, where the (presumably relatively small) built-in field is due to the *n*-doped perovskite being infiltrated within the alumina, the temporary field initially enables them to function *adequately*, before it dissipates - causing the cells to operate in a much less efficient manner (Figure 6.5). This short-lived effect is found to be related to forward-biasing and illumination (light soaking). On the other hand, the standard cells with Ti-CL have shown relatively small discrepancies between their and 'real' and 'apparent' PCEs, possibly due to their large dielectric constant approaching 80.[31,32]

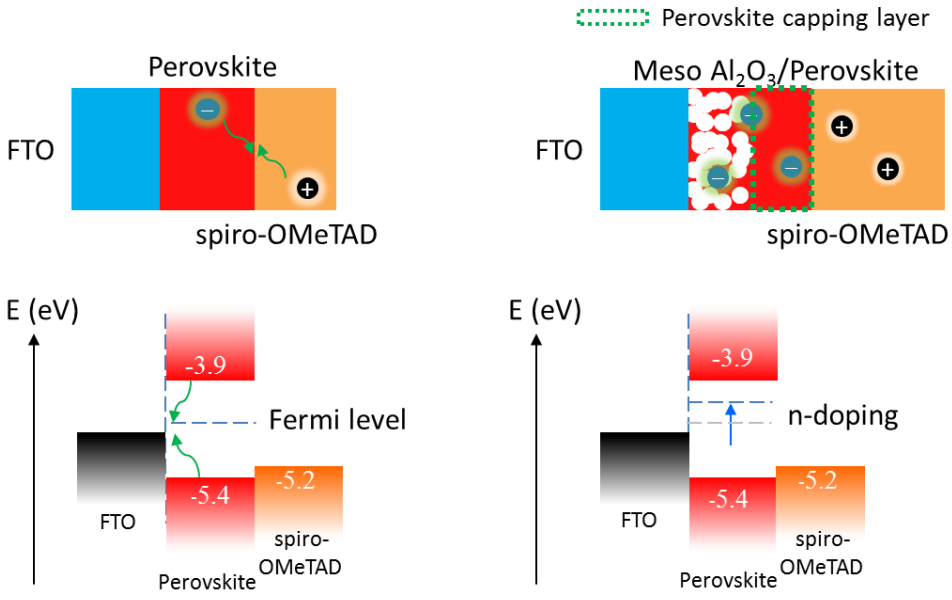


Figure 6.5: Schematic representation of the intrinsic doping of perovskite material induced by alumina mesoporous scaffold.

Interestingly, the maximum power output is dependent on the thickness of the Ti-CL. By varying the concentration of the Ti-CL solution, an optimal condition where the stabilised PCE is maximised, can be achieved as shown in Figure 6.6. In fact, devices employing a mesoporous titania scaffold may not even show any observable hysteresis.[5] This could be as a result of the TiO_2 compact layer screening some of the field due to its high dielectric constant, during forward biasing of the cells. Thereby,

enabling the perovskite layer to experience less of the field than it would in the absence of a compact layer. However, this should be distinguished from charging/discharging a capacitor, because no observable capacitive current was detected from the current-voltage scans run in the dark.

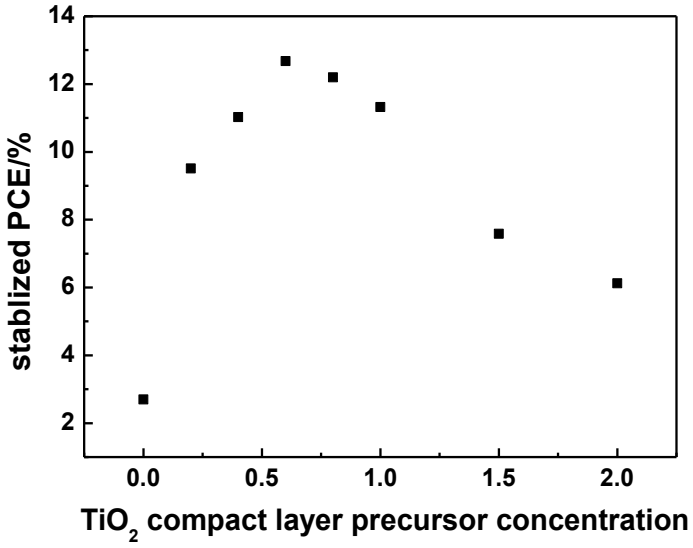


Figure 6.6: Optimisation of stabilised power output by varying the titania precursor concentrations for meso-superstructured perovskite solar cells

The precise nature of this temporary built-in field is still unknown. A possible explanation is that it is due to mobile defects in the perovskite material. During the initial fabrication process, excess organic component is utilised in order to ensure the stoichiometric crystal phase formation.[1] In the course of the subsequent annealing process (typically 80-120^{o}C), it seems likely that an abundance of various point defects, dangling bonds, or stack faults, within the bulk of the material and grain boundaries were induced by uneven solvent evaporation and possibly ion migration across the film. These defects can be categorised into Schottky defects, i.e., neutral vacancy pairs, and Frenkel defects, which are defined by ionic species, such as vacancies (V_{Pb}, V_I, V_{MA}), interstitials (Ma_i, Pb_i, I_i), or substitutions (MA_{Pb}, Pb_{MA}, M_{AI}, Pb_I, bI_{MA}, I_{PB}) amongst others. It has been proposed that the formation energy of such defects are below 100

meV, in relation to the chemical potential of each component.[33] This activation energy required to separate bound electron-hole pairs is thus of a similar order to the thermal energy, kT (~25.6 meV). These low formation energies could result in shallow levels, which can be partially attributed to the strong Pb lone-pair *s* orbital and I (iodine) *p* orbital antibonding coupling.[34] The extremely high dielectric constants (including their illumination dependence) and slow dynamic processes recently reported for this material[7,35] could be induced by the intrinsic defects discussed above.

When constructed onto a mesoporous scaffold, the perovskite material tends to be confined within the network featuring a crystal diameter of ~50nm.[3] Smaller nanocrystals indicate a large amount of grain boundaries and preferential crystal orientations, which is likely to influence defect formation. Their unique ionic bonding nature suggests that the defects can easily be activated by applying an external bias, or by subjecting the material to illumination at room temperature.[36] During current-voltages scans, the highly responsive charged defects could become mobilised, drifting towards the external collectors, thus, removing the defects from the bulk and creating a beneficial built-in field, explaining the short-time beneficial effect (Figure 6.7). There is evidence that a certain period of illumination (photo-doping) or a forward-bias (electric activation) would yield higher PCEs, while prolonged visible light irradiation would yield a plateau, or even a decrease[37] due to possible saturation or depletion of defects. However, the short-lived Frenkel defects could have been neutralised due to charge balance when the external bias was removed, explaining the lower apparent PCEs during slow scans.

Another feasible explanation for the temporary built-in field is that a rearrangement of the cations in the perovskite could occur upon illumination or bias, in a manner similar to the ferroelectric effect.[17] Since the displacement of a cation can cause a dipole

moment, it is possible that such dipole moments slowly align themselves either throughout the film or in specific domains, giving rise to a temporary built-in field, and encouraging charge separation. The observations made based on all the experiments mentioned above, are consistent with either explanation. The cation-realignment theory has been proposed by others already.[7,17,18] Nonetheless, it is still difficult at this point to identify whether ferroelectricity, or the mobile-defect effect proposed here, can individually explain the observations made accurately. It is however expected that a ferroelectric rearrangement should remain even when the field is removed, and only be coerced to dissipate when going to the reverse bias, which is not fully consistent with the results achieved – it was observed that the effect dissipates upon reducing the applied bias, rather than fully reversing it. It could also be suggested that the energy necessary to re-disorder the cations is being supplied by the solar illumination or heating.

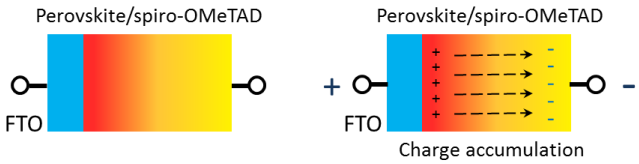


Figure 6.7: Schematic illustration of the proposed charging effect giving a beneficial temporary photovoltaic performance under forward bias.

6.3.4 Perovskite-only System

To further probe into the nature of the short-lived beneficial effect, planar and meso-superstructured devices which consisted only of the perovskite material, i.e., without Ti-CL or spiro-OMeTAD, were fabricated in this study. Despite the absence of an electron or hole transporting layer, these devices were still able to attain apparent fast scan PCEs of 3.2 % and 7.1 %, respectively (Figure 6.8 and Table 6.1). Interestingly, the forward SC-FB scans still give marginal PCE values (0.7% for the

planar heterojunction, and 2.6% for the mesoporous sample). Predictably, similar to the case of Ti-CL free samples with HTM, these devices cannot be properly stabilised when held at their maximum power point voltage, mostly because the absence of a field causes recombination at the non-selective contacts which is crippling to overall device performance. This also displays that potential photo/electro activated charges which give rise to the hysteresis can be regenerated. Moreover, upon stabilising the cells for some time, re-performing a fast current-voltage scan led to almost identical J-V curves and PCEs in comparison to previous results. This again suggests that the photo/electric activation of charges may be responsible for a rather deceptive photovoltaic performance when the perovskite is brought into direct contact with metallic electrodes. Even hysteretic curves may not truly reflect the real working conditions of the devices. On this note, PCEs obtained from fast J-V scans should be treated with caution while steady-state holding voltage scans should be employed as an effective additional tool for interpreting genuine device performance.

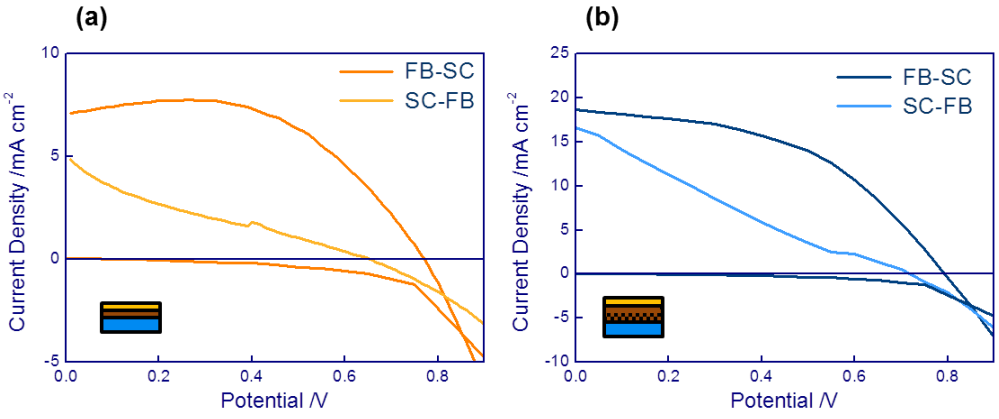


Figure 6.8: J-V curves of perovskite solar cells without Ti-CL and without spiro-OMeTAD layers. (a) Planar heterojunction device and (b) mesoporous structured device. Note the scales of the plots are different.

6.3.5 Hysteresis Loop from FTPS Measurement

To further investigate transient photovoltaic behaviour, a Fourier Transform Photocurrent Spectroscopy (FTPS) was used to evaluate the charge extraction at short-circuit under forward and reverse bias for both standard meso-superstructured, and Ti-CL free meso-superstructured devices (with spiro-OMeTAD). FTPS would be a powerful appliance to evaluate the variance in device operation brought about by defects, since the integrated IPCE can be obtained on a rather short timescale (~0.1s) allowing for the preservation of intermediate charged states during measurements and preventing the effects of defect relaxation on the results obtained.[38,39] By applying a voltage to polarise the devices for a specific duration of time, a corresponding IPCE spectrum was obtained by taking measurements immediately after the devices were short-circuited. Upon recording all IPCE spectra for the different applied bias, the mathematical integration of the IPCE spectra were plotted as a function of the applied bias. The experimental setup and design have been described in detail in section 6.2.5. In an ideal situation, the integrated IPCE would remain unaffected regardless of various biasing conditions such as sweep direction and biasing time, if pre-biasing does not essentially alter the device performance.

Furthermore, in an ideal situation for solar PV devices, an immediate rise to the steady maximum value which is good diode-like behaviour is expected once a forward bias is applied. As shown in Figure 6.9a during the forward scan, the integrated IPCE values of the standard meso-superstructured device with a Ti-CL rise to the steady maximum value approximately at 0.6V applied forward bias, while the absence of a Ti-CL causes a much slower rise eventually reaching the maximum at over 1.5V of bias as depicted in Figure 6.9b. Additionally, the integrated IPCEs obtained from the reverse bias sweep of the standard MSSCs with Ti-CL are very

close to those of the previous forward scan. This contrasts with the plots of the Ti-CL-free MSSCs, where there is a significant gap between the results obtained from the forward and reverse scans. Figure 6.9b also shows that the initial integrated IPCE values of the Ti-CL-free MSSCs is almost one tenth of the maximum value, which corresponds with the differences between the J_{sc} values obtained from fast J-V scans, and those obtained during maximum power stabilisation. This phenomenon suggests that biasing significantly alters the operation mechanism of the cells in the absence of Ti-CLs which could be related to their high dielectric constant. Moreover, in the Ti-CL-free system, a considerable hysteresis loop is derived from the backward scan, and is in line with the possible movement of charged defects, and also consistent with the hysteresis observed in the J-V curve in Figure 6.2, where the Ti-CL-free MSSC suffered a more pronounced hysteresis than the MSSC with a Ti-CL.

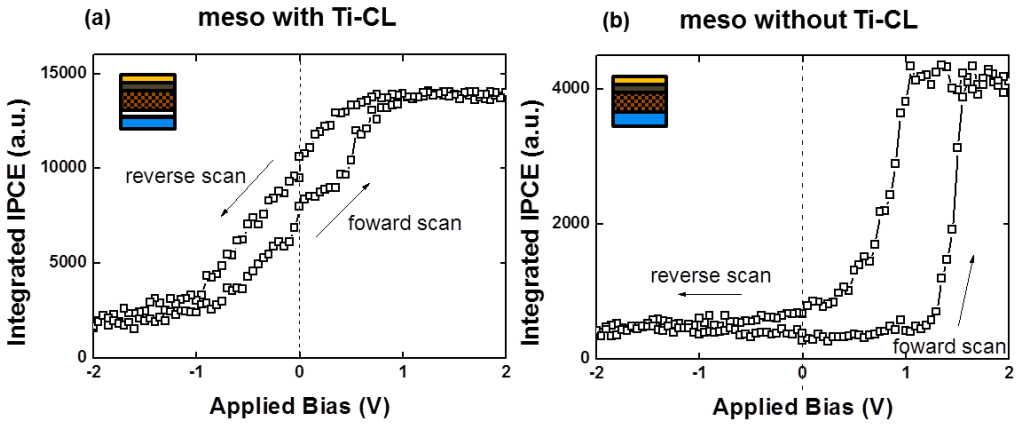


Figure 6.9: IPCE loops based on FTPS measurement

The intrinsic defects and their relation to the built-in field in perovskite films merit further scrutiny. This work highlights the impact of this temporary built-in field, as the potential permanent establishment of this field could prove highly profitable for the fabrication of extremely efficient photovoltaic devices with optimum stabilised power conversion efficiencies. A possible route to achieving this, for instance, is by

doping the perovskite to form a *p*-*n* or *p*-*i*-*n* junction. This is still a major challenge for conventionally employed solution-processing routes and as such, is yet to be implemented. In light of this, further studies will focus on achieving reliable doping profiles in order to realise this concept.

6.4 Summary

In the present work, the hysteretic phenomenon that exists in perovskite solar cells fabricated with different configurations has been observed. Although the planar heterojunction and meso-superstructured perovskite devices completely free of the titania hole-blocking compact layer obtained apparent PCEs of 11% and 13.2% respectively, applying a steady voltage at maximum power to these devices led to the generation of much lower PCEs than that from the fast current-voltage scans. This suggests a short-lived effect existing in the perovskite-based devices, caused by a built-in-field. A mechanism involving the activation and migration of mobile intrinsic charged defects has been proposed as the potential origin of the temporarily observed photovoltaic and hysteretic behaviour. Thus, it is clearly advantageous to employ an *n*-type charge selective contact layer in order to realise hole-blockage and stabilise power output. Controlled doping of the perovskite to create a beneficially permanent built-in-field may result in improved stabilised PCEs and it greatly promises to enhance the performance of perovskite solar cells, if achieved. Although this is still unfeasible for solution-processing methods, vapour deposition techniques have successfully demonstrated controlled levels of doping.[40,41] Incorporating vapour deposition techniques with the objective of realising controlled doping is most likely the next possible path towards high-efficiency perovskite devices.

References

1. Lee, M. M., Teuscher, J., Miyasaka, T., Murakami, T. N. & Snaith, H. J. Efficient Hybrid Solar Cells Based on Meso-Superstructured Organometal Halide Perovskites. *Science* **338,** 643–647 (2012).

2. Kim, H.-S. *et al.* Lead iodide perovskite sensitized all-solid-state submicron thin film mesoscopic solar cell with efficiency exceeding 9%. *Sci. Rep.* **2,** 591 (2012).

3. Burschka, J. *et al.* Sequential deposition as a route to high-performance perovskite-sensitized solar cells. *Nature* **499,** 316–9 (2013).

4. Zhou, H. *et al.* Interface engineering of highly efficient perovskite solar cells. *Science.* **345,** 542–546 (2014).

5. Jeon, N. J. *et al.* Solvent engineering for high-performance inorganic-organic hybrid perovskite solar cells. *Nat. Mater.* **13,** 897–903 (2014).

6. Snaith, H. J. *et al.* Anomalous Hysteresis in Perovskite Solar Cells. *J. Phys. Chem. Lett.* **5,** 1511–1515 (2014).

7. Sanchez, R. S. *et al.* Slow Dynamic Processes in Lead Halide Perovskite Solar Cells. Characteristic Times and Hysteresis. *J. Phys. Chem. Lett.* **5,** 2357–2363 (2014).

8. Unger, E. L. *et al.* Hysteresis and transient behavior in current-voltage measurements of hybrid-perovskite absorber solar cells. *Energy Environ. Sci.* (2014). doi:10.1039/C4EE02465F

9. Ball, J. M., Lee, M. M., Hey, A. & Snaith, H. J. Low-temperature processed meso-superstructured to thin-film perovskite solar cells. *Energy Environ. Sci.* **6,** 1739–1743 (2013).

10. Wojciechowski, K., Saliba, M., Leijtens, T., Abate, A. & Snaith, H. J. Sub-150 °C processed meso-superstructured perovskite solar cells with enhanced efficiency. *Energy Environ. Sci.* **7,** 1142 (2014).

11. Wang, J. T.-W. *et al.* Low-temperature processed electron collection layers of graphene/TiO_2 nanocomposites in thin film perovskite solar cells. *Nano Lett.* **14,** 724–30 (2014).

12. Liu, D. & Kelly, T. L. Perovskite solar cells with a planar heterojunction structure prepared using room-temperature solution processing techniques. *Nat. Photonics* **8,** 133–138 (2013).

13. Dualeh, A. *et al.* Impedance spectroscopic analysis of lead iodide perovskite-sensitized solid-state solar cells. *ACS Nano* **8,** 362–73 (2014).

14. Albin, D. S. & del Cueto, J. A. Correlations of capacitance-voltage hysteresis with thin-film CdTe Solar cell performance during accelerated lifetime testing. in *2010 IEEE Int. Reliab. Phys. Symp.* 318–322 (IEEE, 2010). doi:10.1109/IRPS.2010.5488811

15. Monokroussos, C. *et al.* The Effects of Solar Cell Capacitance on Calibration Accuracy When using a Flash Simulator. in *2006 IEEE 4th World Conf. Photovolt. Energy Conf.* **2,** 2231–2234 (IEEE, 2006).

16. Heiser, T. & Weber, E. Transient ion-drift-induced capacitance signals in semiconductors. *Phys. Rev. B* **58,** 3893–3903 (1998).

17. Frost, J. M. *et al.* Atomistic origins of high-performance in hybrid halide perovskite solar cells. *Nano Lett.* **14,** 2584–90 (2014).

18. Brivio, F., Walker, A. B. & Walsh, A. Structural and electronic properties of hybrid perovskites for high-efficiency thin-film photovoltaics from first-principles. *APL Mater.* **1,** 042111 (2013).

19. Stoumpos, C. C., Malliakas, C. D. & Kanatzidis, M. G. Semiconducting tin and lead iodide perovskites with organic cations: phase transitions, high mobilities, and near-infrared photoluminescent properties. *Inorg. Chem.* **52,** 9019–38 (2013).

20. Lyubomirsky, I., Rabinal, M. K. & Cahen, D. Room-temperature detection of mobile impurities in compound semiconductors by transient ion drift. *J. Appl. Phys.* **81,** 6684 (1997).

21. MIZUSAKI, J., ARAI, K. & FUEKI, K. Ionic conduction of the perovskite-type halides. *Solid State Ionics* **11,** 203–211 (1983).

22. Eperon, G. E., Burlakov, V. M., Docampo, P., Goriely, A. & Snaith, H. J. Morphological Control for high performance, Solution-processed Planar Heterojunction Perovskite Solar Cells. *Adv. Funct. Mater.* **24,** 151–157 (2014).

23. Saliba, M. *et al.* Influence of Thermal Processing Protocol upon the Crystallization and Photovoltaic Performance of Organic–Inorganic Lead Trihalide Perovskites. *J. Phys. Chem. C* **118,** 17171-17177 (2014).

24. You, J. *et al.* Low-temperature solution-processed perovskite solar cells with high efficiency and flexibility. *ACS Nano* **8,** 1674–80 (2014).

25. Leijtens, T. *et al.* Electronic properties of meso-superstructured and planar organometal halide perovskite films: charge trapping, photodoping, and carrier mobility. *ACS Nano* **8,** 7147–55 (2014).

26. Chen, Q. *et al.* Controllable Self-Induced Passivation of Hybrid Lead Iodide Perovskites toward High Performance Solar Cells. *Nano Lett.* **14,** 4158–63 (2014).

27. Barnea-Nehoshtan, L., Kirmayer, S., Edri, E., Hodes, G. & Cahen, D. Surface Photovoltage Spectroscopy Study of Organo-Lead Perovskite Solar Cells. *J. Phys. Chem. Lett.* **5,** 2408–2413 (2014).

28. Chen, Q. *et al.* Planar heterojunction perovskite solar cells via vapor-assisted solution process. *J. Am. Chem. Soc.* **136,** 622–5 (2014).

29. Peng, B. *et al.* Systematic investigation of the role of compact TiO_2 layer in solid state dye-sensitized TiO_2 solar cells. *Coord. Chem. Rev.* **248,** 1479–1489 (2004).

30. Burke, A. *et al.* The function of a TiO_2 compact layer in dye-sensitized solar cells incorporating "planar" organic dyes. *Nano Lett.* **8,** 977–81 (2008).

31. AZO Materials. Titanium Dioxide - Titania (TiO_2). (2014). at <http://www.azom.com/article.aspx?ArticleID=1179>

32. *Handbook of Low and High Dielectric Constant Materials and Their Applications (Two-Volume Set).* 1108 (Academic Press, 1999).

33. Kim, J., Lee, S.-H., Lee, J. H. & Hong, K.-H. The Role of Intrinsic Defects in Methylammonium Lead Iodide Perovskite. *J. Phys. Chem. Lett.* **5,** 1312–1317 (2014).

34. Yin, W.-J., Shi, T. & Yan, Y. Unusual defect physics in $CH_3NH_3PbI_3$ perovskite solar cell absorber. *Appl. Phys. Lett.* **104,** 063903 (2014).

35. Juarez-Perez, E. J. *et al.* Photoinduced Giant Dielectric Constant in Lead Halide Perovskite Solar Cells. *J. Phys. Chem. Lett.* **5,** 2390–2394 (2014).

36. Study of light-induced structural changes associated with Staebler-Wronski Photo-degradation in micro-crystalline silicon thin films. *Phys. Semicond. Devices* 379–382 (2014). doi:10.1007/978-3-319-03002-9

37. Yang, L. *et al.* Initial light soaking treatment enables hole transport material to outperform spiro-OMeTAD in solid-state dye-sensitized solar cells. *J. Am. Chem. Soc.* **135,** 7378–85 (2013).

38. Vanecek, M. & Poruba, A. Fourier-transform photocurrent spectroscopy of microcrystalline silicon for solar cells. *Appl. Phys. Lett.* **80,** 719 (2002).

39. Goris, L. *et al.* Observation of the subgap optical absorption in polymer-fullerene blend solar cells. *Appl. Phys. Lett.* **88,** 052113 (2006).

40. Yang, F., Shtein, M. & Forrest, S. R. Morphology control and material mixing by high-temperature organic vapor-phase deposition and its application to thin-film solar cells. *J. Appl. Phys.* **98,** 014906 (2005).

41. Shah, A., Torres, P., Tscharner, R., Wyrsch, N. & Keppner, H. Photovoltaic Technology: The Case for Thin-Film Solar Cells. *Science.* **285,** 692–698 (1999).

Chapter 7

Ongoing Work: Room-Temperature Fabrication of Tandem Perovskite Solar Cells

Content and Summary

Previous chapters have shown that single junction thin-film perovskite devices generated the optimum PCE values exceeding 15%. However, the efficiency of PV cells within this category is theoretically limited since only photons with energy values higher than the bandgap energy of the semiconducting material can be absorbed to generate charges. This chapter therefore introduces an ongoing project aimed at constructing an all-perovskite tandem device by joining two sub-cells. The individual perovskite films employed in both sub-cells possessed different optical properties thereby satisfying the prerequisites that define a tandem solar cell. Both sub-cells were fabricated via room-temperature processing techniques.

Although the idea seems straightforward, further optimisation of the performance of each individual sub-cell is required to achieve an optimally functioning tandem device. The work is currently in progress, nonetheless, the challenges encountered thus far in the process of building an all-perovskite tandem photovoltaic device are discussed in this chapter.

7.1 Introduction

Research on hybrid organic-inorganic perovskite solar cells has attracted significant attention due to the capability of these cells to exhibit unique intrinsic properties which can be capitalised on for photovoltaic applications, such as possessing appropriate band gap alignments, extended hole-electron diffusion lengths, and long carrier lifetimes. The previous chapters have shown that hybrid organic-inorganic halide perovskite films can dually function as light absorbers, as well as electron/hole conductors. This semiconducting nature renders the thin-film configuration of perovskite based devices possible. As presented in Chapter 4 and Chapter 5, the PCE of the single-junction planar heterojunction perovskite device fabricated by vapour deposition reached 15%.

Additionally, as mentioned in Chapter 6, the syntheses of most conventional electron-transport layers (i.e., *n*-type compact TiO_2) require a high-temperature sintering process (~500 ^{o}C). This limits the development of multi-junction devices, and serves as a bottleneck for industrial scale production. In order to address this challenge, room-temperature processing techniques involving "regular" and "inverted" configurations have been investigated.[1,2,3,4,5,6,7,8] "Regular" and "inverted" denotations are related to the polarity of the cell, which is determined by the relative positioning of the hole transporting material with respect to the electron transporting material. In the present work, "regular" configuration of a device refers to an assembly comprising of the light absorber, deposited over *n*-type compact layer-covered FTO substrates, followed by an organic hole-transporter layer deposited over the resulting structure. In this configuration, holes are collected through the metal cathode while electrons pass through the FTO anode. All devices discussed in the previous chapters were based on

this “regular” configuration. The “regular” configuration usually utilises a TiO_2 compact layer synthesised via different routes,[6,7] or an alternative metal oxide compact layer such as ZnO,[4,8,9] for the fabrication of solar PV devices under room-temperature conditions. On the contrary, the “inverted” architecture presents a scenario where electrons are collected at the metal electrodes, whereas holes are collected from the FTO coated substrates. The inverted structure which is comprised of organic charge collection layers also enables the fabrication of solar cells at room temperature[1,2,10] while demonstrating a PCE of up to 14%, as recently reported.[1] In addition to reasonable feasibility of production at room-temperature, negligible hysteresis has also been observed in devices based on the inverted strcuture.[1,2]

One of the significant advantages of room-temperature processed perovskite cells is that they permit the stacking of additional cells, hence, allowing for the easy attaining of multi-layer thin film architectures. The integration of more than one sub-cell within a single PV device leads to a “tandem” cell. Each sub cell produces an electric current in response to a different range of wavelength of light, facilitating the absorbance of a broader range of light spectra – therefore, improving the ability of the cell to efficiently convert sunlight to electrical energy. The fundamental limits associated with the performance of tandem devices have been studied extensively by De Vos.[11] De Vos’s report shows that the theoretical maximum power conversion efficiency values were boosted from 33.7% for a single-junction cell, to 42% and 49%, for optimal bandgap tandem device consisting of two and three sub-cells respectively.[11]

Vapour deposition is a straightforward route to constructing multi-junction architectures, and has been well developed for inorganic multi-junction devices.[14,15,16] An inorganic tandem cell based on InGaP/GaAs/InGaAs heterostructure achieved a

high PCE record of 37.9% under AM1.5G illumination.[12] However, the high capital cost associated with its fabrication limits its commercialisation. In recent years, the organic photovoltaic (OPV) industry has also utilised vapour deposition techniques for the deposition of small molecules in building tandem devices, that have effectively competed with solution processed OPV devices.[17,18] A polymer tandem cell with two sub-cells has recently been shown to achieve a PCE of 10% .[13]

This chapter therefore presents an ongoing study involving the exploration of room-temperature processing techniques for the fabrication of planar heterojunction perovskite solar cells, while fully addressing the prerequisites of an all-perovskite tandem device - consisting of two single-junction sub-cells. The perovskite film for the bottom sub-cell was fabricated by solution processing, while the perovskite film for the top cell was produced by dual-source vapour deposition. Combining a vapour-deposited cell and a solution-processed cell within a single tandem device circumvents the problems that result from the dissolution of the bottom cell, which tends to occur in cases where both cells have been fabricated from the same solvent. In order to enable stacking, the two sub-cells were fabricated at room-temperature based on the inverted configuration. The resulting architecture basically consisted of a perovskite film sandwiched between the charge collection layers (i.e., PEDOT:PSS as the hole transporting layer, and PCBM as the electron collection layer).

7.2 Methods

7.2.1 Synthesis of the Perovskite Precursors for Bottom Sub-Cell

The procedure for synthesising single halide perovskite precursors (i.e., $CH_3NH_3PbI_3$ and $CH_3NH_3PbBr_3$) has already been described in section 3.1. The desired bandgaps for the $CH_3NH_3PbI_{3-x}Br_x$ perovskite films used for the bottom sub-cell were

engineered by varying the stoichiometry of the pre-prepared $CH_3NH_3PbI_3$ and $CH_3NH_3PbBr_3$ solutions.

7.2.2 Fabrication of Perovskite Films for Top Sub-Cell

The mixed-halide perovskite ($CH_3NH_3PbI_{3-x}Cl_x$) film for the top sub-cell was deposited by dual-source vapour deposition employing the same protocols as described in section 4.2.2 in Chapter 4.

7.2.3 Fabrication of Inverted Single-Junction Device

The procedures for fabricating inverted planar heterojunction perovskite devices through solution processing have been presented elsewhere.[10] The clean etched FTO substrates were coated with a thin film of PEDOT:PSS by spin-coating (conditions: speed 2,000 r.p.m, ramp 2,000 r.p.m.s^{-1}, duration 60 s) a 25:75 vol% solution of PEDOT:PSS (Clevios):isopropanol (>99.9%, Fisher Chemicals). The solution was sonicated in an ultrasonic bath for 15 min and filtered with a 2.7 μm glass fibre filter before use. Subsequent to the spin-coating process, the substrates were annealed at 150 °C for 20 min. After cooling down, the perovskite films were deposited by either solution processing (see 7.2.1) or dual-source vapour deposition method (see 7.2.2), for the bottom and top cells respectively. The solution-processed perovskite film for the bottom cell was annealed at 120^{o}C for 10 min, while the vapour-deposited mixed-halide perovskite film for the top cell was annealed at 100^{o}C for 45 min. The electron selective contact was deposited by spin coating (speed 1,000 r.p.m, ramp 1,000 r.p.m.s^{-1}, duration 45 s) a 10 mg/mL solution of PCBM in chlorobenzene (Anhydrous, Sigma-Aldrich). The TiO_x precursor solution[20] for the compact layer was then spin coated (speed 3,000 r.p.m, ramp 3,000 r.p.m.s^{-1}, duration 45 s), followed by

annealing at 130 °C for 10 min. Finally, devices were completed under high vacuum conditions by evaporating Al contact electrodes on them.

7.2.4 Fabrication of Tandem Device

The fabrication of the perovskite tandem device began with the deposition of the bottom cell, following the single-junction procedure described in section 7.2.3, exclusive of the evaporation of Al electrodes. A PEDOT:PSS layer was spin-coated on top of the already synthesised bottom cell before transferring the sample into an evaporation system. The perovskite film for the top cell was deposited by DSVD method, followed by an annealing process at 100^{o}C for 45 min. Using the same procedures outlined for the single-junction devices in section 7.2.3, successive coatings of PCBM and TiO_x were applied onto the annealed films to provide an electron selective contact. The devices were completed with Al electrodes.

7.3 Results and Discussion

The structure of an inverted single-junction perovskite device is illustrated in Figure 7.1 below. The PEDOT:PSS layer deposited on the fluorine-doped tin oxide (FTO)-coated glass, functions as the hole transporting layer, while the PCBM and TiO_x layers were deposited on top of the perovskite film to act as the electron acceptor. Aluminium was then evaporated as a metal electrode to complete the device.

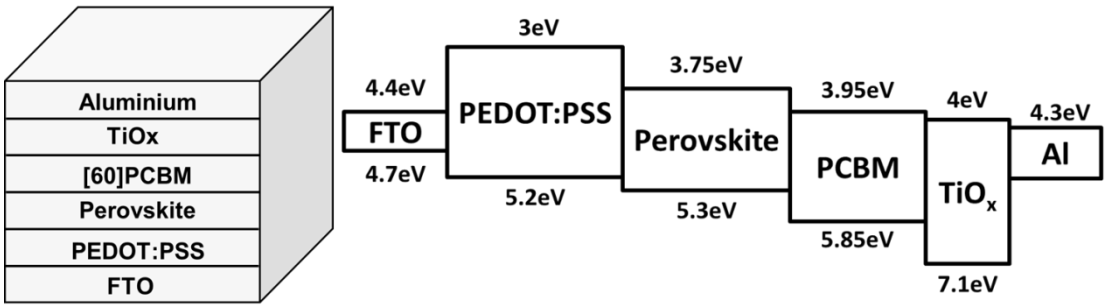


Figure 7.1: Illustration of a single-junction perovskite device based on inverted configuration (FTO/PEDOT:PSS/$CH_3NH_3PbX_3$/PCBM/TiO_x/Al). (a) Device configuration and **(b)** charge transport of thin film perovskite device based on inverted structure.

In a tandem device, light with shorter wavelengths are preferentially absorbed before those with longer wavelengths.[19] In other words, the solution-processed sub-cell at bottom is expected to possess a relatively larger band gap, while the vapour-deposited top cell requires a relatively narrower band gap to ultimately cover a larger solar spectrum. As was previously mentioned, the theoretical optimal bandgaps required for sub-cells to achieve maximum conversion efficiencies have been calculated by De Vos.[11] In the case of the vapour-deposited $CH_3NH_3PbI_{3-x}Cl_x$ perovskite film (as optimised in Chapter 4) with an approximate bandgap of 1.6eV, maximum efficiency can be achieved by integrating a wider bandgap (≈ 2eV) semiconductor, to the bottom of the device.[11] Figure 7.2 illustrates the structure of the all-perovskite tandem device created by incorporating two 'inverted' sub-cells.

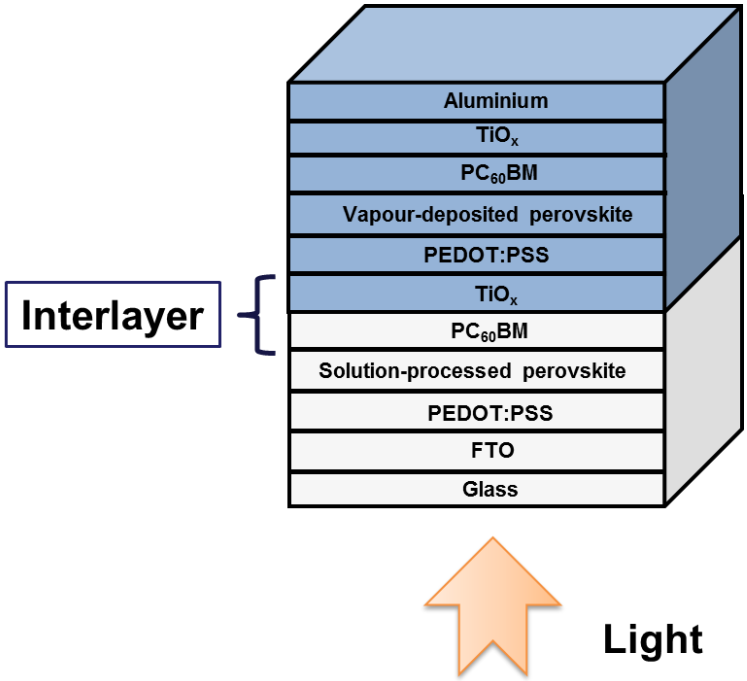


Figure 7.2: Illustration of the structure of a tandem cell formed by incorporating two inverted cells. Solution-processed perovskite film at bottom has a relatively wider bandgap, while the vapour-deposited perovskite film on top has a narrower bandgap.

7.3.1 Fabrication of Bottom Cells through Solution Processing

To obtain a solution-processed perovskite material with a bandgap of 2eV, the bandgap tuning of $CH_3NH_3PbX_3$ (CH_3NH_3=MA, i.e., $MAPbX_3$) was achieved via the substitution of Br^- ions with I^- ions to form a $CH_3NH_3PbI_{3-x}Br_x$ structure. The bandgap energies of $CH_3NH_3PbI_3$ (i.e., $MAPbI_3$) and $CH_3NH_3PbBr_3$ (i.e., $MAPbBr_3$), have been reported as 1.5eV and 2.3eV, respectively.[21,22] A common approach taken with regards to the bandgap engineering of perovskite devices, is preparing a stoichiometric mixture of the two pre-prepared trihalide perovskite solution precursors, $MAPbI_3$ and $MAPbBr_3$.[23]

$MAPbI_3$ has a tetragonal crystal phase of the *I4/mcm* space group, while $MAPbBr_3$ crystallises in the cubic $Pm\bar{3}m$ space group at room temperature.[24] The structural differences between the two perovskites probably stem from the differences in the ionic radius of I^- and Br^- ions with 6-fold coordination where $MAPbI_3$ and $MAPbBr_3$

exhibit lengths of 2.2 Å and 1.96 Å respectively. As was mentioned in Chapter 2, in ABX_3 perovskite structures, smaller X ion radius is relatively beneficial for the formation and stability of an overall cubic structure.[25] The X-ray diffraction spectra in Figure 7.3a falls within the 2θ range of 5^o~65^o. This confirms that $MAPbI_3$ and $MAPbBr_3$ have identical tetragonal and cubic peaks at room-temperature respectively, in agreement with previous reports.[21,22,26] Therefore, increasing the concentration of Br^- ions to substitute for I^- ions causes the crystal structure to transit from a tetragonal phase to cubic one. Noh *et al* have demonstrated that the tetragonal phase of $MAPbI_{3-x}Br_x$ completely transforms into a cubic phase at $MAPbI_{2.4}Br_{0.6}$ (i.e., $MAPbI_3$:$MAPbBr_3$=0.8:0.2).[27] As depicted by Figure 7.3b, within the range of 14^o~15^o of the XRD spectra, the peaks shift towards higher 2θ values suggesting a decrease in lattice spacing induced by the replacement of larger I^- ions with smaller Br^- ions in the crystal lattice.

To verify that variations in the optical properties of the doped perovskite films comply with varying dopant concentrations, the UV−Vis absorbance spectra of the $MAPbI_{3-x}Br_x$ based perovskites under different doping concentrations were obtained as shown in Figure 7.3c. The plots in this figure show that the onset absorption band of $MAPbI_{3-x}Br_x$ can be tuned from a wavelength of 765 nm (i.e., 1.63eV) to 545 nm (i.e., 2.27eV); this practically results in a change in film colouration (ie. from dark brown to brown-red to light yellow). A blue shift of the absorption band edge in the UV-vis spectra confirms successful doping, indicating that heavier Br^- doping leads to a wider bandgap. A molar composition ratio of 0.4:0.6 (i.e., $MAPbI_{1.2}Br_{1.8}$) for $CH_3NH_3PbI_3$ relative to $CH_3NH_3PbBr_3$, features an onset wavelength of approximately 620 nm (i.e.,~ 2eV).

Furthermore, to investigate the variation of the charge lifetimes with the insertion of Br^- ions, the time-resolved photoluminescence curves of perovskites at different Br^- ion doping levels were obtained as shown in Figure 7.3d. The figure indicates that the PL lifetime becomes longer, reaching the maximum at $MAPbI_{1.2}Br_{1.8}$ with an increase in Br ion concentration, further addition of Br ions leads to lifetime reduction. This outcome suggests that the mixed halide perovskite film ($MAPbI_{3-x}Br_x$ ($x \neq 0$ or 3)) has a longer lifetime than a single halide perovskite film (i.e., $MAPbBr_3$ and $MAPbI_3$). This is in line with reports from literature indicating that mixed halide perovskite ($CH_3NH_3PbI_{3-x}Cl_x$) films have relatively longer lifetimes than the corresponding triiodide perovskite($CH_3NH_3PbI_3$) films.[28]

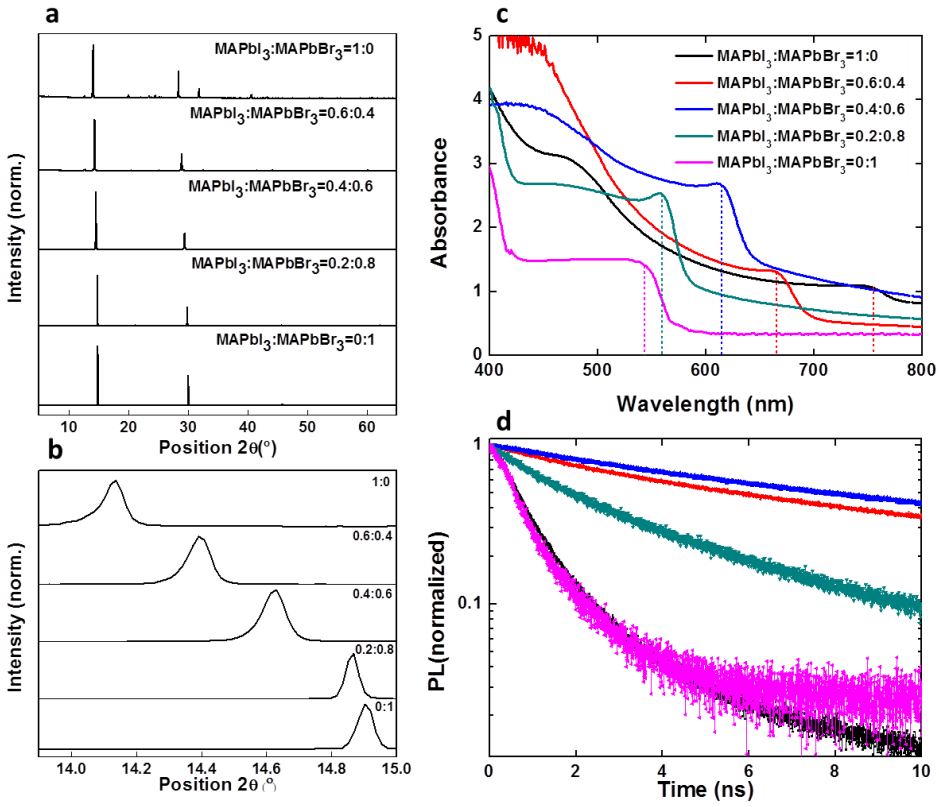


Figure 7.3: Crystallographic and optical properties of the perovskite films for the bottom sub-cell. X-ray diffraction (XRD) spectra at range of **(a)** 5^o~65^o and (**b**) 14^o~15^o respectively; **(c)**Ultraviolet–visible absorbance spectra **(d)** Time-resolved PL measurements taken at the peak emission wavelength; of the mixture precursors at molar compositions at 1:0, 0.6:0.4, 0.4:0.6, 0.2:0.8 and 0:1 of $MAPbI_3$:$MAPbBr_3$ respectively.

A PCE of 3.7% was attained by optimising device performance with $MAPbI_{1.2}Br_{1.8}$ (i.e., 2eV bandgap) perovskite films at room-temperature. This device featured a J_{sc} of 8.77 $mAcm^{-2}$, V_{oc} of 0.7 V and *FF* of 0.58 (Figure 7.4). In principle, the J-V characteristics should vary as a function of the Br ion doping levels. Adding Br ions to the system, led to the appearance of a blue shift at the absorption onset, due to a widening in the band gap which improves V_{oc} but reduces J_{sc}. However, previous literature in the field have claimed that device efficiency experiences an abrupt drop near the 2 eV bandgap and it is believed that the charge transport and recombination behaviour of $MAPbI_xBr_{3-x}$ acting as both light harvester and hole transporter greatly fluctuates within this range and additional factors possibly affect the device performance.[27] A greater understanding of the correlation between the photophysical properties and performance of the device is required to further optimise device efficiency within the proximity of the 2 eV bandgap range.

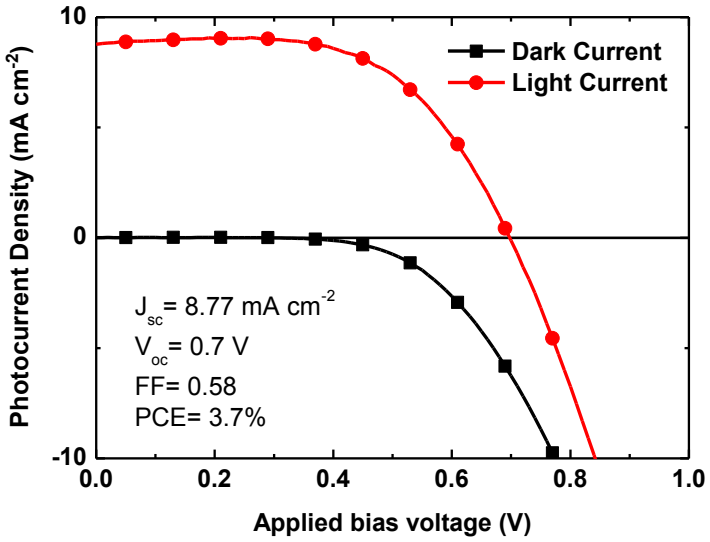


Figure 7.4: Photovoltaic performance of the inverted device with 2eV bandgap perovskite film

7.3.2 Fabrication of Top Cells through Vapour Deposition

The current density–voltage (J-V) curve obtained under the irradiance of an AM1.5 100 $mWcm^{-2}$ solar simulator for the best performing inverted planar heterojunction solar cell fabricated through vapour deposition is shown in Figure 7.5a. The device incorporated the dual-source vapour-deposited perovskite film (as optimised in Chapter 4) into the inverted configuration, as shown in Figure 7.1a. It exhibited a J_{sc} of 14.4 mA cm^{-2}, a *Voc* of 0.87 V, and an *FF* of 0.35, yielding a PCE of 4.4%. In comparison to the PCE of 15% achieved by the regular planar heterojunction vapour-deposited perovskite solar cell (FTO/TiO_2/Perovskite/Spiro) discussed extensively in Chapter 4 and Chapter 5, there is a substantial loss in PCE for the inverted device which is attributed to changes in all three device performance parameters i.e. J_{sc}, V_{oc} and *FF*. A probable key reason for this loss could be the non-continuous film formation of the PCBM observed on top of the perovskite film and it originates from its de-wetting - as shown in Figure 7.5b and Figure 7.5c. De-wetting of PCBM on the vapour deposited perovskites could be due to the nature of the ultrasmooth vapour-deposited perovskite films which unlike the conventionally solution-processed perovskite from a single precursor solution, has a rougher surface that inhibits PCBM coverage.[10] The non-uniform and clustered film morphology of PCBM adversely affects the subsequent deposition of the TiO_x layer on top of PCBM. Although tandem devices incorporating the 'inverted' configuration with the vapour-deposited perovskite films require further optimisation, the results obtained so far demonstrate the feasibility of a room-temperature method and highlight the potential of creating an all-perovskite tandem device.

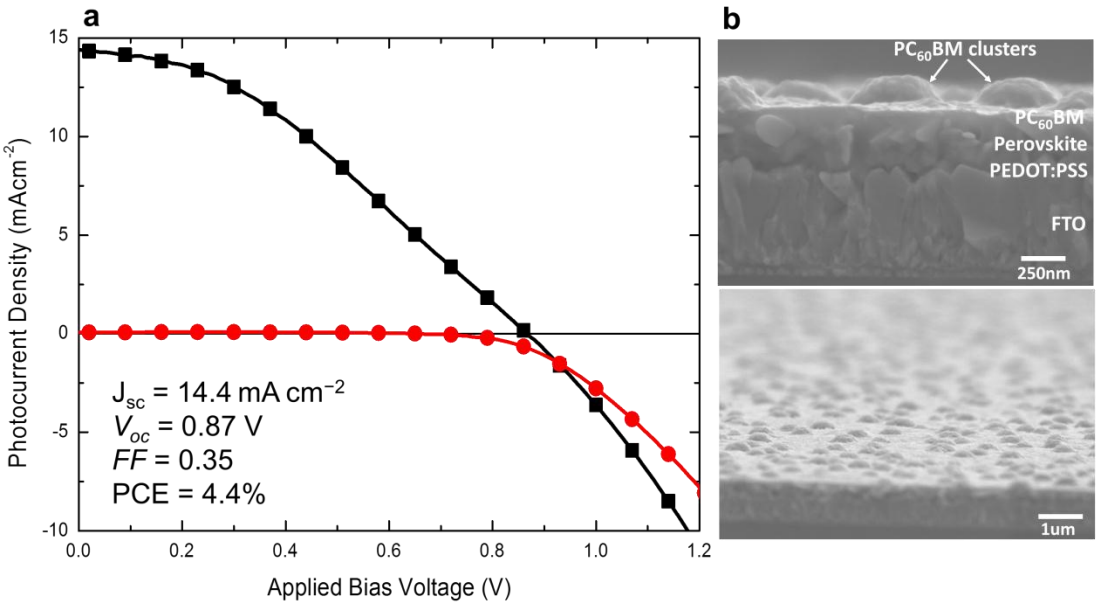


Figure 7.5: (a) Photovoltaic performance and (b) SEMs images of PCBM de-wetting issues of the vapour-deposited inverted device

7.3.3 Model of an All-Perovskite Tandem Device

By combining the solution-processed $MAPbI_{1.2}Br_{1.8}$ perovskite film with the vapour-deposited $MAPbI_{3-x}Cl_x$ perovskite cell, an all-perovskite tandem solar cell was premiered and its cross-sectional SEM image is shown in Figure 7.6. Although both inverted sub-cells stacked up uniformly without destroying each other, this tandem device was unable to generate any PCE. This device underperforms by our standard and optimisation on each individual sub-cell is necessary before the performance of the tandem device can be further tuned. This study is still in progress, and will potentially broaden the variety of possible device configurations that can be employed by perovskite-based solar PV cells.

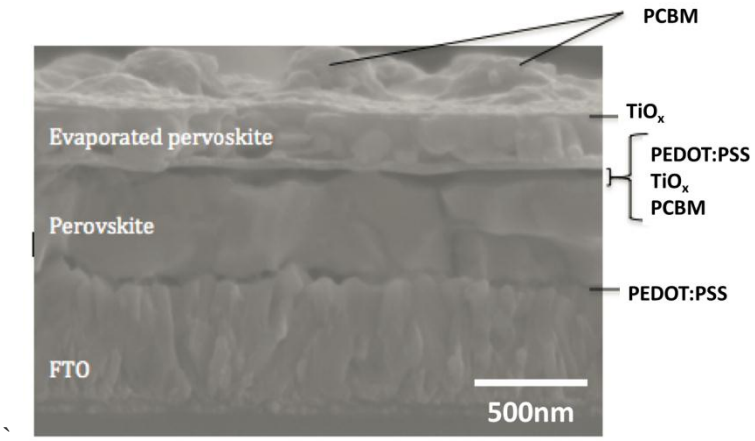


Figure 7.6: SEMs images of the tandem structure constructed with two inverted sub-cells

7.4 Summary

In the present work, the concept of an all-perovskite tandem device has been proposed. This perovskite tandem device was constructed by stacking two inverted sub-cells, comprising of perovskite films fabricated via both solution processing and vapour deposition respectively. Despite the obvious requirement for further optimisation of each individual sub-cell, the results obtained thus far greatly project the feasibility of fabricating an all-perovskite tandem photovoltaic device at room temperature. This work reveals broader prospects that can be applied towards perovskite solar cell technology. The versatility of the perovskite absorber possibly rivals that of c-Si which is the most established solar cell material currently in the PV industry.

Upon fully completing the optimisation of the two sub-cells, another challenge is the establishment of synergy between the two sub-cells within a tandem system. As a single current flows through the sub-cells in serial connection, current matching of the sub-cells leads to compromise the voltage in the tandem system.[11,13,29] A well-coordinated device construction process is required to determine the overall performance of the tandem device.

References

1. Seo, J. *et al.* Benefits of very thin PCBM and LiF layers for solution-processed p–i–n perovskite solar cells. *Energy Environ. Sci.* **7,** 2642 (2014).

2. Wang, Q. *et al.* Large fill-factor bilayer iodine perovskite solar cells fabricated by a low-temperature solution-process. *Energy Environ. Sci.* **7,** 2359 (2014).

3. Yella, A., Heiniger, L.-P., Gao, P., Nazeeruddin, M. K. & Grätzel, M. Perovskite solar cells with a planar heterojunction structure prepared using room-temperature solution processing techniques. *Nano Lett.* **14,** 2591–6 (2014).

4. Schumann, S. *et al.* Inverted organic photovoltaic devices with high efficiency and stability based on metal oxide charge extraction layers. *J. Mater. Chem.* **21,** 2381 (2011).

5. Jeon, N. J. *et al.* Solvent engineering for high-performance inorganic-organic hybrid perovskite solar cells. *Nat. Mater.* **13,** 897–903 (2014).

6. Wojciechowski, K., Saliba, M., Leijtens, T., Abate, A. & Snaith, H. J. Sub-150 °C processed meso-superstructured perovskite solar cells with enhanced efficiency. *Energy Environ. Sci.* **7,** 1142 (2014).

7. Wang, J. T.-W. *et al.* Low-temperature processed electron collection layers of graphene/TiO_2 nanocomposites in thin film perovskite solar cells. *Nano Lett.* **14,** 724–30 (2014).

8. Liu, D. & Kelly, T. L. Perovskite solar cells with a planar heterojunction structure prepared using room-temperature solution processing techniques. *Nat. Photonics* **8,** 133–138 (2013).

9. Dearden, C. A. *et al.* High voltage hybrid organic photovoltaics using a zinc oxide acceptor and a subphthalocyanine donor. *Phys. Chem. Chem. Phys.* **16,** 18926–32 (2014).

10. Docampo, P., Ball, J. M., Darwich, M., Eperon, G. E. & Snaith, H. J. Efficient organometal trihalide perovskite planar-heterojunction solar cells on flexible polymer substrates. *Nat. Commun.* **4,** 2761 (2013).

11. Vos, A. De. Detailed balance limit of the efficiency of tandem solar cells. *J. Phys. D. Appl. Phys.* **13,** 839–846 (1980).

12. Sugo, M., Takanashi, Y., Al-jassim, M. M. & Yamaguchi, M. Heteroepitaxial growth and characterization of InP on Si substrates. *J. Appl. Phys.* **68,** 540 (1990).

13. Dupuis, R. D. III-V semiconductor heterojunction devices grown by metalorganic chemical vapor deposition. *IEEE J. Sel. Top. Quantum Electron.* **6,** 1040–1050 (2000).

14. King, R. R. *et al.* 40% efficient metamorphic GaInP⁄GaInAs⁄Ge multijunction solar cells. *Appl. Phys. Lett.* **90,** 183516 (2007).

15. Green, M. A., Emery, K., Hishikawa, Y., Warta, W. & Dunlop, E. D. Solar cell efficiency tables (version 44). *Prog. Photovoltaics Res. Appl.* **22,** 701–710 (2014).

16. Riede, M. *et al.* Efficient Organic Tandem Solar Cells based on Small Molecules. *Adv. Funct. Mater.* **21,** 3019–3028 (2011).

17. New, E., Howells, T., Sullivan, P. & Jones, T. S. Small molecule tandem organic photovoltaic cells incorporating an α-NPD optical spacer layer. *Org. Electron.* **14,** 2353–2359 (2013).

18. You, J. *et al.* 10.2% power conversion efficiency polymer tandem solar cells consisting of two identical sub-cells. *Adv. Mater.* **25,** 3973–8 (2013).

19. Ball, J. M., Lee, M. M., Hey, A. & Snaith, H. J. Low-temperature processed meso-superstructured to thin-film perovskite solar cells. *Energy Environ. Sci.* **6,** 1739–1743 (2013).

20. Nelson, J. *The Physics of Solar cells*. (Imperial College Press, 2003).

21. Kim, H.-S. *et al.* Lead iodide perovskite sensitized all-solid-state submicron thin film mesoscopic solar cell with efficiency exceeding 9%. *Sci. Rep.* **2,** 591 (2012).

22. Kojima, A., Teshima, K., Shirai, Y. & Miyasaka, T. Organometal halide perovskites as visible-light sensitizers for photovoltaic cells. *J. Am. Chem. Soc.* **131,** 6050–6051 (2009).

23. Noh, J. H., Im, S. H., Heo, J. H., Mandal, T. N. & Seok, S. Il. Chemical management for colorful, efficient, and stable inorganic-organic hybrid nanostructured solar cells. *Nano Lett.* **13,** 1764–9 (2013).

24. Poglitsch, A. & Weber, D. Dynamic disorder in methylammoniumtrihalogenoplumbates (II) observed by millimeter-wave spectroscopy. *J. Chem. Phys.* **87,** 6373 (1987).

25. Cheng, Z. & Lin, J. Layered organic–inorganic hybrid perovskites: structure, optical properties, film preparation, patterning and templating engineering. *CrystEngComm* **12,** 2646 (2010).

26. Baikie, T. *et al.* Synthesis and crystal chemistry of the hybrid perovskite (CH_3NH_3)PbI_3 for solid-state sensitised solar cell applications. *J. Mater. Chem. A* **1,** 5628 (2013).

27. Noh, J. H., Im, S. H., Heo, J. H., Mandal, T. N. & Seok, S. Il. Chemical management for colorful, efficient, and stable inorganic-organic hybrid nanostructured solar cells. *Nano Lett.* **13,** 1764–9 (2013).

28. Stranks, S. D. *et al.* Electron-hole diffusion lengths exceeding 1 micrometer in an organometal trihalide perovskite absorber. *Science* **342,** 341–4 (2013).

29. Howells, T., New, E., Sullivan, P. & Jones, T. S. An External Quantum Efficiency Technique to Directly Observe Current Balancing in Tandem Organic Photovoltaics. *Adv. Energy Mater.* **1,** 1085–1088 (2011).

Chapter 8

Conclusions and Outlook

This chapter summarises the research findings and recommends areas for future research.

8.1 Research Overview

Hybrid organic-inorganic perovskite solar cells have gained a great deal of attention recently, owing to their relatively low cost and ease of processing. However, several challenges still restrict their applications in photovoltaic devices. Attaining enhanced power conversion efficiency values, while preserving the feasibility of large scale fabrication is crucial to realising high-volume commercial applications for perovskite-based photovoltaic devices. To accomplish this objective, this study focused intensively on the development of new industry-transferrable techniques, for the fabrication of highly efficient planar heterojunction organic-inorganic perovskite solar cells. As a result, vapour deposition techniques, which have been widely employed in the semiconductor industry for the fabrication of high quality thin films, were predominantly explored in this work. This research was conducted in three stages aimed at answering the questions outlined in Figure 8.1.

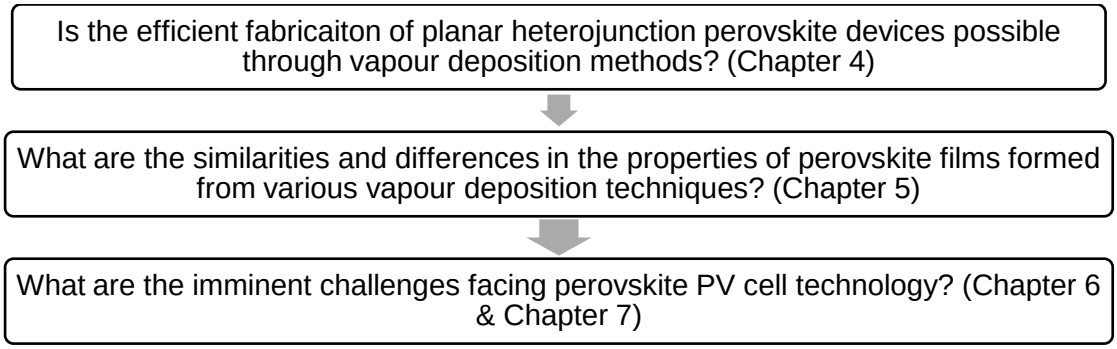


Figure 8.1: Summary of research steps

Upon establishing the relevant technical background knowledge and identifying the research gaps in Chapter 2, three major experiments were conducted in Chapter 4, Chapter 5, and Chapter 6. Furthermore, ongoing work related to the design of multi-junction solar perovskite devices was introduced in Chapter 7.

8.2 Work Done and Contribution

Chapter 4 demonstrated pioneering work on the employment of a dual-source vapour deposition (DSVD) technique for the fabrication of high-efficiency planar heterojunction perovskite solar cells, where hybrid organic-inorganic mixed-halide perovskite ($CH_3NH_3PbI_{3-x}Cl_x$) was utilised as the light absorber. These perovskite films were formed by thermally-evaporating the organic and inorganic precursors simultaneously in vacuum, thus, confirming that perovskite materials can be created entirely from solid-state materials under vacuum conditions. The outcomes from this section also highlighted that one of the primary advantages of vapour-deposited perovskite films over conventional spin-coated films is excellent film morphology (high uniformity and full coverage). Benefiting from the high-quality of the films, the resultant solar devices generated power conversion efficiencies that reached 15%, which was a record-breaking PCE for perovskite solar cells at the time the work was presented. The successful use of vapour deposition techniques to produce efficient thin

film perovskite solar cells is therefore expected to shorten the timeline leading to their large-scale manufacture.

To further expand the vapour deposition techniques and to gain an insight into the properties of the vapour-deposited perovskite films, Chapter 5 explored two-layer sequential vapour deposition (SVD) as an alternative vapour deposition method for the production of planar heterojunction perovskite ($CH_3NH_3PbI_3$) devices. The SVD technique was equally found to produce perovskite films exhibiting high uniformity and coverage. The effects of precursors' compositions and annealing conditions on the crystallographic and photo-physical properties of the films were also discussed. Findings here indicated that slightly imprecise reactions between the organic and inorganic precursors compromised purity and resulted in lower crystallinity within the films. An optimal annealing process assisted in the crystallisation of the perovskite films. Nonetheless, extended annealing induced thermal degradation of the perovskites, created amorphous parts and possibly resulted in mixed phases within the perovskite films. A parallel comparison between perovskite films obtained from both abovementioned vapour deposition techniques (i.e., SVD and DSVD) led to the identification of the merits and drawbacks associated with each technique, from various viewpoints such as crystal formation, carrier lifetime, film quality, and corresponding device performance. Integrating the optimised perovskite films derived from both (SVD and DSVD) fabrication techniques, yielded devices that achieved remarkable PCEs exceeding 15%. Moreover, from a manufacturing perspective, the SVD technique is less complicated, as it allows for the independent manipulation of the lead halide and methylammonium halide deposition parameters. The expansion of vapour deposition techniques in Chapter 5 brings perovskite solar cells a step further towards commercialisation.

Although the PCEs of perovskite-based devices were significantly improved, hysteresis, which is a common phenomenon in PV devices, was also observed in these perovskite solar cells. Chapter 6 systemically compared the hysteretic behaviour of the perovskite films in various configurations. An unusual behaviour was observed where the devices without compact layers delivered PCEs of over 11% in planar heterojunction, and over 13% in mesostructure, during fast J-V scans. Even more astonishing, was the fact that despite the absence of either an electron or hole transporting layer (i.e., without TiO_2 compact layer or spiro-OMeTAD), devices consisting solely of perovskite materials exhibited PCEs of 3.2 % and 7.1% in planar heterojunction and MSSCs respectively during fast J-V scans. Nevertheless, these devices experienced a dramatic reduction in PCE values when stabilised at their maximum power points. It is believed that a temporary built-in-field within the perovskite is responsible for the 'transient enhanced efficiencies' under the fast J-V scans and it is also related to the previously observed hysteresis. The polarisation of the perovskite diode under forward bias results in an effective *n*-type doping of the perovskite near the anode, and *p*-type doping near the cathode. This effect possibly provides the built-in potential promoting accumulation of positive and negative space charges near contacts which is crucial for charge extraction. The polarisation would then temporarily enable the operation of the perovskite solar cells, even without charge selective layers. This "contact doping" agrees with the migration and accumulation of ions within the perovskite film near the metallic contacts. Reducing the influence of the external field under working conditions can lead to the slow migration of these ions away from the junctions, and therefore, the weakening of the interface doping, adversely affecting the operation of the solar cells. Subsequent analyses revealed the enabling of a strong permanent built-in-field as a promising route to achieving

exceptionally efficient devices with corresponding well-stabilised power conversion efficiencies. This could be achieved for instance, by the controlled doping of the perovskite to form a *p-n* or *p-i-n* junction. Vapour deposition technique is a mature one that enables controlled doping,[1] while solution-based methods are still unable to successfully facilitate the precise control of doping levels. Employing vapour deposition techniques capable of realising controlled doping concentrations and introducing the permanent built-in-field, therefore, presents a potential path towards achieving high-efficiency perovskite devices.

Another important advantage of vapour deposition is its ability to produce multi-layer stacked thin films over extremely large areas. In comparison to other thin film fabrication avenues, vapour deposition is an established one that has been adopted in a wide range of manufacturing sectors including the glazing industry, the liquid-crystal display industry, and the thin-film solar energy industry. This is in a large part, due to the manufacturing of crystalline silicon HIT (heterojunction with thin intrinsic layer) solar cells[2] and thin-film solar cells[3]. Additionally, small molecular organic photovoltaics (OPV) produced via vapour deposition have been able to compete directly with solution processed OPV, despite involving much lower levels of research and development, because vapour deposition allows for the collection of charges at interfaces, as well as careful bandgap tuning, multi-junction architectures are more feasible with this technique.[4,5] Moreover, organic light emitting diodes[6,7] fabricated by the vapour deposition of extremely thin multilayer stacks have also proven to be commercially viable. Since perovskite solar cells have now achieved a performance level matching the efficiencies of c-Si and CIGS solar cells, a range of interesting possibilities present themselves. For instance, the current vapour deposited perovskite cells can be upgraded by employ them as “top cells” in “hybrid tandem junctions” for

either (crystalline silicon) c-Si, (copper indium gallium (di) selenide) CIGS or other emerging concepts.[8] The possibility of realising the concept of an "all-perovskite" multi-junction solar cell has been proposed in this study. Chapter 7 introduced the ongoing work aimed at building such an "all-perovskite" tandem device, comprising of the vapour-deposited perovskite as the "top cell", and the solution-processed perovskite as the "bottom cell". The individual sub-cells were functional. However, further optimisation is still required. The successful demonstration of the "all-perovskite" tandem device depicts the versatility of the perovskite absorber layer, indicating potential broader applications of the perovskite solar cell technology,

In conclusion, this study yielded results relevant to the future development of hybrid organic-inorganic perovskite solar cells. The effective exploration of vapour deposition techniques has diversified the fabrication process, and demonstrated the immense potential of the applied thin film configurations. This work has been fundamental to directing photovoltaics research towards thin film perovskite technology as well as to the applications of film morphology control regarding the enhancement of solar cell efficiency.[9,10,11,12,13,14] Organic-inorganic perovskite PV devices have been fully characterised here, revealing the need to improve stabilised maximum power conversion efficiency values. Further investigation is therefore recommended to overcome the prerequisites that are necessary for the mass commercialisation of perovskite-based solar cells.

References

1. Yang, F., Shtein, M. & Forrest, S. R. Morphology control and material mixing by high-temperature organic vapor-phase deposition and its application to thin-film solar cells. *J. Appl. Phys.* **98,** 014906 (2005).

2. Sakata, H. *et al.* 20.7% highest efficiency large area (100.5cm^2) HIT cell. in *Photovolt. Spec. Conf. 2000. Conf. Rec. Twenty-Eighth IEEE* 7–12 (2000). doi:10.1109/PVSC.2000.915742

3. Chopra, K. L., Paulson, P. D. & Dutta, V. Thin-film solar cells: an overview. *Prog. Photovoltaics Res. Appl.* **12,** 69–92 (2004).

4. New, E., Howells, T., Sullivan, P. & Jones, T. S. Small molecule tandem organic photovoltaic cells incorporating an α-NPD optical spacer layer. *Org. Electron.* **14,** 2353–2359 (2013).

5. Riede, M. *et al.* Efficient Organic Tandem Solar Cells based on Small Molecules. *Adv. Funct. Mater.* **21,** 3019–3028 (2011).

6. Reineke, S. *et al.* White organic light-emitting diodes with fluorescent tube efficiency. *Nature* **459,** 234–238 (2009).

7. You, H., Dai, Y., Zhang, Z. & Ma, D. Improved performances of organic light-emitting diodes with metal oxide as anode buffer. *J. Appl. Phys.* **101,** 026105 (2007).

8. Beiley, Z. M. & McGehee, M. D. Modeling low cost hybrid tandem photovoltaics with the potential for efficiencies exceeding 20%. *Energy Environ. Sci.* **5,** 9173 (2012).

9. Burschka, J. *et al.* Sequential deposition as a route to high-performance perovskite-sensitized solar cells. *Nature* **499,** 316–9 (2013).

10. Chen, Q. *et al.* Planar heterojunction perovskite solar cells via vapor-assisted solution process. *J. Am. Chem. Soc.* **136,** 622–5 (2014).

11. Im, J.-H., Kim, H.-S. & Park, N.-G. Morphology-photovoltaic property correlation in perovskite solar cells: One-step versus two-step deposition of $CH_3NH_3PbI_3$. *APL Mater.* **2,** 081510 (2014).

12. Zhou, H. *et al.* Interface engineering of highly efficient perovskite solar cells. *Science.* **345,** 542–546 (2014).

13. Hu, H. *et al.* Vapour-based processing of hole-conductor-free $CH_3NH_3PbI_3$ perovskite/C60 fullerene planar solar cells. *RSC Adv.* **4,** 28964 (2014).

14. Jeon, N. J. *et al.* Solvent engineering for high-performance inorganic-organic hybrid perovskite solar cells. *Nat. Mater.* **13,** 897–903 (2014).